The Dissertation Committee for Logan Edward Hillberry
certifies that this is the approved version of the following dissertation:

Optically trapped microspheres as sensors of mass and sound: Brownian motion as both signal and noise

Committee:

Mark G. Raizen, Supervisor

José R. Alvarado

Philip J. Morrison

Yuebing B. Zheng

Optically trapped microspheres as sensors of mass and sound: Brownian motion as both signal and noise

by

Logan Edward Hillberry

DISSERTATION

Presented to the Faculty of the Graduate School of

The University of Texas at Austin

in Partial Fulfillment

of the Requirements

for the Degree of

DOCTOR OF PHILOSOPHY

THE UNIVERSITY OF TEXAS AT AUSTIN

May 2022

To Dale and Farley, my childhood dogs.

Acknowledgments

It is an honor to thank my supervisor, Professor Mark Raizen, for his kindness and mentorship as I pursued my degree. Shortly after visiting the University of Texas at Austin for the first time, I asked Mark if there would be a place in his group for a person with my skill set. Up until that point, I had not tried my hand at experimental physics research. Despite this, I remember sitting with my then-roommates eating hot wings when an email from Mark came into my inbox with the subject "Offer to join group." Before I read the message, I felt this was the right decision. Mark has excellent ideas that he freely shares with his students. He encourages us to follow our ideas and is always open to discussing the next steps for an experiment. Perhaps the key lesson I have learned from Mark is to keep track of what matters: What are we working towards in an experiment? Who will care? What applications might the results affect? To help us learn what matters, Mark encourages attendance at weekly seminars, asking questions, and reading diverse papers. Beyond his research mentorship, Mark is a deeply caring and kind person. Together, these qualities make Mark a standout leader from whom I am grateful to learn from.

I entered the group to work on novel atomic cooling methods. Of course, I knew nothing about regular cooling methods—except, perhaps, the office refrigerator keeping the mold at bay from my ham sandwich— let alone

novel ones. Initially, I was intimidated. At weekly group meetings, I would hear Mark ask questions to senior students like Kevin and Yu, questions that made me think, "Oh no, I have no idea what that means." Then, I would hear would Kevin or Yu respond, unalarmed, in a way that suggested that they not only understood the question but had the answer. I wondered how I would get there. What would I learn so deeply? What numbers would be on the tips of my fingers? In a certain way, it is hard to believe I now have an answer to those thoughts. The reality is: what I know, how I think, and, therefore, who I am originate from the influences of friends, colleagues, and mentors before and during my graduate studies. I am delighted to reflect on these people in what follows.

I joined Mark's group at the same time as Yi, Jordan, and Alex. It is hard to be the new person in a group and I am thankful we faced that challenge together. I began working on a team project to decelerate a supersonic beam of lithium using an adiabatic moving trap coil gun. We were affectionately known as the Slower Team, which sometimes offered comedic relief and other times was perhaps too portentous. Other projects in the group were somewhat smaller, but the people had a major impact on my time. Georgios and Igal each led largely independent efforts, but were always there to lend a hand or give sound advice. Ahmed worked as a postdoc on several experiments in the group. He generously offered his experience to help me troubleshoot on numerous occasions. Erik and Jamie worked as a duo. Jamie graduated soon after I arrived, but his casual brilliance inspired me. Erik and I became close

over weekly lunch outings where we ate head-sized burritos and did our best to remain productive for the rest of the afternoon.

Two postdocs on the Slower Team brought leadership to our efforts. Harry had previous experience in an atomic physics lab and he taught me many practical skills, like aligning an AOM and sealing a vacuum chamber. On my very first day in the lab, I asked Harry if there was anything I could do to help. He said "Hand me that flange." To which I could only reply "What's a flange?"

Pavel showed me the value of thinking. Initially, I was very excited to go to the lab early to get the experiment started. Pavel showed me that it is not always useful to take the same data every day. One has to think up something new to try to find a new angle on troubleshooting. Pavel giving me this early lesson in the balance of thinking and doing in the lab setting has informed my approach to research.

In addition to postdocs Harry and Pavel, the Slower Team was headed up by senior graduate students Yu, Lukas, and Kevin. Yu taught me many practical lab skills, particularly with optics. From fiber coupling to laser locking to the table layout, Yu's guidance still plays in my head while I work at an optics table. Lukas, Yu, and I all bonded over a passion for open-source software and living life in the command line. Of the many fellow graduate students I have learned from, special recognition goes to Kevin. I cannot conjure a single experimental skill that I have developed that was not in some way influenced by Kevin. He taught me to use CAD software, make mechanical

drawings, and then machine them; he taught me how to design circuits and print them; how to use LabView for data acquisition and experimental control; and many other finer skills. Despite having graduated years ago, I still frequently call Kevin asking where one piece of equipment or another might be tucked away in the lab. At a certain point, Yi joined the Slower Team. Progress continued while the postdocs moved on and the senior students all graduated. Near the end of the project's funding cycle, Yi and I shared a great personal achievement when, one late night of running the experiment, we finally slowed the supersonic lithium beam and confined it in a magneto-optical trap. Though the final trapping stage was standard technology, Yi and I quite literally jumped with joy at the sight of a small laser-illuminated ball of cold lithium gas. I am thankful to have shared the moment with Yi after we both worked hard for the result. To me, that night marked the close of the first half of my graduate research and the beginning of the second half.

Three years in, I switched projects to begin working on the laser trapping of microspheres in air. The project had a history in our group, but the experiment had just entered a rebuilding phase led by Diney, a postdoc in the group. We learned a lot together and his careful attitude toward experiments and theory worked well with me. Diney taught me the importance of consistency. An optical trap isn't built in a day. It takes the integral of many small steps dt for progress to accumulate in experimental physics. For my first lead-author publication, Diney was a terrific co-author guiding me through the process. I am thankful for all of the coauthors on this publication: Yi,

Sebastian, Gabriel, Julia, and, of course, Mark.

More recently, Aaron has joined our group as a graduate student and Ajith as a postdoc. I am very impressed by Aaron's quick start-up time in the lab and the ease with which he has taken on shared lab responsibilities. Aaron will have a very successful career that I look forward to following. Ajith has brought a wealth of skills and good energy to our group. I greatly anticipate following his projects long after I depart Austin, and also learning as much as I can from him before that.

At nearly the same time that I was leading the manuscript with the help of Diney, another back-burner project that followed me from my master's research also entered a writing phase. My former advisor, Professor Lincoln Carr at the Colorado School of Mines, maintained contact with me after graduation and encouraged me to publish some of the results in my masters thesis. I am thankful for his tenacity and excitement about the work that kept me inspired to complete the project across nights and weekends. Many coauthors gave me confidence in the work's technical merit and I am lucky to have learned from them: Matt, David, Patrick, Ning, Simone N., and Professor Simone Montenegro. I give special thanks to Professor Nicole Yunger Halpern who provided me with much-needed guidance during the writing and peer-review process. I have yet to encounter a physics author with as much clarity in both thought and communication as Nicole, and I appreciate her support and role in securing multiple speaking opportunities for me. After our first paper, I was a coauthor on an experimental follow-up where I learned much from coau-

thors Eric J., Mina, Pedram, Zhang, Alan, Eric O., and Peter (among others already mentioned). Though distinct from optical trapping, this side project on quantum many-body dynamics has helped me keep my physics interests broad, honed my computational skills, and strengthened my network of collaborators. These benefits not only impacted my Ph.D. work, but I expect them to follow me far beyond graduation.

Just before endeavoring to report my optical trapping experiments in the present document, Mark put me on a plane to France for a month-long summer school at L'École de Physique des Houches. The program was called "The New Mechanics" and focused on optical nano-mechanics of spheres, strings, and drums. A picturesque view of Mont Blanc from my chalet's window would have been enough inspiration, but the brilliant students and dedicated speakers made the 7-hour lecture days not only tolerable but incredibly engaging. I am grateful to Professors Cohadon, Krenner, and Verlot for organizing the school and for encouraging conversations about our sound detection experiments with Professors Ciliberto, Giseble, Dykman, Reynaud, and Ekinci. Thanks also to Chef Grégorie for two three-course meals per day and for letting me play chef by helping with dinner for the school. My written notes from this summer school proved very valuable while preparing this dissertation. Soon, the school's lecture notes will be published (Session CXX, held August 2022).

In addition to the many great physicists I have learned from, numerous support staff at the University of Texas at Austin have made my journey possible. I would like to recognize administrative assistance from Olga at the

Center for Nonlinear Dynamics and Belle at the Center for Complex Quantum Systems. Thanks also to Brant in the purchasing department, Dale in accounting, the department's Graduate Coordinator Matt, and the Graduate Advisors Professors Keto and Fitzpatrick. Additionally, it was a privilege to work with the many talented machinists and technicians in the department's machine shop and cryogenics lab: I especially thank Allan, Kenny, Ed, and Jack for their patience and wisdom.

Finally, it is hard to put into words my gratitude towards the friends, family, and loved ones that helped maintain my sanity across seven years of graduate school. My friends Dan and Aaron, hailing from the department's 14^{th} floor, have been with me since my first day in Austin. Daily lunch outings, weekend trips to the movies, long-haul board games, and the occasional night on the town helped me stay grounded in reality. They are two defining friendships that I look forward to maintaining in the coming years. Friendships with Ace, Greg, Luc, Natalie, Brant, Marc, Matt, and many others brightened my time in the department, and I cannot wait to see what they accomplish.

My parents Jeff and Vicki have loved and encouraged me my whole life. It is fascinating to see how I have become so like them. I know my dad and I share some internal wiring based on how we perceive the wonder of nature, how we approach our work with focus and dedication, and how we are not quite sure of the difference between August and September when making long-term plans. I see myself in my mother in how we share our love through cooking, our motivation to check tasks off the to-do list soon

after they're added, and our strong vision for what we want for ourselves, our families, and our community. My sister Taylor and I are also so alike, from our regressive music preferences to simultaneously cracking the same joke when we are together. Her ability to run her own business — and have a whole lot of fun doing it — inspires me to approach my work with a light-hearted and self-confident touch. My grandparents Ruth and Darwin have supported me both emotionally and financially through graduate school. I am so fortunate to have them in my life today and to have grown up spending summers gardening with grandma and going to "the shop" with grandpa, where I tore apart old electronics and learned about resistors and capacitors.

Then there is my girlfriend, Kate. We met in October 2019 and have spent essentially every day together since. All we do is have fun and grow. We have been partners through the challenges of a global pandemic and the challenges of interior decorating. Her love of life, be it plants, animals, or people, moves me to a place of contentment and happiness. I am thankful for her patience and support while finishing my degree while writing this document, and beyond. I can't wait to see what we do next.

Optically trapped microspheres as sensors of mass and sound: Brownian motion as both signal and noise

Publication No. _____

Logan Edward Hillberry, Ph.D.
The University of Texas at Austin, 2022

Supervisor: Mark G. Raizen

Owing to their small size, advanced position detection possibilities, and accurate theoretical description, optically trapped microspheres have become a paradigmatic system for myriad sensing applications. This dissertation reports on two air-based experiments that leverage the unique properties of optically-trapped microspheres as measurement tools: inertial mass sensing and sound detection.

We measure the mass of a microsphere in three ways. Careful error analysis allows quantitative comparison between our method and others appearing in the recent literature. As figures of merit, we focus on accuracy, precision, and speed. We find that monitoring the variance of the microsphere's velocity degree of freedom while undergoing equilibrium Brownian motion enables measurement of our microsphere's $\sim$25 pg mass with 4.3% accuracy and 1.6% precision across 14 vastly different trapping laser powers and using 10$\times$ less

data than our most accurate (3.2%) and precise (0.9%) method. The more accurate method is a calibration step that must always be performed initially, but the microsphere's velocity variance may subsequently be monitored, thereby elevating mass to a dynamic measurement variable.

For sound detection, we develop a model for the sensitivity of a microsphere's velocity to an external acoustic perturbation. In this case, the microsphere's Brownian motion is a noise source that must be overcome for a signal to be detectable. We validate our method by comparing measurements of pure-tone bursts between our system and two state-of-the-art, commercially-available acoustic sensors. We then demonstrate the microsphere's advantage in measuring high-frequency-content signals using impulsive sounds generated by laser ablation. We resolve an acoustic rise time of 1 µs on the same signal that our high-bandwidth microphone measures a 7 µs rise time. At the same time, our higher bandwidth resolves a nearly 3× larger peak pressure than the microphone.

This dissertation builds toward these two experimental results by first contextualizing them in a non-technical historical review. Key technical background is then developed pedagogically, followed by details of the trapping and detection apparatus. After the experiments are reported, we conclude with a summary of the results and an outlook on the future of optically trapped microspheres as sensitive detectors.

Table of Contents

List of Tables

List of Figures

Chapter 1

Introduction

In this work, the system under study is a small glass sphere with a diameter roughly $1/10^{\text{th}}$ the width of a human hair. The *microsphere* is *optically trapped* in air using two tightly-focused laser beams, as pictured in Figure 1.1. The position of the microsphere can be measured with a sub-nanometer spatial resolution and microsecond temporal resolution. Novel air-based sensing applications are enabled by such high-speed and sensitive position measurements.

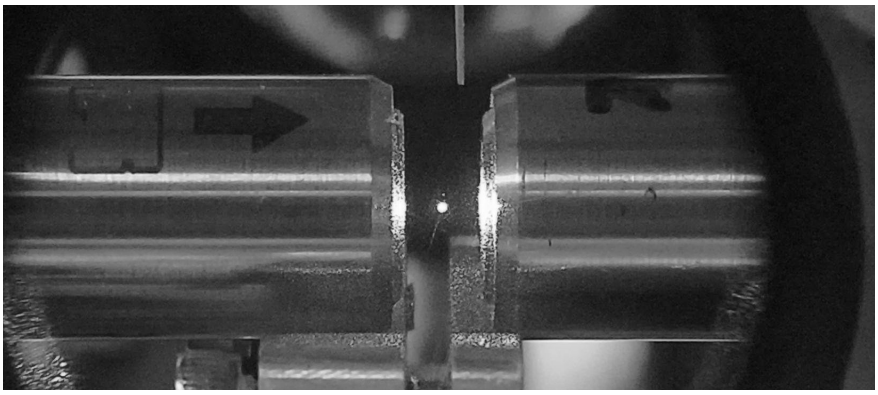

Figure 1.1: An optically trapped microsphere. Two counter-propagating laser beams are focused to a common point by lenses, seen here in their metal housing. A glass slide coated in microspheres just above the trap center is vibrated to affect their release. Once trapped, the microsphere scatters light making it appear much larger than it is.

Because the microsphere is held in air, it is coupled to an environment and therefore sensitive to environmental perturbations. Even in the absence of airflow, the air's temperature drives the microsphere in perpetual *Brownian motion*, like that simulated in Figure 1.2. Upon magnifying Brownian motion in space and time, one finds yet more randomness — Brownian motion appears scale-free and fractal. Upon further magnification, the random motion becomes a smooth trajectory. Our system is capable of resolving the smooth trajectory of Brownian motion and can, in this sense, be thought of as a microscope in both space and time.

We explore our system's ability to make two qualitatively-distinct analytic measurements. First, we monitor the microsphere's Brownian motion to deduce its mass. In the second, we monitor the microsphere's motion when the surrounding air is driven by sound. Brownian motion is present in both mass and sound measurements but its role as signal or noise is interchanged.

Much of the remainder of this Chapter will provide additional context for optical trapping and Brownian motion. We then briefly introduce the mass and sound sensing experiments that comprise the primary results reported herein. At the end, a high-level outline of this dissertation will provide a road map for what is to come.

1.1 History as context

Optical trapping and Brownian motion are concepts situated deeply within history and scientific literature. We will examine segments of each

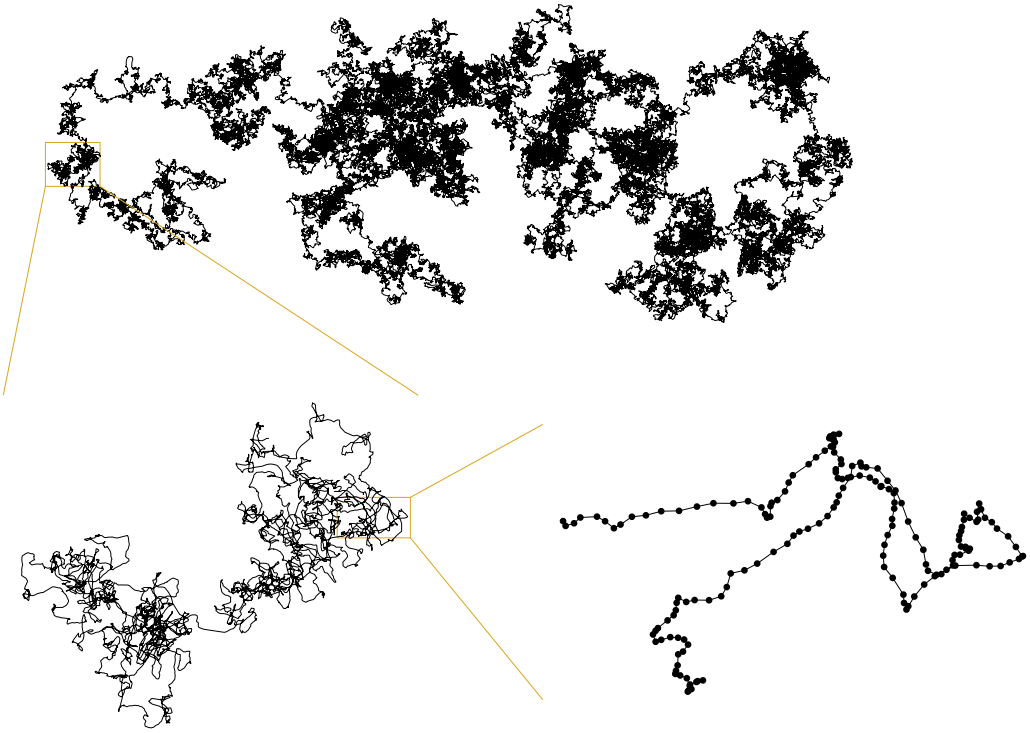

Figure 1.2: Two-dimensional Brownian motion trajectory at different scales of space and time. The upper black trace shows 10 seconds of simulated Brownian motion. Each successive magnification corresponds to a 100× shorter time trace. The original and first level of magnification depicts the random and fractal nature of Brownian motion at large scales. The final level of magnification depicts a portion of the underlying smooth trajectory.

concept's history to better contextualize our work that follows.

1.1.1 Optical trapping

The idea that light can influence the motion of matter can be traced back to at least 1619 [1]. To explain the observation that a comet's tail always points away from the sun, Johannes Kepler hypothesized that solar rays exert a pressure [2]. A proper first-principles prediction of *radiation pressure* didn't arrive until over two and a half centuries later. In 1873, James Clerk Maxwell published his Treatise on Electromagnetism [3]. In Chapter XX, Maxwell used his theory of electromagnetism to deduce that light exerts a pressure: "Hence in a medium in which waves are propagated there is a pressure in the direction normal to the waves, and numerically equal to the energy in unit of volume." The same conclusion was arrived at independently by Bartoli based on thermodynamic cycles [4]. In Bartoli's thought experiment, light reflected from moving mirrors could be used to transfer energy from a cooler body to a warmer body without the expenditure of work, in violation of the second law of thermodynamics. Bartoli calculated the pressure that light must exert to save the second law and the result agreed with Maxwell's [4].

In terms of everyday optical sources, radiation pressure is quite weak. Maxwell estimates that an intense ray of sun exerts a pressure of 4.2 µPa on an absorbing sheet. This is about a 5× smaller pressure than that of a barely audible sound. Owing to the relatively weak pressure exerted by terrestrial sources, the experimental verification of radiation pressure was met with chal-

lenges. Indeed, early experimental efforts led by De Mairan, Fresnel, and Crookes were all thwarted by residual gas heating effects [5]. Perhaps most famously, Crookes suggested in 1874 that radiation pressure could explain why a balance's measurements are influenced by optically radiation [6]. Further developments led to the Crookes radiometer, a partially-evacuated glass chamber in which four vanes, each with a black and silver side, are found to rotate upon illumination. It turns out that the measured "radiation" pressure was over 100 000× that predicted by Maxwell and Bartoli [5]. What's more, the vanes rotate in the opposite direction (black towards silver) compared to the direction of maximum radiation pressure (silver towards black). Instead of radiation pressure, the rotation of the Crookes radiometer is related to the optically-heated black surface driving the residual gas in the chamber. Successful measurements of radiation pressure were finally reported in 1901 by Lebedev[1] in a high vacuum environment [5] and by Nichols and Hull in a variety of lower-vacuum environments [7]. With modern technology, recent work [8] has measured the pressure of radiation by directly monitoring the elastic waves propagating in a mirror upon irradiation.

Despite the early challenges in even measuring optical radiation pressure, today, the effect is of immense importance at an impressively broad interdisciplinary scale. Like many aspects of science and technology, everything changed in 1960 with the invention of the laser [9]. Because the laser is

[1]Soloviev's English translation of Lebedev's paper was useful in reviewing the pre-1901 history of radiation pressure.

a special light source with high spatial coherence and spectral purity[2], it can be focused to an incredibly small spot size — on the order of radiation's wavelength. Thus, a 1 W light source, modest by laser standards, focused down to 1 µm corresponds to an irradiance of 10^{12} W/m^2, about 16 000× larger than the luminosity of the sun's entire surface over all wavelengths (about 6.4×10^7 W/m^2) [10]. Such an irradiance corresponds to a radiation pressure of 3.3 kPa. Acoustic pressures of this magnitude are typically only observed in shock waves produced by, e.g., explosions, firearms, and ruptured rubber pressure vessels (also known as party balloons) [11].

It was Ashkin and coworkers who ultimately unlocked the potential of radiation pressure as a means for manipulating matter [12]. Initially, micrometer-scale glass spheres suspended in water were observed to move in the propagation direction of a moderately focused beam. Because the water's viscosity imparts a velocity-dependent drag force and the radiation pressure exerts a constant pushing force, the microsphere moves at a constant velocity, akin to the terminal velocity of a skydiver. However, Ashkin also noted a wholly unexpected observation: the microspheres near the edge of the focused laser beam were attracted inward to the high-intensity focus in addition to being pushed along the propagation direction. This intensity-seeking force is now called the *gradient force* while the forward pushing force is called the *scattering force*. Despite only the scattering force being predicted and observed previously, the

[2]The spectral purity of an early iteration of the laser, the *maser*, was cause for some debate between one of its inventors, Townes, and towering theorists like Bohr and Von Neumann who asserted such a device could not be made [9].

gradient force has a simple explanation in the view of light as rays that carry momentum and refract upon entering a material. Furthermore, by applying two laser beams in a co-linear and counter-propagating configuration, the scattering forces cancel and particles can be stably trapped. A single vertical beam can also be used to stably levitate particles in air or water against the force of gravity [13] and a single very tightly focused, horizontal laser, sometimes called *optical tweezers*, can be used to form a stable trap [14].

In the same original paper [12], Ashkin hypothesized that single atoms could also be manipulated by laser beams if the frequency of light was tuned to an atomic resonance. Resonant light scatters from an atom as if its cross-sectional area were proportional to the light's wavelength squared, which is a few million times larger than the atom's physical cross-sectional area. Ashkin tested this hypothesis by creating an atomic beam velocity selector and isotope separator [15]. Building on this work, Hänsch and Schawlow suggested that the Doppler shifted frequency of light seen by an atom in motion combined with a slightly off-resonant laser beam could be arranged to cool atoms in a technique known today as optical molasses [16]. Ashkin also realized that by strongly detuning the laser by, say, 100× the width of the resonance, atoms could be stably trapped due to the presence of a gradient force. The full history of laser-matter interactions is well beyond the scope of this introduction, but it is worth noting the explosion of research that originated from Ashkin's first simple experiments. Multiple Nobel Prizes have been awarded in recognition of laser-based manipulation and interrogation of matter: invention of the laser (1964

Prize, Townes, Basov, and Prokhorov), atomic cooling and trapping (1997 Prize, Chu, Cohen-Tannoudji and Phillips), Bose-Einstein condensation (2001 Prize, Cornell, Ketterle, and Wieman), precision spectroscopy (2005 Prize, Hall, and Hänsch, shared with Glauber for the theory of optical coherence), and atoms as quantum systems (2012 Prize, Haroche and Wineland) [17]. Most recently, Ashkin was awarded a portion of the 2018 Prize for his bedrock work outlined above, shared with Mourou and Strickland for their work in pulsed laser amplification [17]. Today, advanced optical trapping techniques are used in neutral-atom-based quantum computing to make defect-free arrays of single atoms [18, 19].

Beyond atomic physics, Ashkin recognized the utility of optical trapping in biology. His early experiments demonstrated optical trapping of cells [20], bacteria[3], and viruses [22]. Trapping and manipulation of organelles within cells have revealed mechano- and viscoelastic-properties of life at the micro-scale with applications to genomic sequencing and *in vitro* fertilization [23].

From Kepler's initial hypothesis to Maxwell and Bartoli's theoretical predictions to Lebedev's and Nichols and Hulls' first measurements to Ashkin's nearly-exhaustive exploration, the story of radiation pressure is an archetype for scientific progression. Ashkin's trailblazing work set the vision for the field so strongly that if ever one has a new application idea for optical trapping,

[3]Bacteria were grown from coworker Dziedzic's ham sandwich [21].

one should first check that Ashkin has not already performed the experiment 50 years ago. Even still, since Ashkin, the flurry of research activity enabled by optical trapping, which continues to grow to this day, has fostered a large and interdisciplinary network.

1.1.2 Brownian motion

Snap! A wooden pencil, held above my head for the audience of school children cracks in half. "Is it still *stuff*?" I ask the audience. The gymnasium resonates in the affirmative. *Snap*, and the pencil is now broken down further. "Is it still stuff?" More affirmation. "What if I keep breaking and keep breaking the pencil, is it still stuff? What is the tiniest possible amount of stuff?" The school children respond "atom!"[4]. Perhaps surprisingly, school children no more than 10 years old have understood that the stuff of reality comes in indivisible packages, at least according to my physics outreach experience. Today, the existence of atoms, and even their sub-atomic constituents, is everyday knowledge. This has not always been the case, however, and the existence of atoms was once a topic of intense debate.

Though the idea of atoms and even the etymology of the word derives from antiquity[5], the mid-19$^{\text{th}}$ century marked the peak of the philosophical and scientific divide between the *continuists*, who believed matter could be divided infinitely, and the *atomists*, who believed matter is composed of dis-

[4]Other responses have included, dust, particle, wood, cell, molecule, and quark.

[5]Democritus used the Greek word *atomos* meaning "indivisible" for the smallest possible amount of stuff.

crete elements called atoms which bond into stable groups called molecules. Around this time (June-August 1827 to be precise), naturalist Robert Brown was observing small particles extracted from pollen grains and suspended on the surface of water. Brown observed the random and persistent motion of the particles. The eponym "Brownian motion" is used to describe such motion today despite similar observations made in the same year by Brongniart [24]. Even 131 years earlier, Gray observed "Globular forms in water" undergoing "swift, progressive, irregular motion" using one of the first-available microscopes [25]. However, these early observations supposed the motion was biological. Brown carried out additional observations on inorganic grains[6] and concluded the effect must not be biological, but he gave no further hypothesis.

In 1905 Einstein predicted that a small particle undergoing Brownian motion would slowly displace from its starting point [26]. A car driving down the highway at a constant velocity is displaced by an amount equal to its speed times the time spent driving, but Einstein derived that a Brownian particle's displacement increases with only the square root of time. The car's trajectory is referred to as *ballistic* while the Brownian particle's is *diffusive*. Shortly after Einstein's paper, Smoluchowski [27] and Langevin [28] gave alternative theoretical arguments with essentially the same conclusion: A Brownian particle diffuses away from its starting position due to random collisions with molecules. All three arguments were based on molecular kinetic theory and thus made a testable prediction different from the continuist hypothesis.

[6]Including a pulverized fragment of the Sphinx.

Convincing experimental evidence for the atomist's hypothesis was provided by Svedberg – in his 1907 doctor's thesis [29] – and Perrin [30] in 1909, finally settling the debate in favor of the molecular theory of nature. For this accomplishment, Svedberg was awarded the 1926 Nobel Prize in Chemistry and Perrin was awarded the 1926 Nobel prize in Physics. Interestingly, an early discussion on the connection between Brownian motion and molecular kinetic theory is provided by Delsaulx, who was inspired by the proper understanding of the movements of the Crookes radiometer [31].

Despite the success of Einstein and Perrin in conclusively establishing molecular reality, there was an obvious flaw in the theoretical description. Einstein predicted that the average increment of displacement x over a time interval t is $x = \sqrt{2Dt}$ where D is called the *diffusion constant*. Thus, the average velocity over the same increment and interval is $v = x/t = \sqrt{2D/t}$. Observe that v diverges to infinity as t decreases to zero. On the other hand, Einstein also knew from his special theory of relativity [32] that nothing could travel faster than light. In 1907 Einstein worked out the correct theory of Brownian motion [33].

The key insight was that at short enough time intervals the Brownian particle's trajectory becomes ballistic. The reason is that at such short time scales there are too few molecular collisions to redirect the particle's movement. With this theoretical understanding, Einstein predicted that the distance increment and time interval over which a Brownian particle's trajectory is ballistic are so small that they could never be observed. Indeed, the measurement

requirements for observing a Brownian particle's ballistic velocity are quite stringent: One must be able to measure position with sub-nanometer resolution within a few microseconds. However, over 100 years after Einstein's 1907 paper, our group met these measurement requirements are reported the first observation of a Brownian particle's ballistic velocity [34, 35].

1.2 Contributions and outline

The path one takes on the road toward research goals is rarely a straight one. Before and parallel to my experimental efforts detailed in this dissertation, I had the opportunity to consider a range of unrelated problems. These projects include novel atomic cooling methods [36], numeric simulation of quantum cellular automata [37], and analysis of their quantum dynamics observed on a superconducting quantum processor [38]. These efforts will not be discussed further here. Instead, a reference to "we" is understood to mean me, the author, my optical trapping and Brownian motion collaborators, and you, the reader.

The present work builds on our group's earlier efforts: the resolution of the microsphere's ballistic velocity is precisely what enables our two major sets of results.

The first set of results is obtained in thermal and mechanical equilibrium. In other words, we record the position of the microsphere as it undergoes Brownian motion due to collisions with air molecules. The system is calibrated by separately measuring the air temperature and particle diameter, and mak-

ing a few assumptions about the surrounding air medium. The full calibration reveals the trapped particle's mass, the trapping strength provided by the laser, and the detection system's voltage-to-distance calibration constant. Furthermore, we compare the accuracy and speed of three distinct particle mass measurement techniques. Leveraging our ability to measure the microsphere's instantaneous velocity leads to a desirable balance between speed and accuracy of mass measurement.

The second set of results pushes the microsphere out of equilibrium using the flow field of sound waves. The sounds generated by a small speaker or by pulsed laser-heating are detected in the microsphere's motion. In post-processing, the microsphere's motion is converted into the fluid's motion based on theoretical models and the results are compared to two state-of-the-art, commercially-available detectors. We again find that resolving the instantaneous velocity of the microsphere enables our measurement. Brownian motion still occurs in these experiments, but in the case of sound detection, it is a source of noise that must be overcome.

The remainder of this Dissertation is organized as follows: Chapter 2 lays out the theoretical models informing the analysis and interpretation of experimental data. Chapter 3 describes the apparatus in detail. Chapter 4 reports the results and discusses the significance of the two experiments outlined above. Finally, Chapter 5 summarizes this work and speculates on the future of optically trapped microspheres as analytic measurement tools.

Chapter 2

Technical Background

In this Chapter, we endeavor to detail much of the physics and mathematics needed to understand the results given in Chapter 4. Three main sections organize this broad content. First, Section 2.1 develops the theory of optical trapping. Second, Section 2.2 deals with signal analysis and defines all of the quantifiers used to analyze experimental data. Third, Section 2.3 develops the theory of Brownian motion. The final Subsection 2.3.4 discusses acoustics from a hydrodynamics perspective. Though not strictly related to Brownian motion, this subsection on acoustics fits naturally with Subsection 2.3.2 on hydrodynamic Brownian motion.

2.1 Optically trapping small spheres

Consider light as a collection of photons with the same wavelength $\lambda = 1\,\mu\text{m}$ and hence the same energy $E = hc/\lambda$ and momentum $p = h/\lambda$, where the speed of light is exactly $c = 299\,792\,458\,\text{m/s}$ and Planck's constant is exactly $h = 6.626\,070\,15 \times 10^{-34}\,\text{Js}$. A $P_0 = 15\,\text{mW}$ source generates a flux of $\dot{n} = P_0/E = P_0\lambda/hc \approx 7.5 \times 10^{16}\,\text{photons/s}$. If each photon is reflected from a small sphere, the light imparts a constant force of $F = 2p\dot{n} = 2P_0/c \approx 10^{-10}N$.

In contrast, a 1 µm-diameter silica sphere has a mass of approximately 10^{-15} kg and hence a weight of approximately 10^{-14} N. According to this order-of-magnitude estimate, the optical forces at play are significantly stronger than the gravitational forces. In the remainder of this section, we will develop three different models for calculating the forces of an optical trap. Section 2.1.1 uses the ray optics approximation, Section 2.1.3 uses the dipole approximation, and Section 2.1.4 considers Mie scattering calculations.

2.1.1 Ray optics picture

When the wavelength of light λ is much smaller than the characteristic size of any object in the light's path, then the light can be considered as traveling in a straight line from its origin to the interface of the object. In this *geometric optics* regime, wave effects like diffraction and interference are ignored and light is modeled as a collection of *rays*. In this section, we will show that ray optics offers an intuitive understanding of optical trapping and even allows quantitative force calculations through numeric ray tracing.

To begin, let us define a ray by the tuple $\vec{q} = \{\mathbf{o}, \hat{\mathbf{k}}, P\}$ that includes the ray origin $\mathbf{o}$, its unit-propagation direction $\hat{\mathbf{k}}$, and its optical power P in units of W. One may parameterize the propagation of a ray by a vector of length d according to

$$\mathbf{q}(d) = \mathbf{o} + d\hat{\mathbf{k}}\,. \tag{2.1}$$

Consider a ray $\vec{q}$ traveling in a medium of refractive index n_1 towards a region or object $\mathcal{R}$ of refractive index n_2. The surface of the object is the

collection of points comprising its boundary: $\mathcal{S} = \{\mathbf{r}_\mathrm{s} \in \partial\mathcal{R}\}$. At some distance d_0, the ray intersects the surface at the point $\mathbf{q}(d_0) \in \mathcal{S}$.

Take as a specific object a sphere of radius R centered at $\mathbf{c}$. This object's surface is defined by

$$|\mathbf{r}_\mathrm{s} - \mathbf{c}|^2 = R^2\,, \tag{2.2}$$

and its outward normal is

$$\hat{\mathbf{n}}(\mathbf{r}_\mathrm{s}) = \frac{\mathbf{r}_\mathrm{s} - \mathbf{c}}{|\mathbf{r}_\mathrm{s} - \mathbf{c}|}\,. \tag{2.3}$$

The intersection distance d_0 of a ray $\vec{q}$, if it exists, is found by solving Equation (2.2) subject to $\mathbf{r}_\mathrm{s} = \mathbf{q}(d_0)$. The resulting quadratic equation yields

$$d_0^{(1,2)} = -\alpha \pm \sqrt{\alpha^2 - \beta}\,, \tag{2.4}$$

$$\alpha = (\mathbf{o} - \mathbf{c}) \cdot \hat{\mathbf{k}}\,, \quad \beta = |\mathbf{o} - \mathbf{c}|^2 - R^2\,. \tag{2.5}$$

When $\alpha^2 - \beta > 0$, the ray intersects the sphere at two points which we may order $d_0^{(1)} < d_0^{(2)}$. When $\alpha^2 - \beta \leq 0$, the ray does not intersect the sphere. Upon incidence, a ray $\vec{q} = \{\mathbf{o}, \hat{\mathbf{k}}, P\}$ is scattered into a reflected ray and a transmitted ray

$$\vec{q}_\mathrm{r} = \{\mathbf{q}(d_0^{(1)}), \hat{\mathbf{k}}_\mathrm{r}, R_\sigma P\}\,, \tag{2.6}$$

$$\vec{q}_\mathrm{t} = \{\mathbf{q}(d_0^{(1)}), \hat{\mathbf{k}}_\mathrm{t}, T_\sigma P\}. \tag{2.7}$$

We next turn define the transmitted and reflected ray propagation directions and ray powers.

The law of reflection states that the angle θ_1 between $\hat{\mathbf{n}}\left[\mathbf{q}(d_0^{(1)})\right]$ (called $\hat{\mathbf{n}}$ below for brevity) and $\hat{\mathbf{k}}$ is the same as the angle between $\hat{\mathbf{n}}$ and $\hat{\mathbf{k}}_r$. Snell's law of refraction states that the angle θ_1 is related to the angle θ_2 between $-\hat{\mathbf{n}}$ and $\hat{\mathbf{k}}_\mathrm{t}$ according to $n_1 \sin\theta_1 = n_2 \sin\theta_2$. From these laws and trigonometric identities, one finds

$$\hat{\mathbf{k}}_\mathrm{r} = \hat{\mathbf{k}} + 2c_1\hat{\mathbf{n}}\,, \tag{2.8}$$

$$\hat{\mathbf{k}}_\mathrm{t} = \frac{n_1}{n_2}\hat{\mathbf{k}} + \left(\frac{n_1}{n_2}c_1 - c_2\right)\hat{\mathbf{n}}\,, \tag{2.9}$$

were we have defined

$$c_1 = \cos\theta_1 = \hat{\mathbf{k}}\cdot(\pm\hat{\mathbf{n}})\,, \tag{2.10}$$

$$c_2 = \cos\theta_2 = \sqrt{1 - \frac{n_1^2}{n_2^2}(1-c_1^2)}\,. \tag{2.11}$$

The sign in Equation (2.10) is to be chosen such that $c_1 > 0$ and that choice of sign for $\hat{\mathbf{n}}$ propagates through Eqs. (2.8) and (2.9).

The *Fresnel coefficients* R_σ and $T_\sigma = 1 - R_\sigma$ scale the reflected and transmitted ray's power (respectively) relative to the incident ray's power. $\sigma \in \{s, p\}$ defines the incident ray's polarization, discussed further in Section 2.1.2. The Fresnel coefficients are

$$R_s = \frac{n_1c_1 - n_2c_2}{n_1c_1 + n_2c_2}\,, \tag{2.12}$$

$$R_p = \frac{n_1c_2 - n_2c_1}{n_1c_2 + n_2c_1}\,. \tag{2.13}$$

The above ingredients sufficiently define rays and spheres for *ray tracing*. Ray tracing for a sphere works as follows: Given an initial ray $\vec{q}_0 = \{\mathbf{o}_0, \hat{\mathbf{k}}_0, P_0\}$, a sphere's radius R and center $\mathbf{c}$, and the refractive indices of the medium n_1 and sphere n_2:

1. Find the first intersection $\mathbf{q}_0(d_0^{(1)})$

2. Compute the elements of the first reflected ray $\vec{q}_{\mathrm{r}1}$ and store it in a set of *external rays*.

3. Compute the elements of the first transmitted ray $\vec{q}_{\mathrm{t}1}$ and store it as the current internal ray $\vec{q}_{\mathrm{int}}$.

4. Compute the *second* intersection $\mathbf{q}_{\mathrm{int}}(d_{\mathrm{int}}^{(2)})$ of the current internal ray. For numeric stability, shift the internal ray's origin off the surface by a small amount ϵ in the direction normal to its origin.

5. Compute the transmitted ray arising from the intersection of the current internal ray and store it in the set of external rays. Note that while working from internal rays, the roles of n_1 and n_1 are reversed.

6. Compute the reflected ray arising from the intersection of the current internal ray and set it as the new current internal ray.

7. Repeat the previous three steps N times to account for N multiple internal reflections within the sphere.

After concluding the above ray tracing algorithm, we have constructed a set of external rays $Q(\vec{q}_0) = \{\vec{q}_{\mathrm{r}1}, \vec{q}_{\mathrm{t}i}\,, i = 2, \ldots N+2\}$. Since a ray transfers momentum along $\hat{\mathbf{k}}$ at a rate $n_1 P/c$, where c is the speed of light, ray tracing gives the force exerted on the object as

$$\mathbf{F}\left[\vec{q}_0, Q(\vec{q}_0)\right] = \frac{n_1}{c}\left(P_0\hat{\mathbf{k}}_0 - P_{\mathrm{r}1}\hat{\mathbf{k}}_{\mathrm{r}1} - \sum_{i=2}^{N} P_{\mathrm{t}i}\hat{\mathbf{k}}_{\mathrm{t}i}\right). \tag{2.14}$$

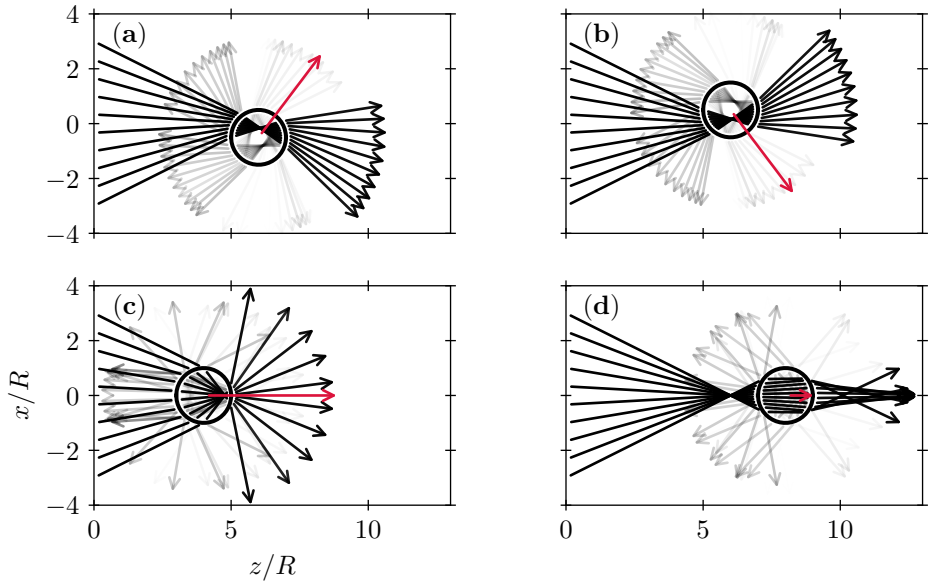

Figure 2.1: Tracing rays (black lines) yields a net force (red arrows). $N = 3$ internal scattering events are included for each ray. The transverse force (**a**) points upwards when the sphere is below the optical axis, and (**b**) points downwards when above the optical axis. The longitudinal force always points along the direction of the incoming beam, but (**c**) increases when the sphere is in front of the focus, and (**d**) decreases behind it.

.

Finally, to simulate optical trapping of a sphere we may calculate the net force caused by a set of M initial rays $\vec{q}_j$, $j = 1, 2, \ldots M$, that model a

focused beam. In Figure 2.1 we show a two-dimensional example consisting a sphere of radius R centered at $(z_0, x_0)^{\mathrm{T}}$ and a focused beam of $M = 10$ rays originating from $\mathbf{o}_j = (-5R, x_j)^{\mathrm{T}}$ with $x_j \in [-3R, 3R]$ and pointing towards $(0, 0)^T$. The beam power P_0 is split evenly among the beams according to $P_j = P_0/M$. As the sphere is moved above or below the beam axis, there is a gradient force driving the sphere back towards the optical axis. No matter where the sphere is moved, there is always a scattering force pointing along the optical axis. The scattering force increases when the sphere is behind the focus and decreases when the sphere is in front of the focus due to the gradient effect in the longitudinal direction. Figure 2.1 is computed assuming the trapping medium is air ($n_1 = 1$) and the sphere is silica ($n_2 = 1.47$) for which the longitudinal force never reaches zero, implying an unstable trap. We solve this problem in our experiment by aligning a second beam counter-propagating to the first to cancel the longitudinal scattering forces.

In Figure 2.2 we show the longitudinal and transverse force components when spheres of various radii are moved through the beam. In particular, we consider $F_z(z, x = 0)$ and $F_x(z = 0, x)$. The beam is comprised of 500 rays originating from $(-f, x_0)^{\mathrm{T}}$ and pointing towards $(0, 0)^{\mathrm{T}}$, where $f = 3\,\mathrm{mm}$ and $x_0 \in [-1\,\mathrm{mm}, -1\,\mathrm{mm}]$ (equivalent to a numeric aperture of 0.33). As observed in Figure 2.2, the longitudinal force never reaches zero. The transverse force is approximately linear near the focus and so has a quadratic potential $U = \kappa_x x^2/2$. According to this ray optics calculation, the transverse trap strength κ_x monotonically decreases with increasing sphere radius R.

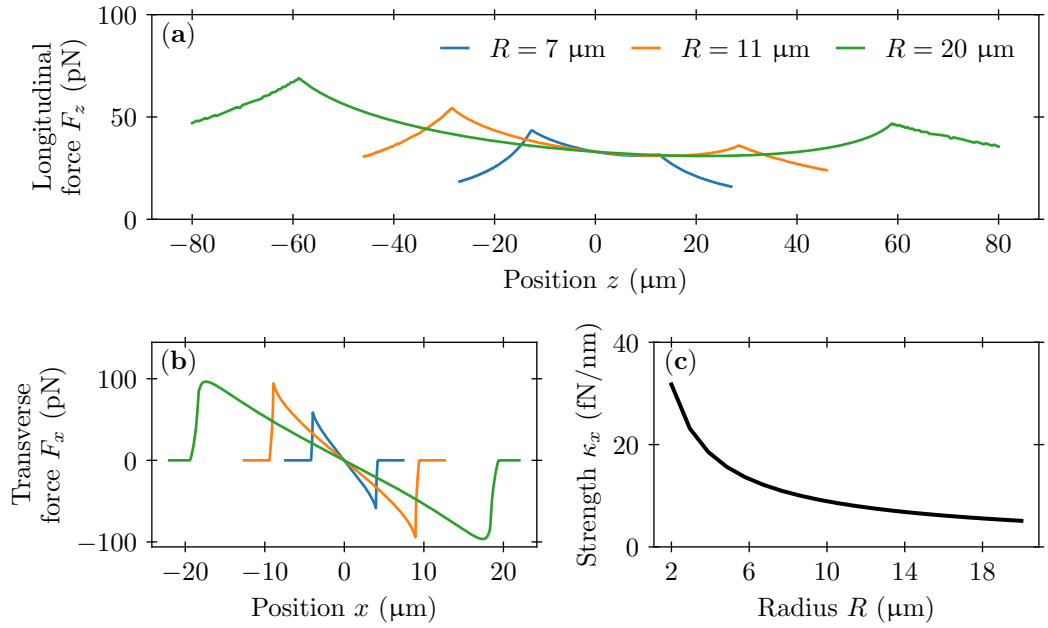

Figure 2.2: The (**a**) longitudinal ($x = 0$) and (**b**) transverse ($z = 0$) trapping forces are shown as a function of a sphere's position $(z, x)^{\mathrm{T}}$ and radius R. (**c**) The transverse trap strength κ_x, determined by linear fits near the trap center. This calculation uses s-polarization, a total power of $P_0 = 50\,\mathrm{mW}$, $n_1 = 1$, and $n_2 = 1.47$.

To summarize, it is sufficient to treat light as a ray so long as light's wave nature is irrelevant. Rays are deflected upon scattering from an object's surface and since light carries momentum the object experiences a force. Tracing rays through an object and tracking their deflections allows one to make quantitative force calculations. We found that micron-scale spheres can be transversely bound to a focused beam of light. The binding is approximately harmonic with strength on the order of a couple of 10s of fN/nm. For silica spheres in air, the longitudinal force never reaches zero and hence the sphere is unbound in the longitudinal direction. Despite the simple nature of the ray

optics picture, more advanced techniques recover mostly the same conclusions as above. While the ray optics calculations are accurate for $R \gg \lambda$, our next goal is to introduce an accurate approximation in the opposite regime $R \ll \lambda$. Before detailing the next approximation, we will first introduce the formalism of light as an electromagnetic wave.

2.1.2 Light localization and Gaussian laser beams

As shown by Maxwell [3], the electromagnetic field supports wave solutions. Light is identically an electromagnetic wave. In this section, plane-wave solutions of the electromagnetic field are derived and interference of multiple plane waves is shown to localize light intensity. The Gaussian beam model of localized light is given towards the end.

We begin with Maxwell's equations for the electric field $\mathbf{E}(\mathbf{r}, t)$ and the magnetic field $\mathbf{B}(\mathbf{r}, t)$ at time t in a region $\mathbf{r} \in \mathcal{R}$ that is absent of charge density and current density:

$$\nabla \cdot \mathbf{E} = 0\,, \tag{2.15}$$

$$\nabla \cdot \mathbf{B} = 0\,, \tag{2.16}$$

$$\nabla \times \mathbf{E} = -\frac{\partial \mathbf{B}}{\partial t}\,, \tag{2.17}$$

$$\nabla \times \mathbf{B} = \mu_0 \epsilon_0 \frac{\partial \mathbf{E}}{\partial t}\,, \tag{2.18}$$

where $\mu_0 \approx 1.256\,637\,062\,12 \times 10^{-6}\,\mathrm{N/A^2}$ is the permeability of free space and $\epsilon_0 \approx 8.854\,187\,812\,8 \times 10^{-12}\,\mathrm{F/m}$ is the permittivity of free space. Taking the

curl of Equation (2.17) and using the vector identity [1] $\nabla \times (\nabla \mathbf{A}) = \nabla(\nabla \cdot \mathbf{A}) - \nabla^2 \mathbf{A}$ gives

$$-\frac{\partial}{\partial t}(\nabla \times \mathbf{B}) = \nabla(\nabla \cdot \mathbf{E}) - \nabla^2 E\,. \tag{2.19}$$

Substitute Equation (2.18) on the left-hand side and Equation (2.15) on the right-hand side in the above to find the *wave equation*

$$\left[\nabla^2 - \frac{1}{c^2}\frac{\partial^2}{\partial t^2}\right]\mathbf{E}(\mathbf{r},t) = \mathbf{0}\,, \tag{2.20}$$

where the $c = 1/\sqrt{\mu_0 \epsilon_0}$ is the speed of light.

When the light field is monochromatic (i.e. laser light consisting of a single angular frequency ω) the time dependence of the electric field may be factored out: $\mathbf{E}(\mathbf{r},t) = \mathbf{E}(\mathbf{r})e^{-i\omega t}$. It is understood that the real part of the complex field is the physical quantity: $\mathrm{Re}\,[\mathbf{E}(\mathbf{r},t)]$. Separating variables and introducing the separation constant $-k^2$ leads to the *vector Helmholtz equation*

$$\left[\nabla^2 + k^2\right]\mathbf{E}(\mathbf{r}) = \mathbf{0}\,, \tag{2.21}$$

and the *dispersion relation* $k = \omega/c$. Each of the three $i \in \{x, y, z\}$ components $E_i(\mathbf{r})$ of $\mathbf{E}(\mathbf{r})$ satisfy the scalar Helmholtz equation. Separating the spatial variables in Cartesian coordinates as $E_i(\mathbf{r}) = A_i(x)B_i(y)C_i(z)$ leads to

$$\frac{1}{A_i}\frac{\mathrm{d}^2 A_i}{\mathrm{d}x^2} + \frac{1}{B_i}\frac{\mathrm{d}^2 B_i}{\mathrm{d}y^2} + \frac{1}{C_i}\frac{\mathrm{d}^2 C_i}{\mathrm{d}z^2} = -k^2\,, \tag{2.22}$$

[1] Using the Einstein summation convention, the completely antisymmetric Levi-Civita symbol ε_{ijk}, and the Kronecker-delta δ_{ij}: $[\nabla \times (\nabla \times A)]_k = \varepsilon_{ijk}\partial_i(\epsilon_{jmn}\partial_m A_n) = -\varepsilon_{jim}\varepsilon_{jmn}\partial_i\partial_m A_n = (\delta_{in}\delta_{km} - \delta_{im}\delta_{kn})\partial_i\partial_m A_n = \partial_k\partial_n A_n - \partial_m\partial_m A_k = [\nabla(\nabla \cdot A) - \nabla^2 A]_k$.

in which each term on the left-hand side depends on only one spatial variable, yet the right-hand side is a constant. Hence, each left-hand side term is individually equal to a constant:

$$\frac{\mathrm{d}^2 A_i}{\mathrm{d}x^2} = -k_x^2 A_i \,, \quad \frac{\mathrm{d}^2 B_i}{\mathrm{d}y^2} = -k_y^2 B_i \,, \quad \frac{\mathrm{d}^2 C_i}{\mathrm{d}z^2} = -k^2 C_i \,, \tag{2.23}$$

$$k_x^2 + k_y^2 + k_z^2 = k^2 \,. \tag{2.24}$$

Solutions to Equation (2.23) are of the form $E_i(\mathbf{r}) = E_{0i} e^{i\mathbf{k}\cdot\mathbf{r}}$ where $\mathbf{k} = (k_x, k_y, k_z)^{\mathrm{T}}$ is normal to planes of constant $E = |\mathbf{E}|$. Thus, we have found *plane wave solutions* of the electric field

$$\mathbf{E}(\mathbf{r}, t) = \mathbf{E}_0 e^{i(\mathbf{k}\cdot\mathbf{r} - \omega t)} \,, \tag{2.25}$$

$$k_x^2 + k_y^2 + k_z^2 = \frac{\omega^2}{c^2} \,. \tag{2.26}$$

To gain further insight into this solution let us set the coordinate system so that $k_y = 0$ and the incident angle of $\mathbf{k}$ with respect to the z-axis is θ. Then, $\mathbf{k} = (k\sin\theta, 0, k\cos\theta)^{\mathrm{T}}$. Equation (2.15) demands $\mathbf{k}\cdot\mathbf{E} = 0$, so we may write

$$\mathbf{E}(\mathbf{r}) = E_0 \begin{pmatrix} \cos\phi\cos\theta \\ \sin\phi \\ -\cos\phi\sin\theta \end{pmatrix} e^{ik(x\sin\theta + z\cos\theta)} \,, \tag{2.27}$$

where ϕ is the *polarization angle*. $\phi = 0$ is known as p-polarization and $\phi = \pi/2$ is known as s-polarization. Together, the p- and s-polarization components form an orthogonal basis for the possible electric field vector orientations ϕ given an angle of incidence θ. Let us choose $\phi = \pi/2$ so that the only nonzero component is

$$E_y(x, z; \theta) = E_0 e^{ik(xsin\theta + zcos(\theta))} \,. \tag{2.28}$$

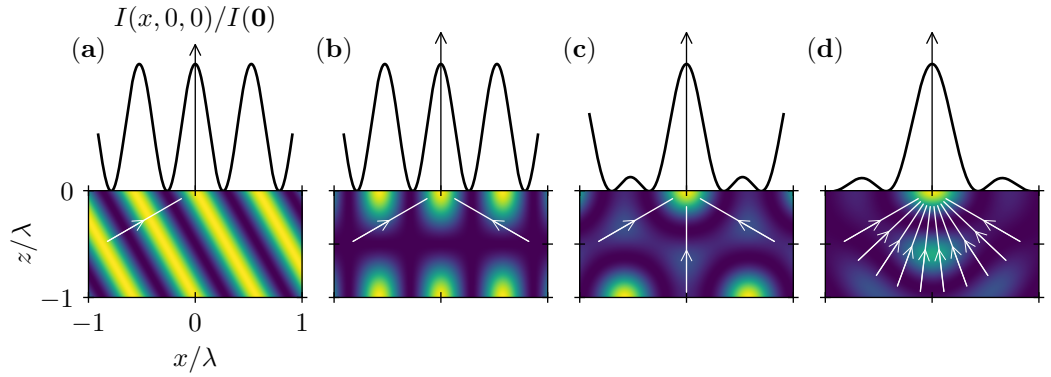

Figure 2.3: The lower portion of each panel shows $I(x, 0, z)$ with low intensity colored purple and high intensity colored yellow. The white arrows points along $\mathbf{k}$ of incident plane waves. The upper portion of each panel shows $I(x, 0, 0)$. x and y are in units of the wavelength $\lambda = 2\pi/k$ and I is in units of its maximum value. (**a**) The intensity distribution of a single plane wave incident at angle $\theta = \pi/3$. (**b** - **d**). The intensity distribution of multiple plane waves incident at equidistant angles between $-\pi/3$ and $\pi/3$.

Figure 2.3 (**a**) plots the intensity $I(x, z) \propto |E_y(x, z; \theta)|^2$ for a single plane wave incident at angle θ. When there are multiple plane waves of different incident angles θ_i, the fields interfere and the intensity $I(x, z) \propto |\sum_i E_y(x, z; \theta_i)|^2$ becomes localized around the point of incidence, as depicted in Figures 2.3 (**b**-**d**). In general, the transverse profile at $z = 0$ of any field can be decomposed as a weighted sum over all possible (transverse) plane waves with incident wave vectors $(k_x, k_y)^{\mathrm{T}}$ and with $k_z = \sqrt{\omega^2/c^2 - (k_x^2 + k_y^2)}$. However, $\mathbf{k}$ for beam-like solutions will be dominated by the k_z component leading to the first-order binomial expansion, known as the *paraxial approximation*

$$k_z \approx k^2 \left(1 - \frac{k_x^2 + k_y^2}{2k^2}\right) . \tag{2.29}$$

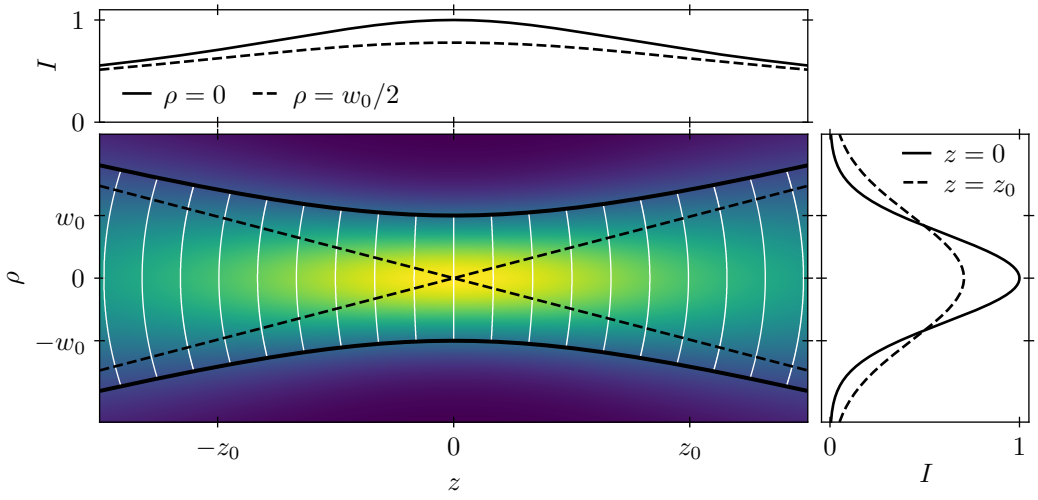

Figure 2.4: The intensity of a Gaussian beam ($E_0 = w_0 = \lambda = 1$) is depicted with low intensity as purple and high intensity as yellow. The waist profile is drawn in solid black. White contours mark where the electric field has a constant phase. Black dashed lines depict the divergence angle. Axial and radial line cuts of the intensity profile are shown above and right of the intensity map, respectively.

A *Gaussian beam* is an approximately-paraxial solution for localized light that accurately describes laser beams. The electric field of a Gaussian beam is [39]

$$\mathbf{E}(x,y,z,t) = \mathbf{E}_0 \frac{w_0}{w(z)} e^{-(x^2+y^2)/w^2(z)} \exp\left[ikz - i\eta(z) + ik\frac{\rho^2}{2R(z)} - i\omega t\right], \tag{2.30}$$

$$w(z) = w_0\sqrt{1+\frac{z^2}{z_0^2}}, \quad R(z) = z + \frac{z_0^2}{z}, \quad \eta(z) = \arctan\frac{z}{z_0}, \tag{2.31}$$

where $z_0 = \pi w_0^2/\lambda$ is the *Rayleigh range* and w_0 is the *beam waist*. For z within the Rayleigh range the beam is well localized according to $w(|z| \leq z_0) \leq \sqrt{2}w_0$. Beyond the Rayleigh range, the beam diverges linearly at an angle $\theta = \lambda/\pi w_0$

with respect to the z-axis. Importantly, the Gaussian beam model describes how all laser beams have a minimum waist somewhere along their beam path beyond which the beam diverges; there is no such thing as an infinitely-parallel beam of light.

In a medium of refractive index n, the intensity $I(\mathbf{r}) = n\epsilon_0 c|\mathbf{E}(\mathbf{r})|^2/2$ of a beam may be conveniently written in terms of its optical power $P = \pi w_0^2 n\epsilon_0 c|E_0|^2/4$ as

$$I(x, y, z) = \frac{2P}{\pi w^2(z)} e^{-2(x^2+y^2)/w^2(z)} \,. \tag{2.32}$$

Figure 2.4 depicts the intensity and phase of a Gaussian beam.

When a thin lens of focal length f is placed at the waist of a Gaussian beam, a new waist w_0' is formed a distance d beyond the lens where

$$d = \frac{f}{1 + f^2/z_0^2} \,, \tag{2.33}$$

$$w_0' = \frac{\lambda f}{\pi w_0} \frac{1}{\sqrt{1 + f^2/z_0^2}} \,. \tag{2.34}$$

The implication of Equation (2.34) is that a Gaussian beam may be very tightly focused. For practical reasons, the ratio f/w_0 cannot be made much smaller than 1 because large w_0 demands a large diameter lens and small f demands a thick lens. Hence, in the best case, $w_0' \sim \lambda$. Moreover, the paraxial approximation that underpins the Gaussian beam solution breaks down for tightly focused beams anyway: Even when $\lambda/2\pi w_0 = 0.1$, the paraxial approximation incurs an average error of about 4% in the electromagnetic field components; fifth-order corrections reduce the average error to less than

0.1% [40]. Nonetheless, the analytic tractability of the Gaussian beam solution makes it a useful modeling tool, as we shall see in the following section.

2.1.3 Optical forces in the Rayleigh regime

When light impinges an object that is much smaller than the light's wavelength, the incident electric field is approximately constant over and inside the object. In this *Rayleigh regime* the electric field polarizes the object such that it may be considered a point dipole. In this section, we will develop the optical forces on a sphere near the focus of a Gaussian laser beam in the dipole approximation.

Consider a harmonic wave of the electromagnetic field $\{\mathbf{E}(\mathbf{r})e^{-i\omega t}$, $\mathbf{H}(\mathbf{r})e^{-i\omega t}\}$ wave with vacuum wavenumber $k = 2\pi/\lambda = \omega/c$ propagating in a medium of refractive index n_m towards a small sphere of index n and radius R. Assume that the medium and particle are both non-magnetic and non-conducting so that $\mu, \mu_\mathrm{m} \approx \mu_0$ and $\epsilon/\epsilon_\mathrm{m} \approx n^2/n_\mathrm{m}^2 = m_\mathrm{r}^2$. The parameters with no subscript refer to the particle, the parameters with the m subscript refer to the medium, and the relative refractive index is defined as $m_\mathrm{r} = n/n_\mathrm{m}$.

The dipole approximation holds if $n_\mathrm{m}kR \ll 1$ and $nkR \ll 1$. In the dipole approximation, the sphere's polarization is treated as a point dipole moment $\mathbf{p}(\mathbf{r}, t) = \alpha\mathbf{E}(\mathbf{r}, t)$. The *complex polarizability*

$$\alpha = \alpha_0 \left(1 - i\frac{n_\mathrm{m}k^3\alpha_0}{6\pi\epsilon_0}\right)^{-1}, \tag{2.35}$$

$$\alpha_0 = 4\pi n_\mathrm{m}^2 \epsilon_0 R^3 \left(\frac{m_\mathrm{r}^2 - 1}{m_\mathrm{r}^2 + 2}\right), \tag{2.36}$$

includes polarization effects of the scattered field near the sphere surface [41].

The total amount of optical power diverted by the sphere, per unit incident power-per-area, is the *extinction cross section* σ_{ext}. The extinction of light is split into two parts, absorption and scattering: $\sigma_{\text{ext}} = \sigma_{\text{abs}} + \sigma_{\text{sc}}$. In the case of non-conducting spheres $\sigma_{\text{abs}} = 0$. The optical theorem links the cross-section to the complex polarizability

$$\sigma_{\text{ext}} = \frac{k}{n_{\text{m}}}\text{Im}[\alpha] \tag{2.37}$$

$$= \frac{\frac{8}{3}\pi R^2 (n_{\text{m}} kR)^3 (m_{\text{r}}^2 - 1)^2/(m_{\text{r}}^2 + 2)^2}{1 + \frac{4}{9}(n_{\text{m}} kR)^6 (m_{\text{r}}^2 - 1)^2/(m_{\text{r}}^2 + 2)^2} \tag{2.38}$$

$$\approx \frac{128\pi^5 n_{\text{m}}^4 R^6}{3\lambda^4}\left(\frac{m_{\text{r}}^2 - 1}{m_{\text{r}}^2 + 2}\right)^2 . \tag{2.39}$$

The last line makes use of the condition $(n_{\text{m}} kR) \ll 1$ to simplify the denominator. At the same level of approximation, note that $\text{Re}[\alpha] \approx \alpha_0$.

The time-averaged force on a dipole is given by the Lorentz Force law [42]. For non-magnetic and non-relativistic dipoles, the force is [43, 44]

$$\langle F \rangle = \frac{1}{2}\text{Re}\left[\alpha \sum_{i \in \{x,y,z\}} E_i \nabla E_i^*\right] \tag{2.40}$$

$$= \frac{1}{2c\epsilon_0 n_{\text{m}}}\text{Re}\left[\alpha\right] \nabla I(\mathbf{r}) + \frac{n_{\text{m}}}{c}\sigma_{\text{ext}}\langle \mathbf{S} \rangle - \frac{1}{2}\frac{c}{n_{\text{m}}}\sigma_{\text{ext}} \nabla \times \langle \mathbf{s} \rangle , \tag{2.41}$$

where $I(\mathbf{r}) = \frac{1}{2} n_{\text{m}} c |\mathbf{E}(\mathbf{r})|^2$ is the intensity of the wave, $\langle \mathbf{S} \rangle = \frac{1}{2}\text{Re}[\mathbf{E} \times \mathbf{H}^*]$ is the time-averaged Poynting vector and $\langle \mathbf{s} \rangle = i\frac{n_{\text{m}}^2}{2\omega}\epsilon_0(\mathbf{E} \times \mathbf{E}^*)$ is the time-averaged *spin angular momentum density*. Equation (2.40) is computationally convenient because it only requires knowledge of the electric field. Equation (2.41)

is conceptually useful because each term has a physical interpretation. The first term is the *gradient force*. It is conservative. When $\mathrm{Re}[\alpha] > 0$ — or equivalently $n > n_\mathrm{m}$ — the gradient force points towards the wave's intensity maximum and is responsible for optical trapping. The second term is the *scattering force*. It is non-conservative, points in the direction of the wave's energy flow, and must be overcome for stable optical trapping. The third term is the *spin curl force* [45]. It is a non-conservative scattering force and is typically zero or small compared to the other terms[2]. The spin curl force can become significant in the presence of polarization gradients.

Let us now specialize the force calculation to a Gaussian beam propagating along the z-axis. Take the beam waist as the origin of the coordinate system so the incident electric field $\mathbf{E}(\mathbf{r}, t)$ is given by Equation (2.30). For this configuration $\langle \mathbf{S} \rangle = I(\mathbf{r})\hat{\mathbf{z}}$, $\langle \mathbf{s} \rangle = \mathbf{0}$, and the intensity $I(\mathbf{r})$ is given by Equation (2.32). The gradient force is $\mathbf{F}_\mathrm{grad} = \alpha_0 \nabla I/(2cn_\mathrm{m}\epsilon_0)$. Expressing ∇I in terms of I and w,

$$\begin{aligned}
F_{\mathrm{grad},\,x}(x,y,z) &= -x\frac{8\pi n_\mathrm{m} R^3}{c}\left(\frac{m_\mathrm{r}^2-1}{m_\mathrm{r}^2+2}\right)\frac{I(x,y,z)}{w^2(z)}\,,\\
F_{\mathrm{grad},\,y}(x,y,z) &= -y\frac{8\pi n_\mathrm{m} R^3}{c}\left(\frac{m_\mathrm{r}^2-1}{m_\mathrm{r}^2+2}\right)\frac{I(x,y,z)}{w^2(z)}\,,\\
F_{\mathrm{grad},\,z}(x,y,z) &= -z\frac{4\pi n_\mathrm{m} R^3}{c}\left(\frac{m_\mathrm{r}^2-1}{m_\mathrm{r}^2+2}\right)\frac{I(x,y,z)}{w^2(z)}\frac{w_0^2}{z_0^2}\left(1-\frac{2(x^2+y^2)}{w^2(z)}\right)\,.
\end{aligned} \tag{2.42}$$

[2]There is some controversy over the reality of the spin gradient force in the dipole approximation [46, 47]. In general, the understanding of momentum and angular momentum of light is quite subtle, especially in the presence of a medium [48, 49].

The scattering force is

$$\mathbf{F}_{\mathrm{sc}} = \frac{128\pi^5 n_{\mathrm{m}}^5 R^6}{3c\lambda^4}\left(\frac{m_{\mathrm{r}}^2 - 1}{m_{\mathrm{r}}^2 + 2}\right)^2 I(x, y, z)\hat{\mathbf{z}}\,. \tag{2.43}$$

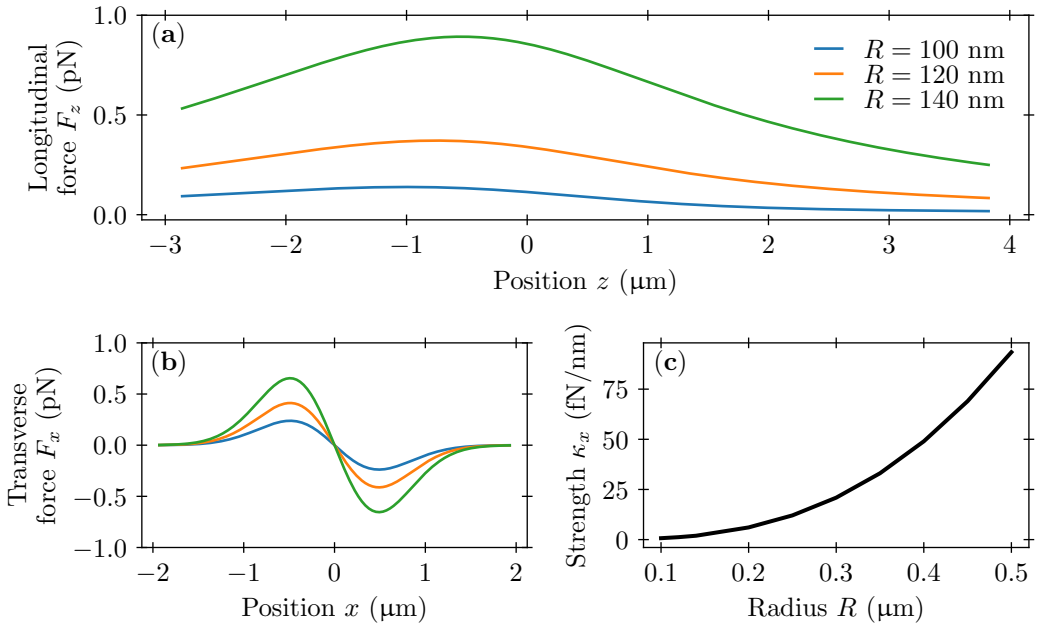

Figure 2.5: The (**a**) longitudinal ($x = 0$) and (**b**) transverse ($z = 0$) trapping forces are shown as a function of a sphere's position $(z, x)^{\mathrm{T}}$ and radius R. (**c**) The transverse trap strength κ_x, determined by linear fits near the trap center, is shown as a function of sphere radius. This calculation uses $P_0 = 50\,\mathrm{mW}$ of $\lambda = 1064\,\mathrm{nm}$ light focused to a waist of $w_0 = 1\,\mu\mathrm{m}$ (numeric aperture 0.33), $n_m = 1$, and $n = 1.47$.

.

For a specific example, consider a silica microsphere of radius R and a 1064 nm-wavelength paraxial Gaussian beam focused with a numeric aperture of 0.33. In Figure 2.5 (**a-b**) we show the longitudinal and transverse trapping forces, respectively, for various R. Figure 2.5 (**c**) shows the transverse trap strength as a function of R is monotonically increasing. Despite all relevant

parameters held constant, the ray optics and Rayleigh scattering calculations of the transverse trapping strength, show opposite trends. A more general approach is needed to bridge between the two regimes when $R \sim \lambda$.

2.1.4 Mie scattering

There exists a scattering regime in which neither the ray-optics picture nor the Rayleigh approximation accurately describes the optical forces of a focused laser beam on a microsphere. In this *Mie scattering*[3] regime, the scattering object is roughly the same size as the wavelength of impinging light. For the case of a dielectric spherical scatterer and an incoming plane wave, the solution has been known for more than a century [50–52]. More generally, the optical force caused by an electromagnetic field may be found by the integral of the total field's time-averaged momentum density over any surface enclosing the scatterer [53]. Calculating the optical forces in this regime is significantly more involved than the two regimes considered previously.

Fortunately, mature and open-source numerical packages have been written to solve the problem quite generally [54]. The package we use is called the Optical Tweezers Toolbox [55]. The Optical Tweezer Toolbox uses the *point-matching T-matrix method* [56]. In this method, the incoming and outgoing fields are expanded in terms of vectorial basis functions. The expansion coefficients of the incoming beam are found by point-matching the field across

[3]While Mie is often the only early name associated with exact electromagnetic scattering solutions, both Clebsch [50] and Lorenz [51] solved the same problem earlier than Mie.

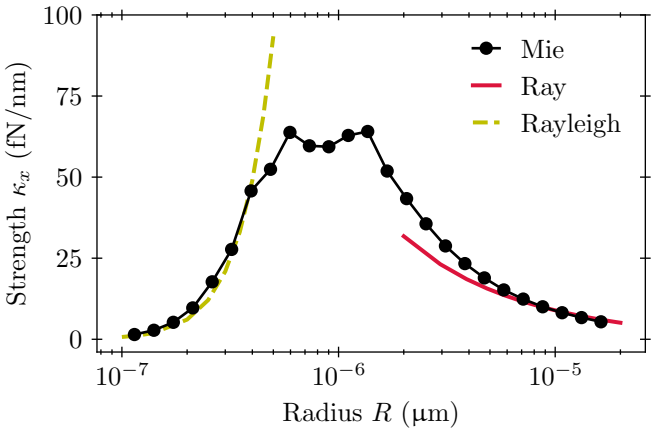

Figure 2.6: Comparing the transverse trap strength found through calculations based on Rayleigh scattering, ray optics, and Mie scattering. All relevant parameters are held constant across the three calculations. For radii near the trapping wavelength $\lambda = 1064\,\text{nm}$, only Mie scattering gives reliable results.

the scatterer's boundary, providing a much more accurate description of a focused beam than the paraxial approximation. The outgoing beam's expansion coefficients are linearly related to those of the incoming beam through the T-matrix. The T-matrix encodes the scatterer's material properties and geometry.

In Figure 2.6 we show the transverse trap strength κ_x for $\lambda = 1064\,\text{nm}$ light focused to a waist of $1\,\mu\text{m}$ as a function of radius R. The Mie scattering result interpolates between the Rayleigh scattering and ray optics regimes. The quantitative agreement between the advanced Mie scattering software and our custom ray optics code in the large-R limit provides some validation for our implementation. Similar conclusions hold for our custom Rayleigh scatting code in the small-R limit.

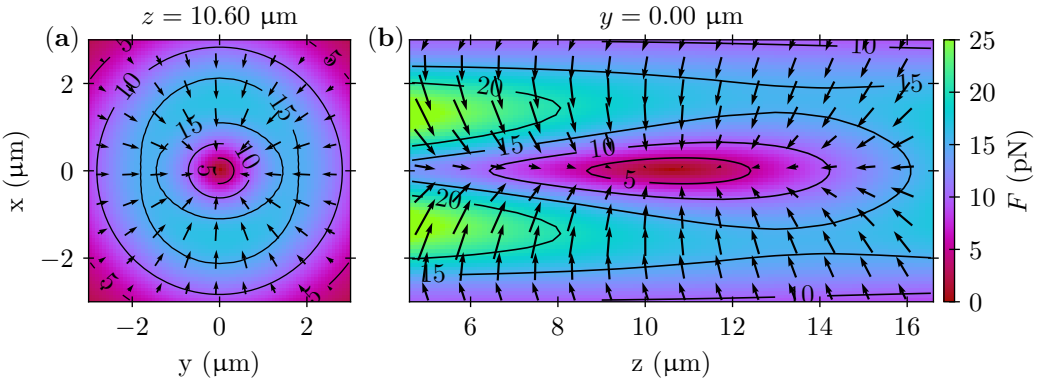

Figure 2.7: Two-dimensional projections of the optical forces exerted by a counter-propagating, dual-beam optical trap (beam 1: $w_0 = 2\,\mu\text{m}$, $P_0 = 56\,\text{mW}$, beam 2: $w_0 = 3\,\mu\text{m}$, $P_0 = 70\,\text{mW}$, offset longitudinally by $25\,\mu\text{m}$) on a radius $R = 1.51\,\mu\text{m}$ silica microsphere. (**a**) shows the transverse plane at the longitudinal minimum. (**b**) shows one of the longitudinal planes.

Due to the generality of the T-matrix method and its implementation in the Optical Tweezers Toolbox, we can make a model of our counter-propagating dual-beam optical trap. In Figure 2.7 we show two-dimensional projections of the optical trapping forces modeling our experimental trap. One beam is traveling along the positive z-axis and focused to a waist of $2\,\mu\text{m}$ at the origin. The second beam is traveling along the negative z-axis and focused to a waist of $3\,\mu\text{m}$ and offset in the z-direction by $25\,\mu\text{m}$ from the origin. The scattering forces from the two beams cancel at the trap center leading to a stable trap in all three dimensions. In Figure 2.8 we show the one-dimensional line cuts of the trapping force. Clear positive-to-negative zero crossings in all three dimensions indicate a stable trap. Fits near the trap center reveal $\kappa_x = 17\,\text{fN/nm}$, $\kappa_y = 15\,\text{fN/nm}$, and $\kappa_z = 3\,\text{fN/nm}$.

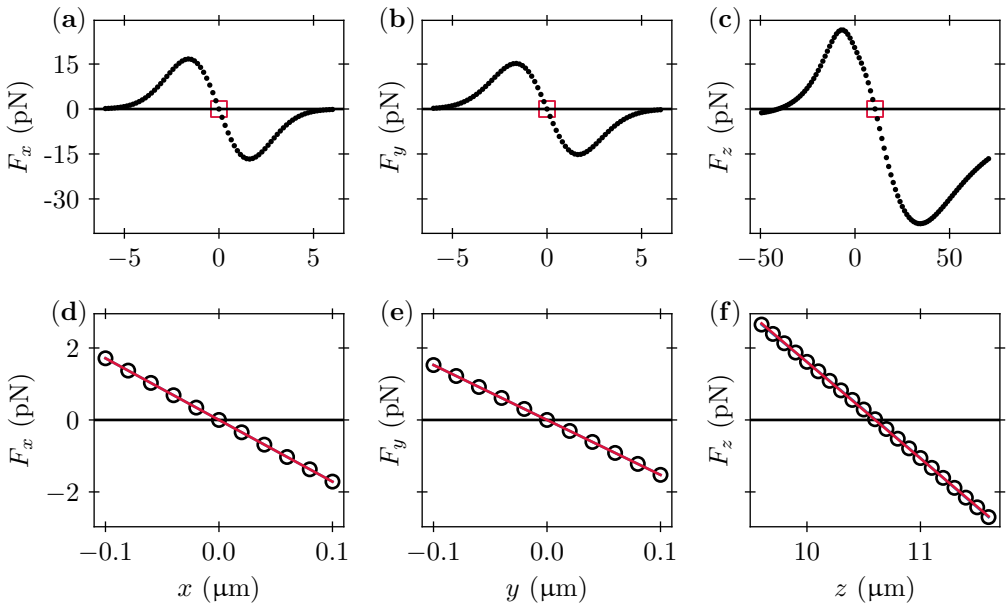

Figure 2.8: One-dimensional line-cuts of force components. (**a-c**) Line cuts of the data are shown in Figure 2.7. (**d-f**) A zoom of the region near the trap center [red squares in (**a-c**)]. Solid lines are linear fits and open circles are data calculated with the Optical Tweezers Toolbox.

Through the last three subsections, we have considered the optical trapping of microspheres in three size regimes. The ray optics picture is accurate for large microspheres and provides intuition on how optical trapping works. The Rayleigh limit is accurate for small microspheres and has the benefit of computational simplicity. The most general approach discussed here, the point-matching T-matrix method, is valid for any microsphere size. However, quantitative modeling is challenged by the sensitivity of optical forces to input parameters. Small changes in beam alignment or waist size can significantly alter the calculation results. Such sensitivity is a fact of nature and therefore underscores the technical challenges of aligning a dual-beam optical trap in practice. The alignment will be discussed in detail in Chapter 3, but first, we switch our focus to signal analysis.

2.2 Signal analysis

The labor of physics is largely divided into 1) devising physical theories that make testable predictions and 2) testing those predictions against empirical experiments. Experimental tests require the measurement of a physical quantity present in the theory. Often one finds quantities that are easy to measure and relates them to quantities of interest. For example, the weight of an object may be measured by placing a calibrated spring between the object and the Earth and measuring, with e.g. a ruler, the compression of the spring. Another example is the measurement of eclectic current. The current-to-be-measured is diverted into a wire coiled around a compass needle (such that the

needle can still spin within the coil). In the absence of current, the device is aligned with Earth's magnetic field such that the compass needle points perpendicular to the coil axis. The presence of a current generates an additional magnetic field, orthogonal to the needle's rest position, and therefore redirects the needle by a measurable angle that is proportional to the current.

The above two examples were specifically considered because they transform gravitational or magnetic forces into measurable displacements. However, it is much more common to measure electric potential differences, or *voltages*. A primary reason for this is that voltages may be easily measured digitally using analog-to-digital conversion (or *digitization*). A digitized voltage is a binary representation of the magnitude of the voltage. The resolution of the digital representation is set by the number of bits used in the conversion. For example, optical power incident on a photodiode generates a proportional current. The current is diverted through a known resistor and the voltage across the resistor may be amplified, digitized, and stored in a computer. Later, the data may be processed to convert from bits to voltage to current to optical power. Typically, the conversion from bits to voltage is done internally by the converter. Furthermore, every measurement has an associated uncertainty. The *statistical uncertainty* represents the fluctuations in an ensemble of identically-prepared measurements and thus quantifies *precision*. The *systematic uncertainty* quantifies the measurement's *accuracy* and contains both the bias due to uncertain conversions and the fundamental *resolution* of the detection system (including the sensor, amplifier, and digitizer).

Consider a process in which a physical quantity changes value. The process may be *deterministic*, meaning that a corresponding theory predicts the exact value of the changing quantity, or *stochastic*, meaning that the theory predicts the probability distribution of the changing quantity. Regardless of whether the underlying process is deterministic or stochastic, a *signal* (or a sequence of measurements) will invariably fluctuate. That is to say, if the process is flipping a fair coin, then the theory predicts an equal probability of heads and tails. The signal generated by N coin flips (a record of the outcomes) may approximate the probabilities of the underlying process using statistics of the signal. It is very unlikely to find exactly $N/2$ heads in a given signal, but the statistics approach the probabilities as N increases. In practice, a signal is often derived from an analog-to-digital converter that is used to record digitized voltages at uniformly-spaced, discrete times.

Stochastic processes, as opposed to deterministic ones, are often of interest, especially in the micro- and nano-scales where thermal or quantum fluctuations are themselves the process under study. Probability distributions are defined by their statistical properties, like their mean and covariance. A process is *stationary* if its governing distribution is independent of time. For example, imagine measuring the weight of an object 100 times in a day. Suppose the measurement outcomes are distributed as a Gaussian, defined by a mean and variance. Then repeat the experiment every few years and otherwise leave the object undisturbed. If one finds that the distribution of measurements is characterized by the same mean and variance each year (within the

measurement's uncertainty) then one may conclude the process (the state of the object between measurements, e.g. sitting at rest) is stationary. However, stationarity depends on the scope of the measurement. The above type of experiment has indeed been performed on the object formerly defined as the kilogram in the SI unit system. However, it was found that the mean mass (weight divided by the local gravitational field) was slowly decreasing [57]. Obviously, the definition of a unit should be a stationary variable. Recently, the kilogram was re-defined in terms of fundamental constants of nature [58]. These constants are believed to be stationary, though experiments seeking variations in such fundamental constants are ongoing [59].

In the remainder of this Section, we deal with the analysis of fluctuating signals derived from stochastic processes. The tools defined herein are quite subtle mathematically and we will largely ignore these subtleties. Instead, we focus on standard results and intuition-building calculations that are instructive for interpreting experimental data.

2.2.1 Basic statistics and time-domain quantities

When a signal $x(t)$ is recorded from a stationary and stochastic process, examining it directly is not particularly informative. We are interested in analysis techniques that elucidate the underlying process x. For this purpose, we will define basic statistics as well as the autocorrelation function, power spectral density, and mean-squared-increment.

The probability that $x(t)$ is between the values q and $q + \mathrm{d}q$ is $\mathcal{P}_x(q)\mathrm{d}q$

where $\mathcal{P}_x$ is the *probability density* for realizations $x(t)$ from the process x. The *ensemble average* or *expected value* is

$$\langle x(t) \rangle = \int_{-\infty}^{\infty} \mathrm{d}q \, q \mathcal{P}_x(q) \, . \tag{2.44}$$

For a large number M of realizations $x^{(i)}(t)$, $i = 0, 1, \ldots M-1$, one can estimate the expected value as the sample average

$$\langle x(t) \rangle = \frac{1}{M} \sum_{i=0}^{M-1} x^{(i)}(t) \, . \tag{2.45}$$

Similarly, the *sample variance* [4] is

$$\left\langle [x(t) - \langle x(t) \rangle]^2 \right\rangle = \frac{1}{M} \sum_{i=0}^{M-1} \left[x^{(i)}(t) - \langle x(t) \rangle \right]^2 \, . \tag{2.46}$$

Unless mentioned otherwise, we will assume $\langle x(t) \rangle = 0$ so the ensemble variance is equal to the second moment

$$\langle x^2(t) \rangle = \frac{1}{M} \sum_{i=0}^{M-1} \left[x^{(i)}(t) \right]^2 \, . \tag{2.47}$$

Stationary implies that, for all t, $\langle x(t) \rangle = \mu_x$, $\langle x^2(t) \rangle = \sigma_x^2$, and similar for all higher order statistics. Hence, for example, $\langle x^2(t) \rangle = \langle x^2(0) \rangle$.

In general, the ensemble average is distinct from the *time-average* $\overline{x(t)}$. For a long measurement time T_m, the time average may be approximated by the function mean

$$\overline{x(t)} = \frac{1}{T_\mathrm{m}} \int_0^{T_\mathrm{m}} \mathrm{d}t \, x(t) \, . \tag{2.48}$$

[4] With divisor M, the sample variance gives the maximum likelihood variance if x is Gaussian distributed. With divisor $M-1$ the sample variance gives an unbiased estimate of the $M \to \infty$ population variance.

When the time average equals the ensemble average we may refer simply to the mean and variance of the process

$$\langle x(t)\rangle = \overline{x(t)} = \mu_x\,, \quad \langle x^2(t)\rangle = \overline{x^2(t)} = \sigma_x^2\,. \tag{2.49}$$

When all statistics have equal ensemble and time averages, a stationary process is called *ergodic*. Suppose we have collected a digital signal $x = x(t) \to x = \{x_j\}$ where $x_j = x(t_j)$ is the j^{th} measurement collected at time $t_j = j\delta t$. The *sample rate* is $f_{\text{s}} = 1/\delta t$. Having N samples of the signal corresponds to a measurement window of $t \in [0, T_{\text{m}}]$ where $T_{\text{m}} = (N-1)\delta t \approx N\delta t$. The time average of a digital signal is

$$\overline{x(t)} = \frac{1}{N}\sum_{j=0}^{N-1} x_j\,. \tag{2.50}$$

Sometimes the sampling interval δt is much smaller than any other time scale of interest. In these cases, it can be advantageous to low-pass-filter the signal to eliminate excessive statistical fluctuations in x that do not reflect the dynamics of the underlying process. This type of filtering may be done by defining a new signal as the *block average* over non-overlapping length-τ segments of the old signal. The j^{th} element of the new signal corresponds to the (left-aligned) time $j\tau$ and is calculated as

$$\overline{x(\tau_{:j})} = \frac{1}{\tau}\int_{j\tau}^{(j+1)\tau} \mathrm{d}t\, x(t) \quad j = 0, 1, \ldots T_{\text{m}}/\tau - 1\,, \tag{2.51}$$

Where the notation $\tau_{:j}$ is introduced for the time interval $t \in [j\tau, (j+1)\tau]$. For a digital signal with $\tau = n\delta t$

$$\overline{x(\tau_{:j})} = \frac{1}{n}\sum_{i=0}^{n-1} x_{jn+i} \quad j = 0, 1, \ldots N/n - 1\,. \tag{2.52}$$

The *time derivative* of a signal is

$$\dot{x}(t) = \frac{\mathrm{d}x(t)}{\mathrm{dt}}\,. \tag{2.53}$$

For a digital signal, one may estimate the derivative using finite differences. For example

$$\begin{aligned} \dot{x}(t) &= \frac{x_{j+1} - x_{j-1}}{2\delta t} + \mathcal{O}(\delta t^2)\,, && (2.54)\\ &= \frac{1}{\delta t}\left(\frac{x_{j-4}}{280} - \frac{4x_{j-3}}{105} + \frac{x_{j-2}}{5} - \frac{4x_{j-1}}{5} + \right. \\ &\qquad \left. \frac{4x_{j+1}}{5} - \frac{x_{j+2}}{5} + \frac{4x_{j+3}}{105} - \frac{x_{j+4}}{280}\right) + \mathcal{O}(\delta t^8)\,. && (2.55) \end{aligned}$$

In Equation (2.54) $j = 1, 2, \ldots, N-2$ while in Equation (2.55) $j = 4, 2, \ldots, N-5$.

A signal's variance may be generalized to the ensemble average of the product of two possibly unequal-time measurements. This *autocorrelation function* or *autocovariance* is

$$C_{xx}(t, t') = \langle x(t)x(t')\rangle = C_{xx}(\tau) = \langle x(\tau)x(0)\rangle\,, \tag{2.56}$$

where the second equality uses the stationary property and defines the *lag time* $\tau = t - t'$. For a zero-mean, ergodic, digital signal, the autocorrelation function at lag $\tau_k = k\delta t$ may be estimated by

$$C_{xx}(\tau_k) = \frac{1}{N-k}\sum_{j=0}^{N-k-1} x_j x_{j+k}\,. \tag{2.57}$$

In practice, one typically limits $\tau_k/T_\mathrm{m} \lesssim 0.05$ in Equation (2.57) so that statistical fluctuations are adequately suppressed. The autocorrelation function

answers the question: on average, how correlated are two values of x separated in time by τ? Intuitively, the magnitude of correlation decreases as τ increases because information about a particular event is lost as time passes. Often C_{xx} is found to scale as a decaying exponential with characteristic time scale τ_x.

The *mean-squared increment* (or *mean-squared displacement* when x is a position measurement) is defined as $\langle \Delta^2(\tau) \rangle = \langle [x(\tau) - x(0)]^2 \rangle$. For a stationary signal,

$$\langle \Delta^2(\tau) \rangle = \left\langle [x(\tau) - x(0)]^2 \right\rangle = 2 \left[\langle x^2(0) \rangle - \langle x(\tau) x(0) \rangle \right] . \tag{2.58}$$

If the signal is ergodic and digitized, one may estimate

$$\langle \Delta^2(\tau_k) \rangle = \left\langle [x_k - x_0]^2 \right\rangle = \frac{1}{N-k} \sum_{j=0}^{N-k-1} (x_{j+k} - x_j)^2 . \tag{2.59}$$

The mean-squared displacement measures how much the signal deviates from its starting value after a time τ.

The *Allan variance* (or *two-sample variance*) is defined as half the mean-squared difference between adjacent block averages of a signal as a function of block length [60, 61]

$$\mathcal{A}_x^2(\tau) = \frac{1}{A-1} \sum_{j=0}^{A-2} \frac{1}{2} \left[\overline{x(\tau_{:j+1})} - \overline{x(\tau_{:j})} \right]^2 . \tag{2.60}$$

where $A = N/n$ is the number of independent length $\tau = n\delta t$ blocks in the signal of length $T_\mathrm{m} = N\delta t$. The Allan variance is sensitive to drifts in the signal. For an ergodic process, the squared difference between adjacent bin averages should decrease as $\sim 1/\tau$ since ideally they only differ due to finite statistics,

which improve according to the standard error of the mean. In reality, slow processes, (e.g. drifts in environmental temperature) break stationarity at long time scales, and $\mathcal{A}_x^2(\tau)$ will no longer decrease as $\sim 1/\tau$.

2.2.2 Power spectral density

So far, we have considered analysis techniques based on time-domain data. For frequency-domain techniques, we must define the Fourier transform and its inverse[5]

$$\tilde{x}(\omega) = \int_{-\infty}^{\infty} \mathrm{d}t\, e^{i\omega t} x(t)\,, \tag{2.61}$$

$$x(t) = \int_{-\infty}^{\infty} \frac{\mathrm{d}\omega}{2\pi}\, e^{-i\omega t} \tilde{x}(\omega)\,. \tag{2.62}$$

Consider the quantity $\langle \tilde{x}(\omega)\tilde{x}(\omega')\rangle$. Substitute Equation (2.61) for $\tilde{x}$ to find

$$\langle \tilde{x}(\omega)\tilde{x}(\omega')\rangle = \int_{-\infty}^{\infty} \mathrm{d}t \int_{-\infty}^{\infty} \mathrm{d}t' e^{i\omega t} e^{i\omega' t'} C_{xx}(t-t')\,.$$

Change variables to $\tau = t - t'$ and $s = (t + t')/2$ from $t = s + \tau/2$ and $t' = s - \tau/2$. The Jacobian of the transformation $\partial(t,\, t')/\partial(\tau,\, s)$ has unit determinate, so now

$$\langle \tilde{x}(\omega)\tilde{x}(\omega')\rangle = \int_{-\infty}^{\infty} \mathrm{d}s\, e^{i(\omega+\omega')s} \int_{-\infty}^{\infty} \mathrm{d}\tau\, e^{i(\omega-\omega')\tau/2} C_{xx}(\tau) = 2\pi\delta(\omega+\omega')\, S_{xx}(\omega) \tag{2.63}$$

In writing Equation (2.63), we have used the Dirac-delta

$$\delta(q-q') = \int_{-\infty}^{\infty} \frac{\mathrm{d}k}{2\pi}\, e^{-i(q-q')k}\,, \tag{2.64}$$

[5]The existence of the Fourier transform and its inverse for a stochastic signal is not guaranteed, but we shall proceed without further hesitation.

and defined the *power spectral density* as the Fourier transform of the auto-correlation function (as well as the corresponding inverse transformation)

$$S_{xx}(\omega) = \int_{-\infty}^{\infty} \mathrm{d}\tau \, e^{i\omega\tau} C_{xx}(\tau) \,, \tag{2.65}$$

$$C_{xx}(\tau) = \int_{-\infty}^{\infty} \frac{\mathrm{d}\omega}{2\pi} e^{-i\omega\tau} S_{xx}(\omega) \,. \tag{2.66}$$

In practice, Equation (2.65) is not particularly useful for analysis. Instead, one truncates the Fourier transform at long (but finite) measurement time T_m

$$\tilde{x}_{T_\mathrm{m}}(\omega) = \frac{1}{\sqrt{T_\mathrm{m}}} \int_0^{T_\mathrm{m}} \mathrm{d}t \, x(t) e^{i\omega t} \,. \tag{2.67}$$

Then, the *periodogram* is defined as $\langle \tilde{x}_{T_\mathrm{m}}(\omega) \tilde{x}_{T_\mathrm{m}}(-\omega) \rangle$. Since $x(t)$ is real-valued, $\tilde{x}_{T_\mathrm{m}}(\omega)$ is complex and $(\tilde{x}_{T_\mathrm{m}}(\omega))^* = \tilde{x}_{T_\mathrm{m}}(-\omega)$. The periodogram is

$$\left\langle \left| \tilde{x}_{T_\mathrm{m}}(\omega) \right|^2 \right\rangle = \frac{1}{T_\mathrm{m}} \int_0^{T_\mathrm{m}} \mathrm{d}t \int_0^{T_\mathrm{m}} \mathrm{d}t' \, \langle x(t) x(t') \rangle e^{i\omega(t-t')} \,.$$

As done above, change variables to $\tau = t - t'$ and $s = (t + t')/2$ and assume x is stationary to write

$$\left\langle \left| \tilde{x}_{T_\mathrm{m}}(\omega) \right|^2 \right\rangle = \frac{1}{T_\mathrm{m}} \int_0^{T_\mathrm{m}} \mathrm{d}s \int_{-\alpha(s)}^{\alpha(s)} \mathrm{d}\tau \, C_{xx}(\tau) e^{i\omega\tau} \,,$$

where

$$\alpha(s) = \begin{cases} 2s & s \leq T_\mathrm{m}/2 \\ 2(T_\mathrm{m} - s) & s > T_\mathrm{m}/2 \end{cases} .$$

When T_m is long compared to the correlation time of the signal ($T_\mathrm{m} \gg \tau_x$), we may extend the τ integration limits $\alpha \to \infty$ and the periodogram estimates the power spectral density

$$\left\langle \left| \tilde{x}_{T_\mathrm{m}}(\omega) \right|^2 \right\rangle = S_{xx}(\omega) \,, \tag{2.68}$$

Since we have defined the power spectral density as the Fourier transform of the autocorrelation function, Equation (2.68) is a statement of the *Wiener-Khinchin theorem*.

When $x(t)$ is a digital signal $x = \{x_j\}$, one evaluates Equation (2.67) in terms of a *discrete Fourier transform*. The *fast Fourier transform* is an efficient algorithm implemented in many programming languages. For example, the implementations available in Python via the packages Scipy or Numpy calculate the quantity (assuming N is even)

$$\tilde{x}_k = \sum_{j=0}^{N-1} x_j e^{-2\pi i k j/N} \quad k = 0, 1, \ldots, N-1\,, \tag{2.69}$$

$$f_k = \begin{cases} \frac{k}{N\delta t} & 0 \leq k \leq N/2 \\ -\frac{k}{N\delta t} & N/2 < k \leq N-1 \end{cases}\,. \tag{2.70}$$

Identifying $t_j = \delta t j$, and $\omega_k = 2\pi f_k$ reveals

$$S_{xx}(f_k) = \frac{\delta t}{N} |\tilde{x}_k|^2\,. \tag{2.71}$$

Note that Equation (2.69) and Equation (2.61) differ in the sign convention chosen for the complex exponential. This is inconsequential for the real-valued power spectrum. Further practical aspects of computing power spectral densities will be given in Section 2.2.3. However, Equation(2.71) provides a useful interpretation of the power spectral density. $S_{xx}(f)$ describes how much of the signal's variance is contained in a component pure tone at frequency f, per unit frequency. Suppose x has units of V. Then $S_{xx}(f)$ has units of V^2/Hz. Since the voltage measurements must be made across some resistance Z, the

electric power in a signal is V^2/Z which explains the origin of the name power spectral density.

2.2.3 Relationships between statistical quantifiers

We shall now explore the variety of ways in which quantities defined above are interrelated. First, a signal's variance will be related to its autocorrelation function, mean-squared displacement, and power spectral density. Then, the relationship between the power spectra of linearly-dependent signals is considered.

We begin by discussing how variance is related to the various quantities discussed in the previous section. Equation (2.58) for the mean-squared displacement can be rewritten in terms of the autocorrelation function

$$\langle \Delta^2(\tau) \rangle = 2 \left[C_{xx}(0) - C_{xx}(\tau) \right] . \tag{2.72}$$

The autocorrelation function at zero lag is identically the signal's variance $C_{xx}(0) = \sigma_x^2$. Thus for a decaying autocorrelation function $C_{xx}(\tau) \sim e^{-\tau/\tau_x}$, the long-time limit of the mean-squared displacement is twice the variance

$$\lim_{\tau \to \infty} \langle \Delta^2(\tau) \rangle = 2\sigma_x^2 . \tag{2.73}$$

Parseval's theorem or *the Plancherel theorem* relates the time-domain variance of a signal to the integral of the power spectral density. For large T_m,

$$\sigma_x^2 = \frac{1}{T_\mathrm{m}} \int_0^{T_\mathrm{m}} \mathrm{d}t \, |x(t)|^2 = \int_{-\infty}^{\infty} \mathrm{d}f \, S_{xx}(2\pi f) = \frac{1}{2\pi} \int_{-\infty}^{\infty} \mathrm{d}\omega \, S_{xx}(\omega) . \tag{2.74}$$

Since $S_{xx}(-\omega) = S_{xx}(\omega)$, $S_{xx}(\omega)$ is often visualized as the *one-sided* power spectral density $2S_{xx}(\omega > 0)$[6]. For similar reasons, one may express the *band-limited variance* over frequencies $f_1 > 0$ to $f_2 > 0$ as

$$\sigma_x^2(f_1, f_2) = 2 \int_{f_1}^{f_2} \mathrm{d}f S_{xx}(2\pi f) \,. \tag{2.75}$$

Next, let us relate the power spectral densities of two processes. Specifically, consider two processes related by a linear time-invariant transformation. For example, suppose a system takes $x_i(t)$ as an input and gives $y_i(t)$ as an output. Linearity means that, for constants a and b, the input $ax_1 + bx_2$ gives the output $ay_1 + by_2$. Time-invariance means that an input $x_i(t - \tau)$ gives an output $y_i(t-\tau)$ for all τ. The input-output relationship is completely captured by the *impulse response* $h(t)$. The impulse response is the system's output in response to the input $\delta(t)$. Given $h(t)$, the output y is the convolution of the input x with the impulse response h

$$y(t) = \int_{-\infty}^{\infty} \mathrm{d}\tau \, x(\tau) h(t - \tau) \,. \tag{2.76}$$

In the frequency domain, convolutions become multiplication, so

$$\tilde{y}(\omega) = \tilde{x}(\omega)\tilde{h}(\omega) \,. \tag{2.77}$$

The quantity $\tilde{h}$ is given many names and symbols depending on the nature of the system. Examples include frequency response, linear-response function,

[6]unfortunately, one- and two-sided power spectral densities are given the same symbol in the literature. Typically two-sided versions are used for theory calculations and one-sided versions for comparison to experiments. We try to explicitly label spectra as one- or two-sided.

susceptibility, transfer function, sensitivity, filter, impedance, mobility, and admittance. It then follows that the power spectra of the two quantities are related by

$$S_{yy}(\omega) = |h(\omega)|^2 S_{xx}(\omega)\,. \tag{2.78}$$

When $y = \dot{x}$ one has the useful identity

$$S_{\dot{x}\dot{x}}(\omega) = \omega^2 S_{xx}(\omega)\,, \tag{2.79}$$

which follows from differentiation of Equation (2.61): $\tilde{\dot{x}}(\omega) = -i\omega\tilde{x}(\omega)$. For a discrete, length-N signal collected with a sampling interval δt, it is tempting to then write $\tilde{\dot{x}}_k = i2\pi f_k \tilde{x}_k$ (accounting for the difference in sign convention mentioned earlier). However, the result consistent with Equation (2.54) for the finite difference is in fact [62]

$$\tilde{\dot{x}}_k = i\frac{\sin\left(\frac{2\pi f_k \delta t}{N}\right)}{\delta t}\tilde{x}_k\,. \tag{2.80}$$

An additional consequence of Equation (2.79) is

$$C_{\dot{x}\dot{x}}(t) = \int_{-\infty}^{\infty} \frac{\mathrm{d}\omega}{2\pi} e^{-i\omega t}\omega^2 S_{xx}(\omega) = -\frac{\mathrm{d}^2}{\mathrm{d}t^2} C_{xx}(t)\,. \tag{2.81}$$

2.2.4 Calculating the power spectral density

Estimating the power spectral density from real discrete data requires further attention. For this purpose let us call $\hat{S}_{xx,k} = \hat{S}_{xx}(f_k)$ the *estimated*

one-sided power spectral density

$$\hat{S}_{xx}(f_k) = \frac{2\delta t}{W_N} \left| \sum_{j=0}^{N-1} w_j^{(N)} x_j e^{-2\pi i j k/N} \right|^2 , \tag{2.82}$$

$$f_k = \frac{k}{N\delta t} , \tag{2.83}$$

for $k = 0, 1, \ldots, N/2$. Here, we have generalized Equation (2.67) and Equation (2.71) to include an optional *window function* $w_j^{(N)}$ that scales the signal x_j, typically so that $x_0, x_{N-1} \approx 0$. A power correction factor

$$W_N = \sum_{j=0}^{N-1} \left| w_j^{(N)} \right|^2 . \tag{2.84}$$

accounts for the attenuation introduced by the window. For the *box-car* or *rectangular* window $w_j^{(N)} = 1$, Equation (2.83) recovers twice the value of Equation (2.71) (the factor of two accounts for the one-sidedness). We will also make use of the *Hamming* window

$$w_j^{(N)} = 0.54 - 0.46 \cos\left(\frac{2\pi j}{N-1}\right) . \tag{2.85}$$

Let us assume that $x(t)$ is linearly related to a stationary stochastic variable $\xi(t)$ whose realizations follow a Gaussian probability density

$$\mathcal{P}_\xi(q) = \frac{1}{\sqrt{2\pi}\sigma_\xi} e^{\frac{-q^2}{2\sigma_\xi^2}} , \tag{2.86}$$

with $\mu_\xi = 0$ and $C_{\xi\xi}(t) = \delta(t)$. Since ξ_j is Gaussian-distributed, $\tilde{\xi}_k = \tilde{\xi}_k' + i\tilde{\xi}_k''$ has real ($\tilde{\xi}_k'$) and imaginary ($\tilde{\xi}_k''$) parts distributed independently and identical to ξ_j. Then, $\hat{S}_{xx,k} \propto |\tilde{\xi}_k|^2$ is distributed as the modulus-squared of two

independent identical Gaussian variables. The joint distribution of real and imaginary parts is

$$\mathcal{P}_{\tilde{\xi}',\tilde{\xi}''}(q,p) = \frac{1}{2\pi\sigma_\xi^2} e^{\frac{-(q^2+p^2)}{2\sigma_\xi^2}} .$$

The probability that $|\tilde{\xi}_k|^2 = \tilde{\xi}_k'^2 + \tilde{\xi}_k''^2$ is less than z is given by the *cumulative distribution function*

$$F_{|\tilde{\xi}_k|^2}(z) = \int_{(q^2+p^2)<z} \mathrm{d}q\mathrm{d}p\, \mathcal{P}_{\xi',\xi''}(q,p) .$$

In polar coordinates $q = r\cos\phi$, $p = r\sin\phi$, $\mathrm{d}p\mathrm{d}q = r\mathrm{d}r\mathrm{d}\phi$,

$$F_{|\tilde{\xi}_j|^2}(z) = \int_0^{\sqrt{z}} \frac{r\,\mathrm{d}r}{\sigma_\xi^2} e^{\frac{-r^2}{2\sigma_\xi^2}} = 1 - e^{\frac{-z}{2\sigma^2}} .$$

The probability density is related to the cumulative distribution according to $\mathcal{P}(z) = \mathrm{d}F(z)/\mathrm{d}z$:

$$\mathcal{P}_{|\tilde{\xi}_j|^2}(z) = \frac{1}{2\sigma_\xi^2} e^{\frac{-z}{2\sigma_\xi^2}} . \tag{2.87}$$

The result Equation (2.87) says that if an ergodic signal x_j is Gaussian-distributed then a particular realization of its periodogram $\hat{S}_{xx,k}$ is *exponentially*-distributed. It follows from the properties of exponential distributions that $\mu^2_{\hat{S}_{xx,k}} = \sigma^2_{\hat{S}_{xx,k}} = 2\sigma_\xi^2$, meaning the periodogram estimate fluctuates dramatically from one realization to the next: $\sigma_{\hat{S}_{xx,k}}/\mu_{\hat{S}_{xx,k}} = 1$. Moreover, a good model for the power spectral density, parameterized by a vector of quantities $\boldsymbol{\theta}$, $S^{(\boldsymbol{\theta})}_{xx,k} = S_{xx}(2\pi f_k;\boldsymbol{\theta})$, should follow the true power spectral density process mean $S^{(\boldsymbol{\theta})}_{xx,k} = \mu_{\hat{S}_{xx,k}}$, and hence

$$\mathcal{P}_{\hat{S}_{xx,k}}(z) = \frac{1}{S^{(\boldsymbol{\theta})}_{xx,k}} e^{-z/S^{(\boldsymbol{\theta})}_{xx,k}} . \tag{2.88}$$

To suppress the fluctuations inherent in the periodogram, one often takes an ensemble average over independent periodograms. In practice, this may be done with *Bartlett's method* by splitting the signal $\{x_j,\ j = 0, 1, \ldots, N-1\}$ into n independent blocks $\{\{x_j^{(i)}, j = 0, 1, \ldots, N/n-1\},\ i = 0, 1, \ldots, n-1\}$, computing the periodogram of each block $\hat{S}_{xx,k}^{(i)} = \hat{S}_{x^{(i)}x^{(i)},k}$, then averaging the result:

$$\langle \hat{S}_{xx,k} \rangle = \frac{1}{n} \sum_{i=0}^{n-1} \hat{S}_{xx,k}^{(i)} \,, \tag{2.89}$$

$$f_k = \frac{kn}{N\delta t} \,, \quad k = 0, 1, \ldots, \frac{N}{2n} \,. \tag{2.90}$$

What is probability density of $\langle \hat{S}_{xx,k} \rangle$? It is clearly the probability density of the sum of n random variables $\frac{1}{n}\hat{S}_{xx,k,}^{(i)}$. By scaling Equation (2.88) we have

$$\mathcal{P}_{\frac{1}{n}\hat{S}_{xx,k}^{(i)}}(z) = \frac{n}{S_{xx,k}^{(\boldsymbol{\theta})}} e^{-nz/S_{xx,k}^{(\boldsymbol{\theta})}} \,.$$

The probability density of the sum of n independent and identically distributed random variables is the n^{th} convolution of the probability density with itself. The convolution of n exponential distributions may be calculated via induction and is called the *Erlong distribution*

$$\mathcal{P}_{\langle \hat{S}_{xx,k} \rangle}(z) = \frac{e^{-nz/S_{xx,k}^{(\boldsymbol{\theta})}}}{S_{xx,k}^{(\boldsymbol{\theta})}} \frac{n^n}{(n-1)!} \left(\frac{z}{S_{xx,k}^{(\boldsymbol{\theta})}} \right)^{n-1} \,. \tag{2.91}$$

Importantly, $\mu_{\langle \hat{S}_{xx,k} \rangle} = S_{xx,k}^{(\boldsymbol{\theta})}$ and $\sigma_{\langle \hat{S}_{xx,k} \rangle} = S_{xx,k}^{(\boldsymbol{\theta})}/\sqrt{n}$. We see that Bartlett's method suppresses fluctuations by a factor of $1/\sqrt{n}$. The cost of splitting the initial signal into smaller blocks is evident in Equation (2.90): the spectral resolution $f_{k+1} - f_k$ is reduced by a factor of n. For simplicity of notation,

we will drop the $\langle\cdot\rangle$, and a reference to $\hat{S}_{xx,k}$ is understood to be Erlong-distributed.

The final result of interest for this section pertains to curve fitting power spectral density estimations. Typical least-squares fitting algorithms assume Gaussian-distributed data. As we have shown, Bartlett's power spectral density estimation is Erlong-distributed. Since the distribution is known, one may employ *maximum likelihood fitting*. To fit the model $S_{xx}^{(\theta)}$, one may maximize the likelihood of a particular realization $z_k \in \{\hat{S}_{xx}\}$ given the model parameters $\boldsymbol{\theta}$

$$\mathcal{L}(\hat{S}_{xx};\boldsymbol{\theta}) = \prod_k \mathcal{P}_{\hat{S}_{xx,k}}(z_k)\,. \tag{2.92}$$

Maximizing Equation (2.92) is equivalent to minimizing its negative logarithm

$$\ell(\hat{S}_{xx};\boldsymbol{\theta}) = -\log\mathcal{L}(\hat{S}_{xx};\boldsymbol{\theta}) = n\sum_k\left(\log\left[S_{xx}(f_k;\boldsymbol{\theta})\right] + \frac{z_k}{S_{xx}(f_k;\boldsymbol{\theta})}\right) + C\,, \tag{2.93}$$

where $C = \sum_k[\log[(n-1)!] - n\log n - (n-1)\log z_k]$ is a constant with respect to the model parameters and thus inconsequential for the minimization.

2.3 Theory of Brownian motion

As discussed in Section 1.1.2, Brownian motion refers to the random and persistent motion of micro-scale objects coupled to a thermal environment. The environment is understood to affect the Brownian particle in two inexorably linked ways: 1) The fluid is comprised of molecules in random motion; collisions with an object impart a stochastic or fluctuating *thermal force*. 2)

Through its *viscosity*, the fluid diffusivity transports momentum from layers of higher velocity towards layers of lower velocity. Since the velocity of the particle and fluid match that at the particle's boundary, the particle experiences a velocity-dependent drag *drag force*. Therefore, the particle gains kinetic energy through collisions and losses it through viscous dissipation. In thermal equilibrium the gain and loss of energy are equal and hence fluctuations and dissipation must be related to one another. Building out this and related ideas occupies the remainder of this Chapter. In Section 2.3.1 the dynamics of Brownian motion are modeled by the Langevin equation assuming an uncorrelated thermal force. Section 2.3.2 considers the case when hydrodynamic effects of the fluid, like its inertia and memory, induce correlations in the thermal force. Such correlations are typically not relevant for optically trapped spheres in air, but their hydrodynamic origin becomes relevant for acoustic detection at high frequencies. Then, Section 2.3.3 considers Brownian motion subject to the effects of confinement imposed by an optical trap. Finally, Section 2.3.4 introduces basic concepts of acoustics from the hydrodynamic perspective.

2.3.1 Einstein-Ornstein-Uhlenbeck theory

The one-dimensional Langevin equation of motion for a spherical Brownian particle of radius R, density ρ, and mass $m = 4\pi\rho R^3/3$ coupled to a fluid with viscosity η at temperature T is

$$m\dot{v}(t) + \gamma_0 v(t) = g\xi(t)\,, \tag{2.94}$$

where $v(t) = \dot{x}(t)$ is the particle's velocity and $x(t)$ its position at time t. The thermal force $F_{\rm th}(t) = g\xi(t)$ is of strength g and $\xi(t)$ is *Gaussian white noise*: $\xi(t)$ is a stationary, stochastic variable defined by the probability density (2.86) with zero mean $\mu_\xi = \langle \xi(t) \rangle = 0$ and δ-correlation $C_{\xi\xi}(t) = \langle \xi(t)\xi(0) \rangle = \delta(t)$. The drag force is $F_{\rm d}(t) = -\gamma_0 v(t)$. If the fluid density $\rho_{\rm f}$ is not too high (in a gas as opposed to a liquid) then we may write $\gamma_0 = 6\pi\eta R$ for a small spherical particle. As discussed above, the dissipation strength γ_0 and fluctuation strength g must be related in thermal equilibrium. Analysis of Equation (2.94) in terms of the statistics defined in Section 2.2 produces the *Einstein-Ornstein-Ulenbeck theory* for a Brownian particle's mean-squared displacement [63].

The first step is to write Equation (2.94) in the frequency domain in terms of $\tilde{v}(\omega)$ and $\tilde{\xi}(\omega)$. Using Equation (2.62)

$$\int_{-\infty}^{\infty} {\rm d}t \, e^{i\omega t} \left[i\omega m \tilde{v}(\omega) + \gamma_0 \tilde{v}(\omega) - g\tilde{\xi}(\omega) \right] = 0 \, .$$

For the above equality to hold for all circular frequencies ω, the integrand must be zero. Hence

$$\tilde{v}(\omega) = g\tilde{\xi}(\omega) \frac{\gamma_0 + i\omega m}{\gamma_0^2 + m^2\omega^2} \, . \tag{2.95}$$

By approaching the problem in frequency space, we have implicitly asserted that averages over initial conditions are equivalent to ensemble averages over realizations. This need not be the case if $x(0)$ and $v(0)$ may be controlled either experimentally or through post-selection of data [64, 65]. In the current case where the initial conditions are taken as fluctuating, the *equipartition theorem*

associates an average energy of $k_{\rm B}T/2$ with each quadratic degree of freedom — $k_{\rm B} = 1.380\,649 \times 10^{-23}\,{\rm J/K}$ is (exactly) *Boltzmann's constant*. That means $m\langle v^2(0)\rangle/2 = k_{\rm B}T/2$, or equivalently $\sigma_v^2 = k_{\rm B}T/m$.

The Wiener-Khinchin theorem (2.68) gives the power spectral density of velocity as

$$S_{vv}(\omega) = \frac{g^2}{\gamma_0^2 + m^2\omega^2} S_{\xi\xi}(\omega)\,.$$

By definition (2.66) of the power spectral density and the assumption $C_{\xi\xi} = \delta(t)$, we find $S_{\xi\xi} = 1$ and

$$C_{vv}(t) = \int_{-\infty}^{\infty} \frac{{\rm d}\omega}{2\pi}\, e^{-i\omega t} S_{vv}(\omega) = \frac{g^2}{2\pi m^2} \int_{-\infty}^{\infty} \frac{{\rm d}\omega\, e^{-i\omega t}}{(\omega - i\gamma_0/m)(\omega + i\gamma_0/m)}\,.$$

To evaluate the integral by the residue theorem, extend ω to the complex plane and note the poles in the integrand at $\omega = \pm i\gamma_0/m$. When $t > 0$ take a contour integral around a semicircle in the lower half ω-plane so that the arc contribution is zero and the real-line contribution is equal to the residue of the lower pole. For $t > 0$ the contour is taken in the upper half-plane. Define the *momentum relaxation time* $\tau_{\rm p} = m/\gamma_0$ to write the net result

$$C_{vv}(t) = \frac{g^2}{2\gamma_0 m} e^{-|t|/\tau_{\rm p}} = \frac{k_{\rm B}T}{m} e^{-|t|/\tau_{\rm p}}\,. \tag{2.96}$$

Since $C_{vv}(0) = \sigma_v^2 = k_BT/m$ we have set $g = \sqrt{2k_{\rm B}T\gamma_0}$ in the second equality. This is a statement of the fluctuation-dissipation theorem because it relates the strength of the fluctuating force g to the strength of the damping force γ_0. Having set g, we have the (two-sided) velocity power spectral density

$$S_{vv}(\omega) = \frac{2k_{\rm B}T\gamma_0}{\gamma_0^2 + m^2\omega^2}\,. \tag{2.97}$$

According to Equation (2.81), $\ddot{C}_{xx} = -C_{vv}$. Integrating once,

$$\dot{C}_{xx}(t \geq 0) = \frac{-k_{\mathrm{B}}T}{m}\left(-\tau_{\mathrm{p}}e^{-t/\tau_{\mathrm{p}}} + A\right)]$$
$$\dot{C}_{xx}(t \leq 0) = \frac{-k_{\mathrm{B}}T}{m}\left(\tau_{\mathrm{p}}e^{t/\tau_{\mathrm{p}}} + A'\right) .$$

Since x is driven by a stationary process, $C_{xx}(t) = C_{xx}(-t)$ and hence $\dot{C}_{xx}(t) = -\dot{C}_{xx}(-t)$. Enforcing the odd parity of $\dot{C}_{xx}$ at $t = 0$ requires $A = -A' = -m/\gamma_0$. Integrating again gives

$$C_{xx}(t) = \frac{2k_{\mathrm{B}}T}{m}\left(B - \tau_{\mathrm{p}}|t| - \tau_{\mathrm{p}}^2 e^{-|t|/\tau_{\mathrm{p}}}\right) . \tag{2.98}$$

The Brownian particle is free to diffuse through all of space, so $\sigma_x^2 = C_{xx}(0)$ is not defined. That means we do not have a condition to fix B. However Equation (2.72) for the mean-squared displacement is independent of B:

$$\langle \Delta^2(t > 0) \rangle = \frac{2k_{\mathrm{B}}T}{\gamma_0}\left(t + \tau_{\mathrm{p}}e^{-t/\tau_{\mathrm{p}}} - \tau_{\mathrm{p}}\right) . \tag{2.99}$$

Equation (2.99) for the mean-squared displacements captures the qualitative features of Brownian motion discussed in Section 1.1.2. At short times the particle displaces from its original position at a constant velocity $\sigma_v = \sqrt{k_{\mathrm{B}}T/m}$. At long times the particle displaces diffusivity (proportional $\sqrt{t}$) with diffusion constant $D = k_{\mathrm{B}}T/\gamma$. These limits are apparent from the fact that $e^{-t/\tau_{\mathrm{p}}} \approx 1 - t/\tau_{\mathrm{p}} + t^2/2\tau_{\mathrm{p}}$ for $t \ll \tau_{\mathrm{p}}$ and $e^{-t/\tau_{\mathrm{p}}} \approx 0$ for $t \gg \tau_{\mathrm{p}}$. Explicitly,

$$\sqrt{\langle \Delta^2(t) \rangle} = \begin{cases} \sigma_v t & t \ll \tau_{\mathrm{p}} \\ \sqrt{2Dt} & t \gg \tau_{\mathrm{p}} \end{cases} . \tag{2.100}$$

The ballistic velocity of a Brownian particle immersed in air was first experimentally measured in [34].

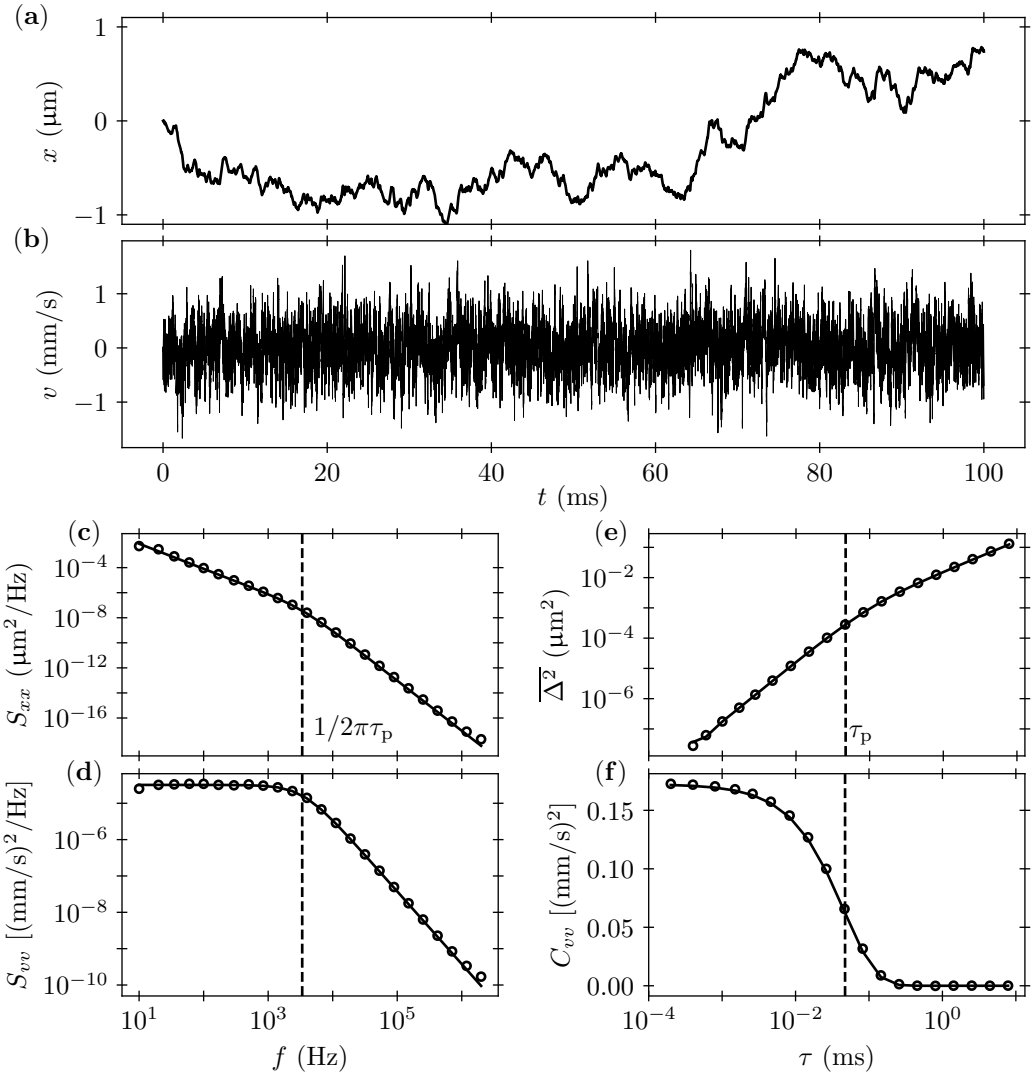

Figure 2.9: The dynamics of a free particle evolving under the Langevin equation of motion are simulated. (**a**) Position exhibits persistent random fluctuations and a slow diffusion away from the starting point. (**b**) Velocity fluctuates faster and has a well-defined variance. (**c**) The (one-sided) position power spectral density and (**d**) the velocity power spectral density are both shown on a log scale. (**e**) The mean-squared displacement and (**f**) the velocity autocorrelation function. In panels (**c** - **f**) the solid lines show the theoretical predictions while the open symbols are calculated from the discrete simulation data.

We have now established several theoretical results for statistical quantities calculated on the position and velocity of a Brownian particle whose motion is governed by the Langevin equation (2.94). This provides an opportunity to verify the discrete versions of the same quantities through simulation of the digitized dynamics x_j and v_j. To simulate a signal, we approximate the derivatives in Equation (2.94) as finite differences with a time step δt. The thermal force is $F_{\mathrm{th},j} = \xi_j \sqrt{2k_\mathrm{B}T\gamma/\delta_t}$ where ξ_j is a pseudo-random number drawn from a Gaussian distribution with zero mean and unit variance at each time step j. When $\dot{v} = \ddot{x}$ is approximated by a second order central-difference and $\dot{x}$ by a first-order forward difference then [66]

$$x_j = \frac{2 + \delta t/\tau_\mathrm{p}}{1 + \delta t/\tau_\mathrm{p}} x_{j-1} - \frac{1}{1 + \delta t/\tau_\mathrm{p}} x_{j-2} + \frac{\sqrt{2k_\mathrm{B}T\gamma}}{m\,(1 + \delta t/\tau_\mathrm{p})} \delta t^{3/2} \xi_j \,, \tag{2.101}$$

$$v_j = \frac{x_j - x_{j-1}}{\delta t} \,. \tag{2.102}$$

Given initial conditions x_0 and v_0, one may set $x_1 = x_0 + v_0\delta t$ and $x_2 = x_0 + 2v_0\delta t$. Higher-order finite difference schemes may be implemented for faster convergence with respect to the time step size δt.

In the simulations shown in Figure 2.9, a fourth-order Runge-Kutta integrator is used to solve for x_j and v_j simultaneously. We have set $R = 1.5\,\mu\mathrm{m}$, $\rho = 1700\,\mathrm{g/cm^3}$, $T = 300\,\mathrm{K}$, and $\eta = 18\,\mu\mathrm{Pa\,s}$, corresponding to a $3\,\mu\mathrm{m}$ diameter silica microsphere immersed in air at room temperature and in zero gravity. With these parameters $m = 2.4 \times 10^{-14}\,\mathrm{kg} = 24\,\mathrm{pg}$, $\tau_\mathrm{p} = 47\,\mu\mathrm{s}$, and $\sigma_v = 0.42\,\mathrm{mm/s}$. The simulation takes $N = 5 \times 10^5$ steps of size $\delta t = 200\,\mathrm{ns}$ for a total time of $T_\mathrm{r} = 100\,\mathrm{ms}$. The simulated position and velocity are

shown in Figure 2.9 (**a** - **b**). The power spectral density of position and velocity, mean-squared displacement, and velocity autocorrelation function, ensemble-averaged over 100 simulations, and are shown in Figure 2.9 (**c** - **f**). Each quantifier identifies τ_{p} as the only relevant time scale. The agreement between simulations and theory validates our numeric implementation of the quantifiers.

2.3.2 Hydrodynamic considerations

In Section 2.3.1 we derived various quantities of interest for the Langevin description of a Brownian particle. The whole process began by restricting to cases in which the hydrodynamic drag force on the particle could be expressed as $F_{\mathrm{d}}(t) = -\gamma_0 v(t)$. From there we transformed into frequency space and found Equation (2.95) relating $\tilde{v}(\omega)$ to $\tilde{F}_{\mathrm{th}}(\omega)$. Power spectral densities and autocorrelation functions for both position and velocity as well as the mean-squared displacement could then be calculated from Equation (2.95). To make this process more systematic note that Equation (2.95) is in the form of Equation (2.77). That is, $\tilde{v}(\omega) = \mathcal{Y}(\omega)\tilde{F}_{\mathrm{th}}(\omega)$ where we have defined the *admittance*

$$\mathcal{Y}(\omega) = (\gamma_0 - i\omega m)^{-1} \,. \tag{2.103}$$

The *Kubo-Green formula* links the admittance to the velocity autocorrelation function for an equilibrium system [67]

$$\mathcal{Y}(\omega) = \frac{1}{k_{\mathrm{B}}T} \int_0^\infty \mathrm{d}t \, e^{i\omega t} C_{vv}(t) \,. \tag{2.104}$$

The definition (2.65) of the power spectral density combined with stationarity $C_{vv}(-t) = C_{vv}(t)$ reveals

$$S_{vv}(\omega) = 2k_{\mathrm{B}}T\,\mathrm{Re}\left[\mathcal{Y}(\omega)\right] . \tag{2.105}$$

Hence through $S_{xx} = S_{vv}/\omega^2$ and the inverse formula (2.66) we find

$$C_{vv}(t) = \frac{k_{\mathrm{B}}T}{\pi}\int_{-\infty}^{\infty} \mathrm{d}\omega\, e^{-i\omega t}\,\mathrm{Re}[\mathcal{Y}(\omega)]\,, \tag{2.106}$$

$$C_{xx}(t) = \frac{k_{\mathrm{B}}T}{\pi}\int_{-\infty}^{\infty} \mathrm{d}\omega\, e^{-i\omega t}\,\frac{\mathrm{Re}[\mathcal{Y}(\omega)]}{\omega^2}\,. \tag{2.107}$$

The fluctuation-dissipation relation now follows from Equation (2.78) as

$$S_{F_{\mathrm{th}}F_{\mathrm{th}}}(\omega) = 2k_{\mathrm{B}}T\,\frac{\mathrm{Re}[\mathcal{Y}(\omega)]}{\left|\mathcal{Y}(\omega)\right|^2}\,. \tag{2.108}$$

As we will see in a specific example below, a wide class of hydrodynamic problems may be modeled by a complex, frequency-dependent damping coefficient $\gamma(\omega)$, resulting in the admittance $\mathcal{Y} = [\gamma(\omega) - im\omega]^{-1}$. The fluctuation-dissipation relation is then

$$S_{F_{\mathrm{th}}F_{\mathrm{th}}}(\omega) = 2k_{\mathrm{B}}T\mathrm{Re}[\gamma(\omega)]\,. \tag{2.109}$$

The recipe given in Equations (2.104) through (2.109) shows how one may calculate (at least numerically) the statistical quantities of interest for Brownian motion given the admittance of the system. The formula used in Section 2.3.1 for the drag force assumed a rarefied medium like a gas, but more generally the hydrodynamic force is the fluid stress integrated around the microsphere's boundary. The stress in a fluid is related to its velocity $\mathbf{u}(\mathbf{r}, t)$,

pressure $P(\mathbf{r},t)$, and density $\rho_{\rm f}(\mathbf{r},t)$ whose values are coupled through the *Navier-Stokes* equations. Realistic assumptions may be imposed to simplify the Navier-Stokes equations:

1. Linearization

$$\rho_{\rm f}(\mathbf{r},t) \to \rho_{\rm f} + \rho'_{\rm f}(\mathbf{r},t)\,, \quad P(\mathbf{r},t) \to P + P'(\mathbf{r},t)\,, \tag{2.110}$$

   where the primed quantities represent the small variation on the equilibrium (un-primed) quantities, and only terms linear in the primed quantities are maintained.

2. Small Reynolds number

$$\mathrm{Re} = \frac{\rho_{\rm f} u R}{\eta}\,, \tag{2.111}$$

   where the length scale is taken as the microsphere radius R and η is the fluid's dynamic viscosity. Small Re means that velocity advection is negligible thereby linearizing the fluid's velocity degree of freedom.

3. Incompressibility

$$\nabla \cdot \mathbf{u}(\mathbf{r},t) = 0\,, \tag{2.112}$$

   is valid for flows with velocity scale $u \ll c_0$ where c_0 is the speed of sound in the fluid.

4. A non-heat-conducting fluid implies entropy production is negligible (in the linear approximation) and hence the flow is isentropic (constant entropy s). Equivalently, the pressure varies only with the density and that

variation defines the speed of sound

$$c_0 = \sqrt{\left(\frac{\partial P}{\partial \rho_{\rm f}}\right)_s}\,. \tag{2.113}$$

From such assumptions, one may express the hydrodynamic drag force on a sphere moving with velocity $v(t)$ in a fluid otherwise at rest. When any bounding walls are far from the sphere and the fluid velocity is assumed to match the sphere velocity at the sphere's surface, the hydrodynamic drag force is [68]

$$F_{\rm d}[v(t)] = -\frac{1}{2}\delta m\dot{v}(t) - \gamma_0\left(v(t) + \sqrt{\frac{\tau_{\rm f}}{\pi}}\int_{-\infty}^{t} {\rm d}t'\,\frac{\dot{v}(t')}{\sqrt{t-t'}}\right)\,. \tag{2.114}$$

The *vorticity diffusion time*, defined as

$$\tau_{\rm f} = \frac{R^2\rho_{\rm f}}{\eta} = \frac{9}{2}\delta\tau_{\rm p}\,, \tag{2.115}$$

is the amount of time it takes for vorticity (the curl of velocity) to diffuse across the sphere. The density ratio is $\delta = \rho_f/\rho$. For a silica microsphere in air $\delta \sim 10^{-3} \ll 1$ hence $\tau_{\rm f} \ll \tau_{\rm p}$ and Equation (2.114) reduces to $F_{\rm d}[v(t)] \approx -\gamma_0 v(t)$. For silica in water $\tau_{\rm f} \sim \tau_{\rm p}$, so Equation (2.114) gives the correct hydrodynamic drag force, as long as the above four assumptions remain valid.

Furthermore, Equation (2.114) is given the following physical interpretation: The first term accounts for the added mass. That is, the acceleration of the sphere is impeded due to the inertia of the fluid made to follow the surface of the sphere as it moves. As a result, the dressed sphere mass $m^* = m(1+\delta/2)$ appears in the equipartition theorem: $\sigma_v^2 = k_{\rm B}T/m^*$. The added mass effect

is a consequence of incompressibility. At time scales shorter than $\tau_{c_0} = R/c_0$ compressibility of the flow matters and the added mass effect is expected to vanish, though this has yet to be experimentally verified. The second term is the usual viscous Stokes damping where $\gamma_0 = 6\pi\eta R$. The third term is called the *Basset history force*. The history force accounts for the fact that when the sphere accelerates it sets up flow fields in its vicinity. A moment later, those flow fields have diffused away slightly but the sphere still feels their influence through the fluid's viscosity. A moment after that, all the information about the initial acceleration event has diffused away. In this way, the fluid has a finite memory of the sphere's history and that memory has a back-action on the future dynamics of the sphere. Armed with Equation (2.114) we seek the corresponding admittance[7].

To find the admittance, express the general Langevin equation

$$m\dot{v}(t) - F_{\mathrm{d}}[v(t)] = F_{\mathrm{th}}(t)\,, \tag{2.116}$$

in the frequency domain by assuming a harmonic response $v(t) = v_0 e^{-i\omega t}$ and solving for v/F_{th}. The substitution $s = \sqrt{t - t'}$, $dt' = -2sds$ in the integral term of Equation (2.114) allows v to factor out of Equation (2.116) on the left-hand side, leading to

$$\mathcal{Y}(\omega) = \left[\gamma_0 \left(1 - 2i\omega\sqrt{\frac{\tau_{\mathrm{f}}}{\pi}} \int_0^\infty \mathrm{d}s\, e^{i\omega s^2}\right) - i\omega m(1 + \delta/2)\right]^{-1}.$$

[7]While we have started from Equation (2.114) and seek the admittance, the first-principles calculation starts from the Navier-Stokes equations, transforms to frequency space, identifies the admittance, and inverts to real space to end at Equation (2.114).

The remaining integral may be evaluated in the complex s-plane. Take a $1/8^{\text{th}}$-circle wedge contour with an angle of $45°$ with respect the Re[s]-axis. The contour encloses no poles and the arc section goes to zero by Jordan's lemma [8]. We deduce the integral of interest is identically minus the integral along the diagonal back to the origin. What remains is a Gaussian integral that may be evaluated by considering the integral-squared and changing to polar coordinates. To summarize,

$$\int_0^\infty \mathrm{d}s\, e^{i\omega s^2} = e^{i\pi/4} \int_0^\infty \mathrm{d}s\, e^{-\omega s^2} = \frac{1}{2}\sqrt{\frac{i\pi}{\omega}}\,.$$

Hence the admittance of a Brownian particle in a bulk, incompressible fluid is

$$\mathcal{Y}(\omega) = [\gamma(\omega) - i\omega m]^{-1} \tag{2.117}$$

$$= \frac{\left(1+\sqrt{\tau_{\mathrm{f}}\omega/2}\right) - i\left[\tau_{\mathrm{p}}\omega + \tau_{\mathrm{f}}\omega/9 + \sqrt{\tau_{\mathrm{f}}\omega/2}\right]}{\gamma_0\left(1+\sqrt{\tau_{\mathrm{f}}\omega/2}\right)^2 + \gamma_0\left[\tau_{\mathrm{p}}\omega + \tau_{\mathrm{f}}\omega/9 + \sqrt{\tau_{\mathrm{f}}\omega/2}\right]^2}\,, \tag{2.118}$$

where the frequency-dependent damping is, as given by Stokes [69]

$$\begin{aligned}\gamma(\omega) &= \gamma_0\left(1+\sqrt{-i\tau_{\mathrm{f}}\omega} - i\frac{\tau_{\mathrm{f}}\omega}{9}\right) \\ &= \gamma_0\left(1+\sqrt{\tau_{\mathrm{f}}\omega/2}\right) - i\gamma_0\sqrt{\tau_{\mathrm{f}}\omega/2}\left(1+\frac{2}{9}\sqrt{\tau_{\mathrm{f}}\omega/2}\right)\,,\end{aligned} \tag{2.119}$$

and $\sqrt{-i} = -i\sqrt{i} = (1-i)/\sqrt{2}$ defines the square-root branch cut. It is now straightforward to write the (two-sided) power spectral densities for velocity,

[8] Using the triangle inequality and the identity $4\theta \leq \pi\sin(2\theta)$ for $\theta \in [0, \pi/4]$, $\left|\int_{\mathrm{arc}} \mathrm{d}s\, e^{i\omega s^2}\right| < \int_{\mathrm{arc}} \mathrm{d}s\, \left|e^{i\omega s^2}\right| = R\int_0^{\pi/4} \mathrm{d}\theta\, e^{-\omega R^2\sin(2\theta)} \leq R\int_0^{\pi/4} \mathrm{d}\theta\, e^{-4\omega R^2\theta/\pi} = \pi\left(1-e^{-\omega R^2}\right)/4\omega R$, which goes to zero as $R\to\infty$.

position, and the thermal force

$$S_{vv}(\omega) = \frac{2k_{\mathrm{B}}T}{\gamma_0} \frac{1+\sqrt{\tau_{\mathrm{f}}\omega/2}}{\left(1+\sqrt{\tau_{\mathrm{f}}\omega/2}\right)^2 + \left[\tau_{\mathrm{p}}\omega + \tau_{\mathrm{f}}\omega/9 + \sqrt{\tau_{\mathrm{f}}\omega/2}\right]^2}\,, \tag{2.120}$$

$$S_{xx}(\omega) = \frac{S_{vv}(\omega)}{\omega^2}\,, \tag{2.121}$$

$$S_{F_{\mathrm{th}}F_{\mathrm{th}}}(\omega) = 2k_{\mathrm{B}}T\gamma_0\left(1+\sqrt{\tau_{\mathrm{f}}\omega/2}\right)\,. \tag{2.122}$$

Critically, we find frequency-dependent damping leads to a non-white thermal force spectrum. Equivalently, the fluctuating thermal force is correlated in time. However, in calculating the inverse transform Equation (2.66) to find $C_{F_{\mathrm{th}}F_{\mathrm{th}}}(t)$, confusion may arise due to 1) the presence of the square-root in $S_{F_{\mathrm{th}}F_{\mathrm{th}}}(\omega)$, 2) ensuring causality, and 3) properly accounting for initial conditions. Indeed, while much of the literature reports,

$$C_{F_{\mathrm{th}}F_{\mathrm{th}}}(t) = 2k_{\mathrm{B}}T\gamma_0\left(\delta(t) - \frac{1}{4}\sqrt{\frac{\tau_{\mathrm{f}}}{\pi}}t^{-3/2}\right),$$

the correct formula is claimed to be [70]

$$C_{F_{\mathrm{th}}F_{\mathrm{th}}}(t) = 2k_{\mathrm{B}}T\gamma_0\left[\delta(t) - \frac{1}{2}\sqrt{\frac{\tau_{\mathrm{f}}}{\pi t}}\left(\frac{1}{\tau_{\mathrm{p}}} + \frac{1}{2t}\right)\right], \tag{2.123}$$

which has a slower decaying term $\sim t^{-1/2}$ as compared to $\sim t^{-3/2}$. The $t^{-3/2}$ law is still correct for $t \lesssim \tau_{\mathrm{p}}$.

Formulae for the velocity autocorrelation function $C_{vv}(t)$ and the mean-squared displacement $\langle\Delta^2(t)\rangle$ may also be expressed analytically [71,72]. The full equations are not particularly informative but their limits are. At long times, $C_{vv}(t\to\infty) \propto \sigma_v^2 t^{-3/2}$, which is significantly slower than the exponential decay predicted by the Einstein-Ornstein-Uhlenbeck theory of Section

2.3.1. Historically, numeric studies on the motion of atoms in liquid argon gave the first indication of long-time tails in the velocity autocorrelation function [73]. Additional early theoretical work [74–76] recovered the asymptotic behavior from the perspective of hydrodynamics. As for the mean-squared displacement, the short- and long-time limits agree with the Einstein-Ornstein-Uhlenbeck Equation (2.100) but with $\sigma_v^2 = k_\mathrm{B}T/m^*$. The short-time motion of a Brownian particle in a liquid was first experimentally measured in [35].

The experiments reported on later in Chapter 4 were all performed in air, so the hydrodynamic effects discussed in this Section are negligible in equilibrium Brownian motion. However, in acoustic detection hydrodynamic corrections become relevant at frequencies above a few hundred kilohertz. The theory underlying acoustic detection will be discussed in Section 2.3.4, but first, we revise the theory of Brownian motion to account for spatial confinement.

2.3.3 Harmonic confinement

When a microsphere is optically trapped it experiences gradient and scattering forces, as discussed in Section 2.1. While trapped and in thermal equilibrium with the surrounding fluid, the microsphere undergoes Brownian motion. Obviously, the confinement imposed by the trap limits how far the microsphere may diffuse. Therefore, the statistical quantifiers of Brownian motion, like power spectral densities, autocorrelation functions, and mean-squared displacement, must be adapted. This section considers the effects of

confinement on Brownian motion with an emphasis on the results for a particle in air.

For small excursions $\mathbf{r}$ from the trap center, an optically trapped microsphere experiences a linear restoring force $F_{\mathrm{trap},i} = -k_i r_i$ along all three dimensions $i \in \{1, 2, 3\}$. Larger excursions couple the motion along different dimensions according to a *Duffing non-linearity*. The non-linear coupling effect is clear when considering Equation (2.42) for the gradient force in the Rayleigh regime. Expanding the force to third-order reveals

$$F_{\mathrm{trap},i}(\mathbf{r}) \approx -\kappa_i r_i \left(1 + \sum_{j=1}^{3} \zeta_j r_j^2\right) ,$$

where $\zeta_{1,2} = -2/w_0^2$, $\zeta_3 = -2/z_0^2$, and κ_i are the linear trap strength coefficients. In the Mie-scattering regime, a similar non-linear coupling can occur. For simplicity will assume strictly linear restoring forces and hence harmonic confinement:

$$F_{\mathrm{trap},i}(\mathbf{r}) = -\kappa_i r_i = m\omega_{0,i}^2 r_i \,, \tag{2.124}$$

where $\omega_{0,i} = \sqrt{\kappa_i/m}$ are the *natural frequencies* of the harmonic trap. Let us consider a single dimension and simplify notation to $F_{\mathrm{trap}}(x) = -\kappa x = m\omega_0^2 x$. The microsphere's potential energy is $U(x) = \kappa x^2/2$. The position x is now a quadratic degree of freedom so the equipartition theorem demands $\sigma_x^2 = k_{\mathrm{B}}T/\kappa$.

The one-dimensional Langevin equation of motion reads

$$m\ddot{x}(t) - F_{\mathrm{d}}[\dot{x}(t)] - F_{\mathrm{trap}}[x(t)] = F_{\mathrm{th}}(t) \,. \tag{2.125}$$

Expressing Equation (2.125) in terms of $v(t) = \dot{x}(t)$ and transforming to the frequency domain gives the admittance

$$\mathcal{Y}(\omega) = \left[\gamma(\omega) - i\omega m + i\kappa/\omega\right]^{-1} . \tag{2.126}$$

For a microsphere in a liquid, $\gamma(\omega)$ is given by Equation (2.119). Theoretical details [72] and experimental measurements [35] on a Brownian microsphere harmonically bound in a liquid will not be discussed further here. Instead, we will focus on the results for air-based optical trapping.

In air at temperature T with viscosity η, $\gamma(\omega) \approx \gamma_0 = 6\pi\eta R$. As a result, Equation (2.125) becomes the equation of motion for a thermally driven damped harmonic oscillator. The oscillation frequency is $\omega_1 = \sqrt{\omega_0^2 - (2\tau_\mathrm{p})^{-2}}$ where the momentum relaxation time is $\tau_\mathrm{p} = m/\gamma_0$. The system is underdamped when $\omega_0 > (2\tau_\mathrm{p})^{-1}$, over-damped when $\omega_0 < (2\tau_\mathrm{p})^{-1}$, and critically-damped when $\omega_0 = (2\tau_\mathrm{p})^{-1}$. Equations (2.105) and (2.79) give the (two-sided) velocity and position power spectral densities

$$S_{vv}(\omega) = \frac{2k_\mathrm{B}T}{\gamma_0} \frac{\omega^2}{\tau_\mathrm{p}^2(\omega^2 - \omega_0^2)^2 + \omega^2} , \tag{2.127}$$

$$S_{xx}(\omega) = \frac{S_{vv}(\omega)}{\omega^2} . \tag{2.128}$$

In Chapter 4 we shall find a use for the equivalent one-sided forms

$$S_{xx}(\omega) = \frac{4k_\mathrm{B}T\gamma_0}{(m\omega^2 - \kappa)^2 + \gamma_0^2\omega^2} , \tag{2.129}$$

$$S_{vv}(\omega) = \frac{4k_\mathrm{B}T\gamma_0\omega^2}{(m\omega^2 - \kappa)^2 + \gamma_0^2\omega^2} . \tag{2.130}$$

The position and velocity autocorrelation functions may be found via contour integration of Equation (2.107) and Equation (2.106), respectively. For this purpose, we may factorize the denominator of Equation (2.127) as

$$\tau_{\mathrm{p}}^2(\omega^2-\omega_0^2)^2+\omega^2=(\omega-\omega_{++})(\omega-\omega_{-+})(\omega-\omega_{--})(\omega-\omega_{+-})$$

where $\omega_{s's''}=s'\omega_1+s''i(2\tau_{\mathrm{p}})^{-1}$ and $s',s''\in\{+,-\}$. For $t>0$ ($t<0$), a lower- (upper-) half-plane semi-circular contour encloses the two poles with $s''<0$ ($s''>0$) such that the arc's contribution is zero and the residue theorem gives

$$C_{xx}(t)=\frac{k_{\mathrm{B}}T}{\kappa}\left(\cos\omega_1 t+\frac{\sin\omega_1|t|}{2\omega_1\tau_{\mathrm{p}}}\right)e^{-|t|/2\tau_{\mathrm{p}}}\,, \tag{2.131}$$

$$C_{vv}(t)=\frac{k_{\mathrm{B}}T}{m}\left(\cos\omega_1 t-\frac{\sin\omega_1|t|}{2\omega_1\tau_{\mathrm{p}}}\right)e^{-|t|/2\tau_{\mathrm{p}}}\,. \tag{2.132}$$

We can verify the equipartition theorem is satisfied by $C_{xx}(0)=\sigma_x^2=k_{\mathrm{B}}T/\kappa$ and $C_{vv}(0)=\sigma_v^2=k_{\mathrm{B}}T/m$. Equations (2.131) and (2.132) are valid for the under-damped case as well as the over-damped case by the identities $\cos i\theta=\cosh\theta$ and $\sin i\theta=i\sinh\theta$. Finally, the mean-squared displacement follows immediately from Equation (2.131) and Equation (2.72) as

$$\langle\Delta^2(t)\rangle=\frac{2k_{\mathrm{B}}T}{\kappa}\left[1-e^{-t/2\tau_{\mathrm{p}}}\left(\cos\omega_1 t+\frac{\sin\omega_1 t}{2\omega_1\tau_{\mathrm{p}}}\right)\right]\,. \tag{2.133}$$

As expected from Equation (2.73), $\langle\Delta^2(t\to\infty)\rangle=2\sigma_x^2$.

The effects of confinement may easily be accounted for in simulations of Brownian motion by the addition of a linear restoring force. In Figures 2.10 and 2.11 we show the position and velocity statistics (respectively) of a silica microsphere ($R=1.5\,\mu\mathrm{m}$, $\rho=1700\,\mathrm{g/cm^3}$) in air ($T=300\,\mathrm{K}$, and

$\eta = 18\,\mu\text{Pa}\,\text{s}$) and trapped harmonically with strengths $\kappa = 1\,\text{fN/nm}$ and $\kappa = 50\,\text{fN/nm}$. The simulations takes $N = 5 \times 10^5$ steps of size $\delta t = 200\,\text{ns}$ for a total time of $T_\text{r} = 100\,\text{ms}$. Statistical quantities are averaged over 100 independent simulations.

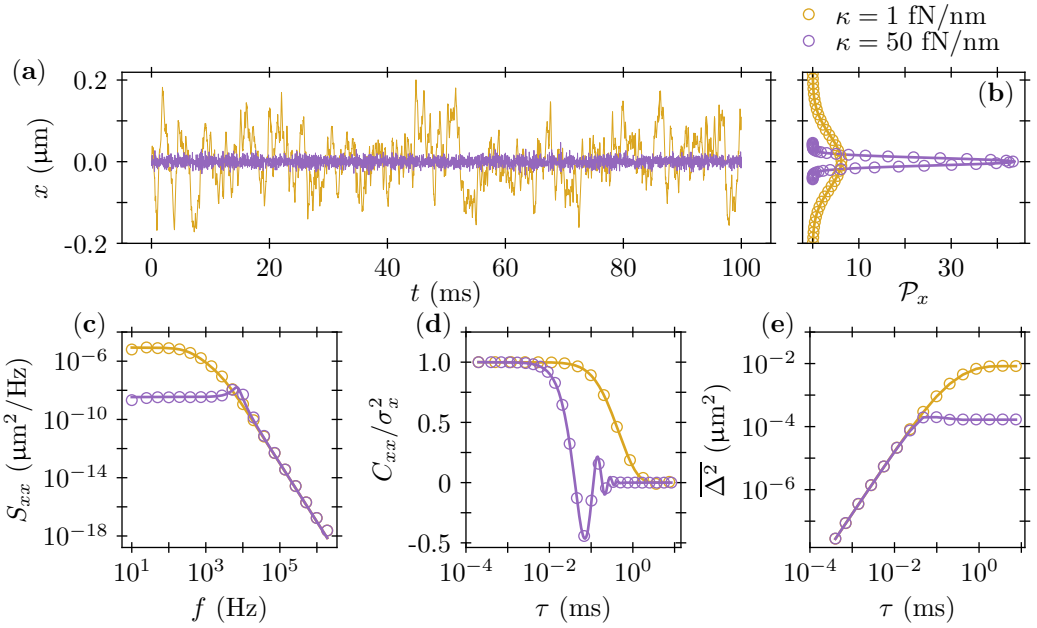

Figure 2.10: (**a**) The simulated position of a silica microsphere undergoing Brownian motion subject weak ($\kappa = 1\,\text{fN/nm}$, gold) and strong ($\kappa = 50\,\text{fN/nm}$, purple) harmonic confinement. The simulation (open symbols) and theoretical (solid curves) results are shown for the (**b**) position probability density, (**c**) position power spectral density, (**d**) normalized position autocorrelation function, and (**e**) mean squared displacement.

The raw position data in Figure 2.10 (**a**) shows large fluctuations around the trap center for a weak trap and small fluctuations for a strong trap. Figure 2.10 (**b**) shows the probability density of observed positions calculated as a histogram of the data in Figure 2.10 (**a**) compared to the theoretical curve

Equation (2.86) with $\sigma_x^2 = k_B T/\kappa$. Figure 2.10 (**c**) shows the position power spectral density calculated as the periodogram Equation (2.89) of simulated data compared to the theoretical curve Equation (2.129). Similarly, Figure 2.10 (**d**) shows the normalized position autocorrelation function $C_{xx}(\tau)/\sigma_{xx}^2$ calculated from the simulation data according to Equation (2.57) compared to the theoretical curve Equation (2.131). Finally, for the mean squared displacement Equation (2.59) provides the numeric implementation and Equation (2.133) provides the theoretical curve. Figure 2.11 is like Figure 2.10 but for the velocity degree of freedom $v(t)$ for which $\sigma_v^2 = k_B T/m$. Notice that harmonic confinement does not alter the total velocity variance but does alter how the variance is distributed in frequency space. We do not show the mean-squared velocity increment because it has not historically been of concern. In future studies, especially those venturing out of thermal equilibrium or to high-Reynolds-number flows, the mean-squared velocity increment and more-general *velocity structure functions* could be of interest.

Now we have cross-checked our numeric implementation and theoretical predictions of various quantifiers of harmonically-confined Brownian motion in air using simulated data. In the next section, we will return to hydrodynamics to understand acoustic forces on a trapped microsphere.

2.3.4 Acoustics

When a fluid is excited by a sudden compression event, energy is transported in the direction of compression in the form of acoustic radiation. As

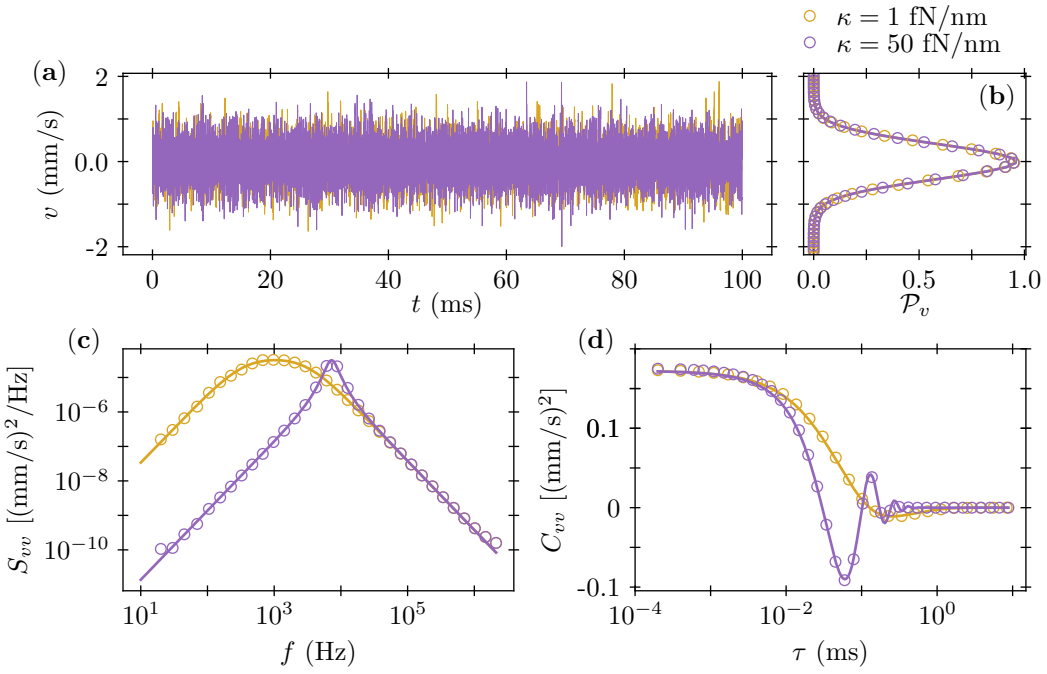

Figure 2.11: (**a**) The simulated velocity of a silica microsphere undergoing Brownian motion subject weak ($\kappa = 1\,\mathrm{fN/nm}$, gold) and strong ($\kappa = 50\,\mathrm{fN/nm}$, purple) harmonic confinement. The simulation (open symbols) and theoretical (solid curves) results are shown for the (**b**) velocity probability density, (**c**) velocity power spectral density, and (**d**) velocity autocorrelation function.

long as the compression is not too strong and the viscosity not too high, the radiation propagates without distortion as a longitudinal wave. Such is the regime of *linear acoustics*. In this section, elements of linear acoustics are developed to understand the motion of an optically trapped microsphere when driven by a linear acoustic wave.

In Section 2.3.2 we outlined four key simplifying assumptions to the Navier-Stokes equations. Assumption number 3. asserted the flow was incompressible, but that is no longer strictly valid when the flow supports acoustic waves. Instead, the conservation of mass requires

$$\frac{\partial}{\partial t}\rho_{\mathrm{f}}'(\mathbf{r},t) = -\rho_{\mathrm{f}}\nabla\cdot\mathbf{u}(\mathbf{r},t)\,, \tag{2.134}$$

where, as before, un-primed quantities represent the ambient fluid properties in the absence of a perturbation, the primed quantities represent the perturbation, and only terms linear in primed quantities are retained. At the same level of approximation, the conservation of momentum is expressed as Euler's equation of motion

$$\rho_{\mathrm{f}}\frac{\partial}{\partial t}\mathbf{u}(\mathbf{r},t) = -\nabla P'(\mathbf{r},t)\,. \tag{2.135}$$

Also as before, assumption 4. for a non-heat-conducting fluid implies adiabatic compression

$$P'(\mathrm{r},t) = \left(\frac{\partial P}{\partial\rho_{\mathrm{f}}}\right)_{\mathrm{s}}\rho_{\mathrm{f}}'(\mathbf{r},t) = c_0^2\rho_{\mathrm{f}}'(\mathbf{r},t)\,, \tag{2.136}$$

where c_0 is the speed of sound. Substituting Equation (2.136) into Equation (2.134) eliminates the density fluctuations in favor of the pressure fluctuations. Taking the time derivative of the result and comparing it to the

divergence of Equation (2.135) reveals the wave equation in pressure. Conversely, Taking the divergence of Equation (2.134) [after eliminating density fluctuations using Equation (2.136)] and comparing to the time derivative of Equation (2.135) reveals the wave equation in velocity. Critically, we see that a sound wave is a wave of pressure and a wave of velocity[9]

$$\left[\nabla^2 - \frac{1}{c_0^2}\frac{\partial^2}{\partial t^2}\right] P'(\mathbf{r},t) = 0\,, \tag{2.137}$$

$$\left[\nabla^2 - \frac{1}{c_0^2}\frac{\partial^2}{\partial t^2}\right] \mathbf{u}(\mathbf{r},t) = 0\,. \tag{2.138}$$

Solutions may be found by separating variables in a given coordinate system. As done for light waves in Section 2.1.2, plane wave solutions are found upon separating variables in Cartesian coordinates. Let us reset notation and refer to the perturbation $P'(\mathbf{r},t)$ as the *acoustic pressure* $p(\mathbf{r},t)$. Then plane wave solutions read

$$p(\mathrm{r},t) = p_0 e^{i(\mathbf{k}\cdot\mathbf{r}-\omega t)}\,, \tag{2.139}$$

$$\mathbf{u}(\mathrm{r},t) = \mathbf{u}_0 e^{i(\mathbf{k}\cdot\mathbf{r}-\omega t)}\,. \tag{2.140}$$

The wave amplitudes are p_0 and $\mathbf{u}_0$. The wave vector $\mathbf{k}$ points orthogonal to planes of constant pressure/velocity and velocity points in the direction of $\mathbf{k}$. The wave number $k = |\mathbf{k}| = 2\pi/\lambda$ is related to the circular frequency $\omega = 2\pi f$ through the speed of sound $c_0 = \omega/k = \lambda f$ where λ is the wavelength and f is the wave frequency. We can see that the fluid velocity and pressure of a

[9]Since density is proportional to pressure, sound is also a density wave. Additionally, the conservation of energy reveals a wave equation in temperature. Temperature and density waves will not be considered further here.

plane acoustic wave are in phase. Moreover, the amplitudes p_0 and $\mathbf{u}_0$ must be related such that momentum and mass are conserved. Without loss of generality, take $\mathbf{k} = k\hat{\mathbf{x}}$. Then $p(x,t) = p_0 e^{i(kx-\omega t)}$. Integrating the conservation of momentum gives $\rho_\mathrm{f} c_0 u_x(x,t) = p(x,t) + g(x)$ where $g(x)$ is an unknown function of position. Conversely, integrating the conservation of mass gives $\rho_\mathrm{f} c_0 u_x(x,t) = p(x,t) + f(t)$ where $f(t)$ is an unknown function of time. Thus, we conclude $g(x) = f(t) = 0$ and

$$p_0 = Z_0 |\mathbf{u}_0| \,, \tag{2.141}$$

where we have defined the *impedance* $Z_0 = \rho_\mathrm{f} c_0$. Clearly, the impedance depends on the medium properties through its density and sound speed. Perhaps less obvious is that this formula for the impedance was derived for plane wave solutions and thus the impedance also depends on the sound source's geometry. More generally, acoustic pressure and velocity need not be in phase and the impedance may be a complex function of frequency. For example, the impedance at a distance r from a spherical acoustic source of wave number k is

$$Z_\mathrm{sph}(r) = Z_0 kr \frac{kr + i}{kr + 1} \,, \tag{2.142}$$

while for a cylindrical source

$$Z_\mathrm{cyl}(r) = i Z_0 \frac{H_0^{(2)}(kr)}{H_1^{(2)}(kr)} \,, \tag{2.143}$$

where the $H_j^{(2)}(x)$ are Hankel functions of the second kind.

When an acoustic wave impinges on an object, the object experiences a force. For a small particle-like object, the force is caused by the local velocity

and pressure. In other words, write $\mathbf{u}(t)$ and $p(t)$ without spatial dependence to reflect the fact that forces are caused by fluid properties local to the particle. Such a description is valid as long as the particle's size and excursion remain much smaller than the length scale over which the fluid properties change in the sound wave (the wavelength λ).

The exact solution for the force on a sphere immersed in a harmonic sound wave of circular frequency ω (assuming a small Reynolds number and a non-heat-conducting fluid) is known [77]. The result is given as a transfer function $H(\omega) = \tilde{v}(\omega)/\tilde{u}(\omega)$ where $\tilde{u}$ is the Fourier velocity amplitude of the fluid and $\tilde{v}(\omega)$ is the Fourier velocity amplitude of the sphere. From this exact solution, the incompressible limit $\omega\eta/\rho_{\mathrm{f}}c_0^2 \ll 1$ may be found. A simpler calculation [78,79] arrives at the same result by using Equation (2.114) for the force on the sphere due to the fluid-velocity wave. The force due to the pressure wave is proportional to the pressure gradient. Integrating Equation (2.135) over the volume of the sphere with a diameter assumed small compared to the acoustic wavelength suggests the pressure gradient force is

$$\mathbf{F}_{\nabla}(t) = -\frac{4}{3}\pi R^3 \nabla P(t) = \delta m \dot{\mathbf{u}}(t)\,. \tag{2.144}$$

In one dimension, we may write the net external force caused by the sound wave as $F_{\mathrm{ext}}(t) = F_{\mathrm{d}}[-u(t)] + F_{\nabla}(t)$. The one-dimensional equation of motion for an optically trapped microsphere is

$$m\dot{v}(t) - F_{\mathrm{d}}[v(t)] - F_{\mathrm{trap}}[x(t)] = F_{\mathrm{th}}(t) + F_{\mathrm{ext}}(t)\,. \tag{2.145}$$

For the moment let us ignore the thermal force so that

$$\begin{aligned} m\dot{v}(t) - \delta m\dot{u}(t) + \frac{1}{2}\delta m\left[\dot{v}(t) - \dot{u}(t)\right] \\ + \gamma_0\left(v(t) - u(t) + \sqrt{\frac{\tau_\mathrm{f}}{\pi}}\int_{-\infty}^{t}\mathrm{d}t'\,\frac{\dot{v}(t') - \dot{u}(t')}{\sqrt{t-t'}}\right) + \kappa x(t) = 0\,. \end{aligned} \tag{2.146}$$

Assume a harmonic drive $u(t) = u_0 e^{-i\omega t}$ and response $v(t) = v_0 e^{-i\omega t}$ so that $\dot{u}(t) = -i\omega u(t)$, $\dot{v}(t) = -i\omega v(t)$, and $x(t) = iv(t)/\omega$. As done in Section 2.3.2, make the substitution $s = \sqrt{t-t'}$ to evaluate the history term. Solving for the transfer function $H(\omega) = v/u$ gives

$$H(\omega) = \frac{\gamma(\omega) - i\omega\delta m}{\gamma(\omega) - i\omega m + ik/\omega} = \mathcal{Y}(\omega)\left[\gamma(\omega) - i\omega\delta m\right]\,, \tag{2.147}$$

where $\gamma(\omega)$ is given by Eq (2.119). Equation (2.147) exposes the contribution of the pressure gradient force $-i\omega\delta m = -2i\gamma_0\omega\tau_\mathrm{f}/9$ and the optical trap $i\kappa/\omega$ to the transfer function. In terms of time scales τ_f and τ_p we have

$$H(\omega) = \frac{A + iB}{A + iC}\,, \tag{2.148}$$

$$A = \omega\left(1 + \sqrt{\omega\tau_\mathrm{f}/2}\right)\,, \tag{2.149}$$

$$B = -\omega\sqrt{\omega\tau_\mathrm{f}/2}\left(1 + \frac{2}{3}\sqrt{\omega\tau_\mathrm{f}/2}\right)\,, \tag{2.150}$$

$$C = \tau_\mathrm{p}\left(\omega_0^2 - \omega^2\right) - \omega\sqrt{\omega\tau_\mathrm{f}/2}\left(1 + \frac{2}{9}\sqrt{\omega\tau_\mathrm{f}/2}\right)\,. \tag{2.151}$$

The transfer function gives the oscillation amplitude and phase of the microsphere's motion relative to the amplitude and phase of the sound wave. The transfer function amplitude and phase are

$$h(\omega) = |H(\omega)| = \sqrt{\frac{A^2 + B^2}{A^2 + C^2}}\,, \tag{2.152}$$

$$\phi(\omega) = \mathrm{Arg}[H(\omega)] = \arctan\left(\frac{AB - AC}{A^2 + BC}\right)\,, \tag{2.153}$$

so that $H(\omega) = h(\omega)e^{i\phi(\omega)}$.

In Figure 2.12 we plot the amplitude and phase of the velocity transfer function for acoustic frequencies from 100 Hz to 1 MHz assuming a silica microsphere of radius $R = 1.5\,\mu\text{m}$ trapped with strength $\kappa = 10\,\text{fN/nm}$ in air. On the same axes, we also plot two limiting cases for otherwise identical parameters: 1) $\delta \to 0$, i.e. the only damping is from the Stokes contribution $\gamma(\omega) \to \gamma_0$ and the pressure gradient is ignored, giving

$$H(\omega) = \frac{\gamma_0\omega}{\gamma_0\omega - i(m\omega^2 - k)} = \frac{\omega}{\omega - i\tau_{\text{p}}(\omega^2 - \omega_0^2)}\,, \tag{2.154}$$

and 2) $\kappa \to 0$ while also accounting for compressibility effects, i.e. the exact solution for an unbound particle [77]. The transfer function developed in this section is labeled simply "Basset" in Figure 2.12 even though effects of harmonic confinement, added mass, and acoustic pressure gradient are accounted for.

We see that our model interpolates between the low-frequency Stokes-dominate solution and the high-frequency trap-independent solution. The Stokes-only model applies to Brownian motion in air, but Basset-force corrections become relevant in high-frequency acoustic fields. For example, at 1 MHz, the Stokes-only model underestimates the amplitude by a factor of ~ 2 and overestimates the phase by $\sim \pi/6$ radians. On the other hand, the Basset model agrees very well with the exact model at 1 MHz since compressibility effects may safely be neglected, though the fluid's memory and inertia can not.

This Chapter has covered significant theoretical ground. Section 2.1 in-

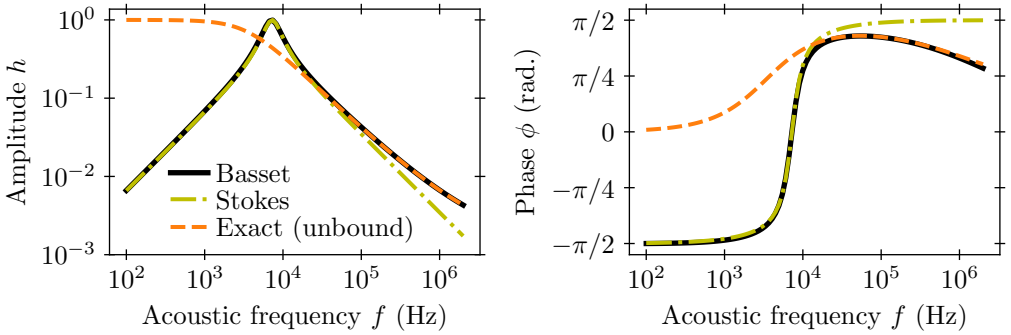

Figure 2.12: The transfer function (**a**) amplitude and (**b**) phase compared for different models: Equation (2.148) is the black, solid line, Equation (2.154) is the gold, dot-dashed line, and the exact solution for an unbound microsphere including compressibility effects [77] is the orange, dashed line.

troduced the concept of optical trapping through ray optics, Rayleigh scattering of Gaussian beams, and most generally, the Mie scattering regime. Section 2.2 was purely mathematical; we defined stochastic processes and described how to analyze the signals they generate. Special attention was given to the power spectral density. Finally, Section 2.3 considered Brownian motion as a stochastic process driven by thermal fluctuations and subject to hydrodynamics and harmonic confinement. We verified our numeric routines for calculating statistical quantities using simulated digitized signals. Furthermore, we leveraged the hydrodynamic theory to calculate the acoustic radiation force on small spheres in the absence of thermal fluctuations. All of the results presented in this chapter are standard but lead into the two key results of this dissertation presented in Chapter 4. Specifically, 1) in thermal equilibrium, fitting the position power spectral density reveals the inertial mass of an optically

trapped microsphere. 2) When perturbed by an acoustic wave, the velocity transfer function provides a means of making quantitative, high-bandwidth measurements of the perturbing field. Before detailing these results, we next describe the apparatus and equipment used to make the measurements.

Chapter 3

Experimental set-up

This Chapter details the experimental apparatus used for equilibrium inertial mass measurements and acoustic sensing. Figure 3.1 provides a basic block diagram. At the highest level of abstraction, the experiment operates in a pulsed mode with two synchronized digitizers for reading data. One digitizer is faster (GaGe 1622 up to 200 MHz sampling rate) and one is slower (National Instruments 6259 up to 2 MHz sampling rate). Synchronization is provided by an external clock source (Stanford Research Systems DS345.) The fast digitizer collects signals from primary sensors like the microsphere's position or a reference microphone. The slower digitizer collects signals from auxiliary sensors like the trapping laser power and air temperature. Multiple nearly-contiguous acquisitions, each referred to as a *record*, may be made from a single external trigger. It is useful to split the data into a collection of records at the level of data acquisition (instead of in post-processing) for organizational reasons. Each record may be considered an independent realization of identical measurements and therefore makes up an ensemble to average. Furthermore, the data stream from the slow digitizer is averaged over time for each record.

It is instructive to walk through an example of an acquisition sequence

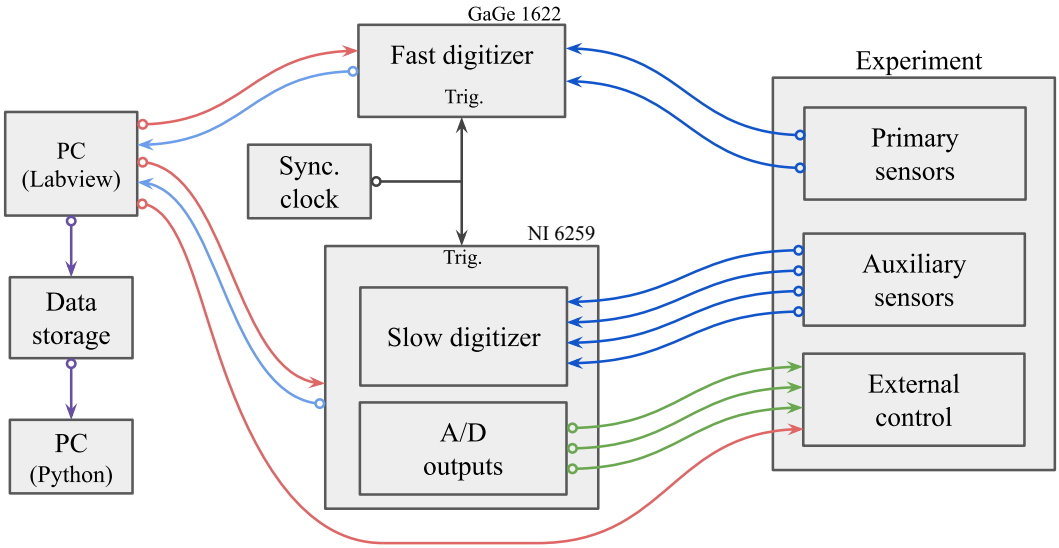

Figure 3.1: The experimental apparatus is represented as simplified blocks. One personal computer (PC) runs a custom LabView control loop. User input (red arrows) is sent to the fast digitizer and the NI control card to set up acquisition parameters. User input is also sent directly to the experiment and the loop waits for the update to complete (e.g. setting a new laser power) before arming the acquisition triggers. At the next rising edge of the synchronizing clock, the digitizers simultaneously begin their independent acquisitions (dark blue arrows). Simultaneously, stimuli may be sent to the experiment while data is being acquired (green arrows). After all the requested data has been collected, it is transferred to the control PC (light blue arrows). The data is optionally saved to an external storage device and subsequently loaded to a (possibly different) PC (purple arrows) for analysis with custom Python libraries.

to understand how the data is organized. Set the fast sampling rate to $f_{s,1} = 25\,\mathrm{MHz}$ and the slow sampling rate to $f_{s,2} = 250\,\mathrm{kHz}$. Collecting $N_1 = 2^{16}$ samples per record at $f_{s,1}$ corresponds to a record time of $T_r = 2.6\,\mathrm{ms}$. For the slow digitizer to collect over the same amount of time, the control loop will automatically set $N_2 = T_r f_{s,2} = 650$ (rounded to the nearest integer). Since the slow digitizer records the experimental conditions like temperature and laser power that we expect to change on time scales much longer than T_r, each such record is averaged over all N_2 points per record. Collecting $M = 10$ records per collection means that the external clock frequency should be set to $f_{trig} \leq (MT_r)^{-1} = 38\,\mathrm{Hz}$. Finally, the control loop can run multiple trials of a collection with the same experimental parameters or loops over several varying control parameters. The data is optionally saved to an external drive in the LabView TDMS format that may then be opened in Python (npTDMS library) for further analysis.

The remainder of this Chapter is organized as follows: First, in Section 3.1 we describe the optical trapping setup and microsphere position detection scheme. Then, in Section 3.2 we describe our method for releasing and trapping individual microspheres. Finally, in Section 3.3 we discuss the various acoustic sensors and sources used in the sound detection experiment.

3.1 Optics and alignment

We now turn to a description of the optics used for trapping, monitoring, and exciting a microsphere.

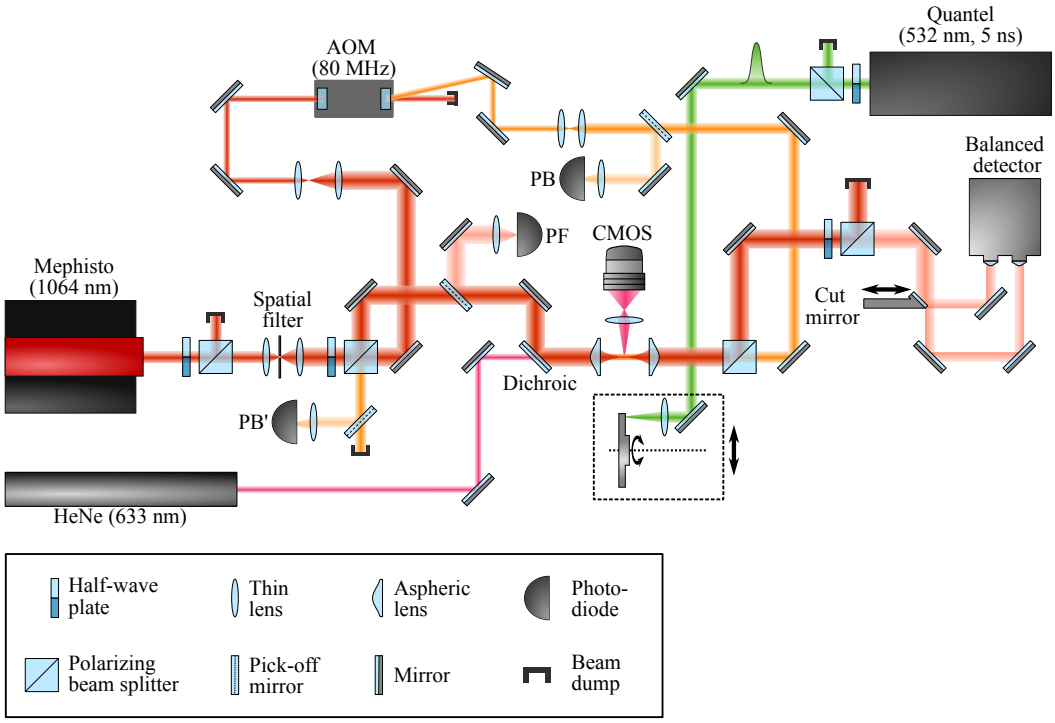

Figure 3.2: Laser table schematic. The optical trap is formed by a 1064 nm continuous-wave laser split into two counter-propagating beams and focused by identical aspheric lenses. Two photodiodes are used to monitor each beam's input power (PF and PB). An additional photodiode monitors the backward beam's output power (PB'). The forward beam is used to detect the microsphere's motion by splitting its wavefront and detecting the power imbalance between each beam half. A 633 nm HeNe laser is used for visible-wavelength imaging. A 532 nm, 5 ns pulsed laser is used to ablate an aluminum target and generate acoustic impulses.

Figure 3.2 depicts a schematic of the laser table setup. The trap is formed by a continuous-wave, 1064 nm laser (Innolite [now a Coherent] Mephisto). The Mephisto consists of a monolithic Nd:YAG crystal in the non-planar ring oscillator configuration, capable of up to 1.2 W of output. Using the built-in noise eater, the output is shot-noise limited above $\sim 1\,\mathrm{MHz}$. Light exits the laser head and its power is adjusted by manually tuning a half-wave plate in front of a polarizing beam splitter. Then, a beam-expanding telescope and a 10 µm diameter pinhole form a spatial filter that provides a collimated Gaussian mode with a diameter of 3.6 mm.

A second half-wave-plate-polarizing-beam-splitter pair is used to split the beam into two parts. The s-polarized component (the one reflected by the beam splitter) is referred to as the *forward beam*. The forward beam is sampled using a pick-off mirror and measured with a photodiode (PF) so that its power may be monitored during the experiment. Then, two mirrors divert the forward beam through an aspheric lens (numeric aperture 0.7, Thorlabs C330TMD-C), forming the first half of the optical trap. Meanwhile, the p-polarized component passing through the beam splitter is called the *backward beam*. The backward beam passes a beam-reducing telescope before entering an acousto-optical modulator (AOM, IntraAction Corp ATM-801A6, with driver ME-802). The AOM provides convenient intensity control of the backward beam as well as an 80 MHz frequency shift relative to the forward beam. A smaller input diameter improves the coupling efficiency through the AOM (about 80% here). The backward beam is then expanded to 2.6 mm, sampled

with a pick-off mirror for power monitoring (photodiode PB), and directed into a second aspheric lens to from the second half of the trap. Cross polarization and 80 MHz of relative detuning ensure interference does not affect the trap potential.

Passing through the trap waist, both the forward and backward beams are recollimated by the opposite aspheric lens. The backward beam retraces the forward beam's path until it hits the beam splitter that initially separated the two beams. Here, the backward beam passes through the cube and is sampled on a photodiode (PB') for alignment purposes. The forward beam emerges from the trap and is immediately separated from the backward beam using another polarizing beam splitter. Once separated, the forward beam has its power reduced using another half-wave-plate-polarizing-beam-splitter pair before it enters the detection system.

For detection, the wavefront is split using a sharp D-shaped mirror (Thorlabs BBD05-E03). The wavefront halves are diverted into the two ports of a balanced photodetector (75 MHz bandwidth, Thorlabs PDB120C) whose signal is proportional to the difference in optical powers between each half. The cut mirror is mounted on a motorized stage (Thorlabs TDC001). Balance is maintained over long periods by actuating the stage to zero the detector signal between acquisitions. More details on the detection system are provided in Section 3.1.2.

Figure 3.2 also depicts a simple imaging system. A 633 nm HeNe laser beam (4 mW, Gaussian mode diameter 4 mm) is directed colinear to the

forward beam and into the trap. The forward beam's final pre-trap mirror is dichroic to let the 633 nm light pass. Light scattered from microspheres is collected by a magnifying lens and imaged onto a complementary metal-oxide-semiconductor camera (CMOS, Thorlabs DCC1545M). The imaging system helps while tapping microspheres and ensuring the trap is singly occupied. Releasing and capturing microspheres is discussed further in Section 3.2.

Finally, Figure 3.2 shows a third laser (Quantel); it is a flash-lamp-pumped, Q-switched, frequency-doubled Nd:YAG laser. The 532 nm wavelength pulses are 5 ns long and fired at a repetition rate of up to 50 Hz. Each pulse has a peak energy of up to 200 mJ and a flat-top mode shape. A half-wave-plate-polarizing-beam-splitter pair controls the nominal pulse energy. Laser pulses are focused through a lens and onto an aluminum target near the optical trap. The pulsed laser is not part of the trapping or measuring system but is used to generate fast acoustic pulses via laser ablation. The focusing lens and aluminum target are mounted on a motorized stage (Velmex MA1515K2S1.5) to control the distance between the acoustic source and the optical trap. Additionally, the target has circular symmetry and may be rotated around its axis using a stepper motor (Newport 8401). By rotating the target between shots, a fresh surface may be ablated for each trial. In Chapter 4 we show the microsphere's response to such an acoustic impulse as well as other non-laser-based sound sources that may be mounted on the same motorized stage.

A few optics are not shown in Figure 3.2. Neutral density filters re-

duce the optical power entering the photodiodes PF, PB, and PB' so that the sensors do not saturate. A 633 nm rejecting line filter is placed at the forward beam's trap exit so that only the 1064 nm forward beam enters the detection system. Additionally, the power-reducing beam splitter in the detection system has an unused port. This port may be unblocked, the wave-front rotated by 90 degrees using a dove prism [80], and then sent to an identical detection system. By rotating the beam front, this detection system is sensitive to the microsphere's motion in the transverse direction orthogonal to the depicted detection system, thereby enabling two-dimensional tracking of the microsphere. Alternatively, the dove prism may be removed and a home-built high-saturation-power balanced detector may be swapped for the commercial balanced detector. Our home-built system has superior sensitivity [35, 81], but is AC coupled and therefore requires a careful calibration transfer from the DC-coupled, lower-sensitivity commercial detector. For the experiments reported on in Chapter 4, only one commercial detector is used to track the motion in one dimension for simplicity and proof-of-principle.

Connecting to the language of Figure 3.1, we identify the balanced detector as a primary sensor. The three photodiodes are auxiliary sensors. The two linear stages, one rotary stepper motor, and the pulsed laser's flash lamp energy are actuated by the control PC between acquisitions. The pulsed laser's flash lamp and Q-switch may be triggered during an acquisition. Additionally, the temperature is tracked using a platinum resistance thermometer (Omega RTD-3-F3102-36-T, read by Lakeshore 211). The sensor head is mounted in

free space near the optical trap.

While most of the optical components depicted in Figure 3.2 may be aligned using standard methods, special attention is required to align the counter-propagating beams through the trap lenses. In the next section, we will describe the alignment techniques employed for reliable and repeatable trapping.

3.1.1 Pinhole alignment

Recall in Section 2.1 we found that a $\sim$1 µm silica sphere near the intensity maximum of a tightly focused beam experiences significant scattering forces leading to unstable trapping in the longitudinal direction. We also saw how an additional counter-propagating beam can stabilize the trap by applying an equal and opposite scattering force. In practice, the two counter-propagating beams must be aligned very accurately. Otherwise, the scattering forces do not cancel and can instead drive an out-of-equilibrium circulating motion [82, 83]. While it is often stated that the trapping position is midway between the two trapping beams' foci, the stable point of a dual-beam optical trap introduces additional subtleties: up to four stable trapping positions may be found along the optical axis [84, 85]. For these reasons, reliable and repeatable alignment of the two counter-propagating beams is required. This section is devoted to a detailed description of our alignment procedure.

The aspheric lens focusing the forward beam is housed (Thorlabs E09RMS) and mounted (Thorlabs HCS013) on a fixed aluminum block. The backward

beam's aspheric lens is similarly mounted on a three-axis translation stage (Thorlabs MBT616D). Alignment is performed in two stages of increasing accuracy. The first step is to bring both beams and aspheric lenses onto the same optical axis as a one-to-one telescope. In the second step, alignment is refined using a pinhole between the two lenses to set a common point through which both beams are focused.

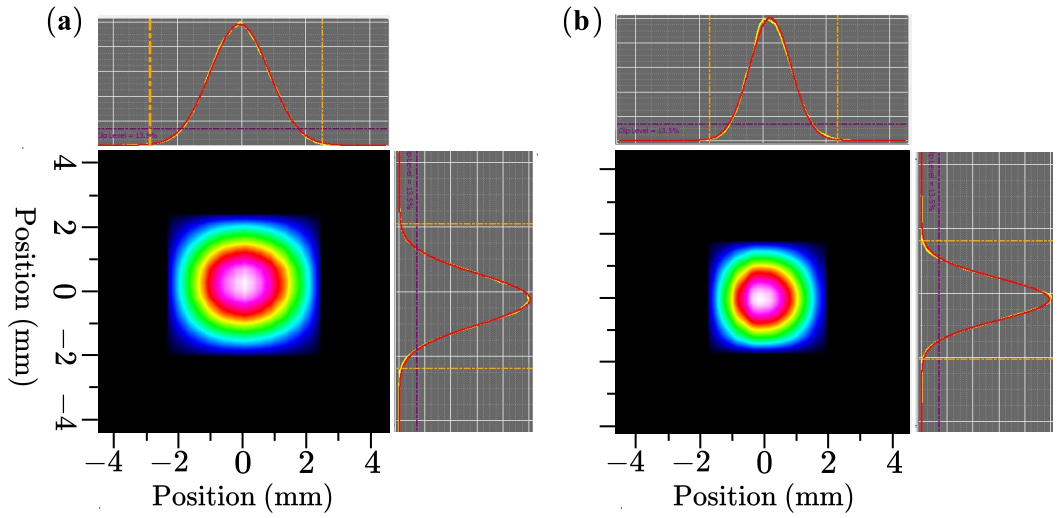

Figure 3.3: The transverse profile of the (**a**) forward and (**b**) backward beams just before entering the trap. These images were captured with the beam profiler software and edited for aesthetics in post-processing. Care was taken to ensure the position scales remain accurate.

The first step in the alignment is to set the optical axis as the forward beam. A beam profiler (Thorlabs BP109-UV) should show a clean, and unchanging Gaussian mode as it is translated parallel to the laser table's hole pattern. The fixed aspheric lens must then be placed in the beam line. Trans-

lating the beam profiler just downstream of the lens' focus should show a growing-but-otherwise-unmoving Gaussian mode. Then the translation-stage-mounted aspheric lens is brought into the beam line. If both lenses are well aligned, the downstream beam profile should look the same whether or not the trap lenses are installed. Additionally, as the kinematic lens is translated along the optical axis, the downstream profile should change in size but not position or symmetry. Finally, the backward beam is aligned through the trap lenses such that its downstream profile looks the same whether or not the trap lenses are installed. Figure 3.3 shows the beam profiles of the forward and backward beams just before they enter the trap.

The second step in aligning the optical trap is to ensure both beams are focused through the same point using a pinhole. Figure 3.4 (**a**) shows a 3D rendering of the optical trap components set up for pinhole alignment. Between the two lenses sits an L-shaped aluminum platform. The long arm of the L extends underneath the trap and the short arm is mounted to a three-dimensional translation stage (Thorlabs NanoMax 300) equipped with piezoelectric actuation for fine-tuning (Thorlabs MDT693B open loop piezo controller). Two screws secure a custom pinhole clamp to the long end of the L. The clamp has a V-shaped groove to increase the placement accuracy when installing or changing pinholes. Figure 3.4 (**b**) depicts the technical drawing used to machine the pinhole clamp. Efforts must be made to align the pinhole axis to the translation axis of the stage and the optical axis of the trap. Once installed, the pinhole stage's micrometers are adjusted so

that the forward beam's throughput is maximized. The maximization can be done using the signal from the split beam detector after fully retracting the cut mirror. Then, the throughput of the backward beam is maximized by adjusting three micrometers of the kinematic lens' stage and monitoring the signal from the backward beam's post-trap photodiode (PB'). It is helpful to first align a larger (20 µm) pinhole and then switch to a smaller (5 µm) pinhole. We have been unable to find a signal using an even-smaller 2 µm pinhole.

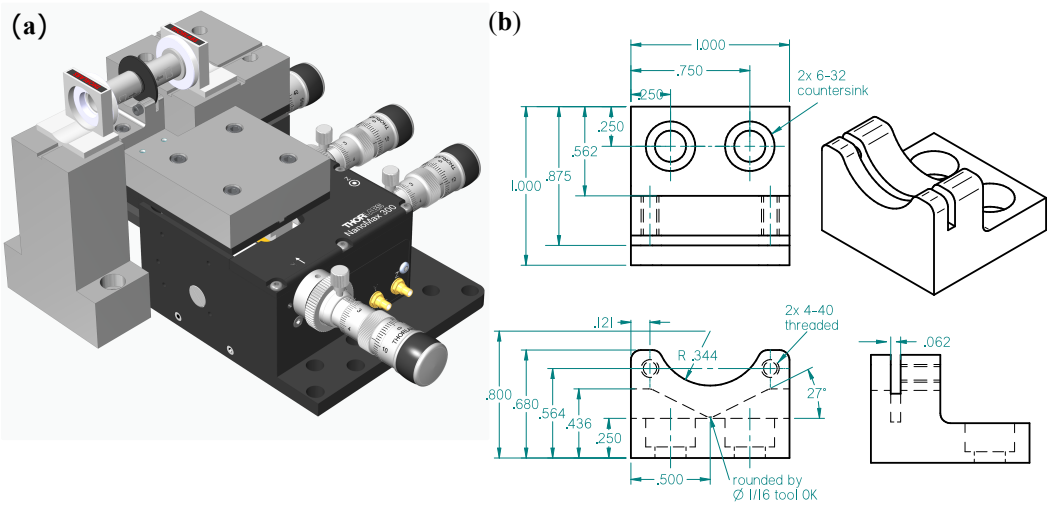

Figure 3.4: (**a**) Rendering of the optical trap set up for pinhole alignment. (**b**) Technical drawing of the removable pinhole clamp, including details of the V-shaped groove.

The pinhole stage's piezo driver is computer controlled and can be raster-scanned in three dimensions. Scanning the pinhole and simultaneously recording the signals from the post-trap photodiodes reveals an approximate map of the light field inside the trap. These maps are approximate because

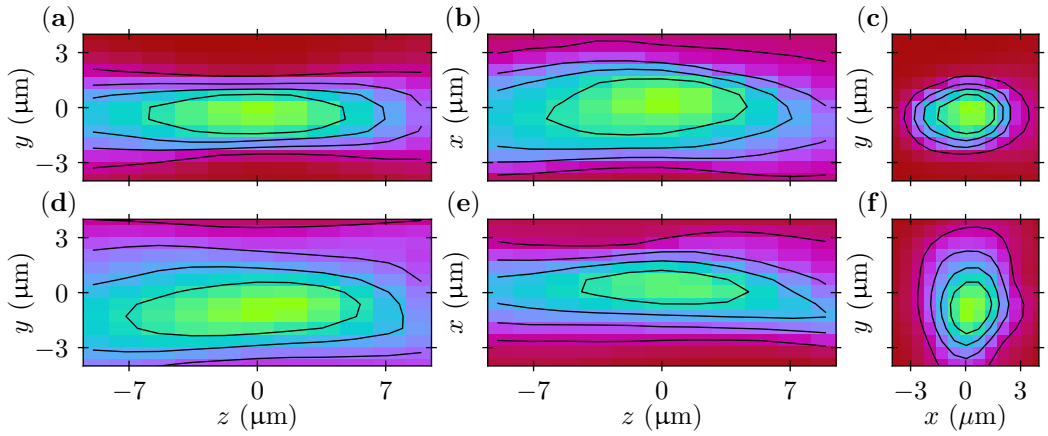

Figure 3.5: By scanning a 5 µm pinhole in the vicinity of the trap center, we approximately measure the trap's intensity distribution. $25 \times 25 \times 10 = 6250$ points (10 points along z) were measured over 20 µm^3 volume. (**a** - **c**) Slices of the forward beam's intensity distribution. (**d** - **f**) Slices of the backward beam. All slices are taken through the intensity maximum (normalized to unity). The intensity maximum of the forward beam sets the origin of the coordinate system.

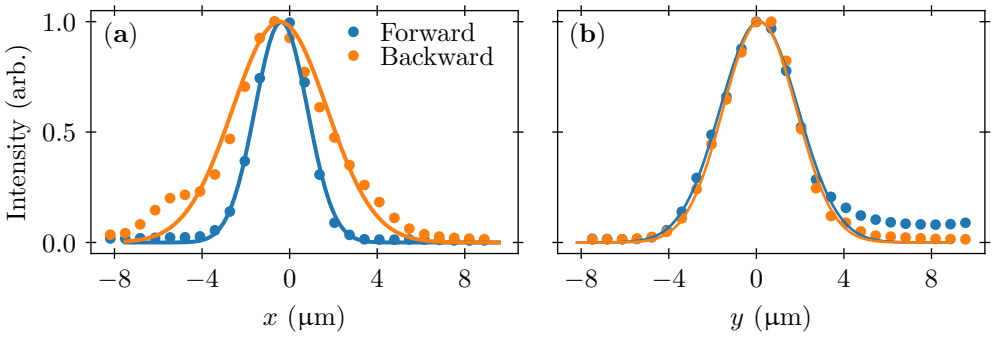

Figure 3.6: Line-cuts of the data shown in Figure 3.5(**c**) and (**f**). Gaussian fits (solid lines) estimate the trap waists and alignment accuracy for the (**a**) x direction and (**b**) y direction.

no account is taken for diffraction effects even though the pinhole diameter is on the order of the waist and wavelength of the trapping light. Cyclically measuring the trap profile and making small adjustments to the translatable aspheric lens' position enables our most sensitive alignment check. Once both foci are coincident, the backward beam is translated along the optical axis such that the two foci are separated by about 25 µm. In our experience, slightly separated foci more reliably trap a single microsphere at a time.

Table 3.1: The fitting parameters corresponding to the solid curves in Figure 3.6. Reported uncertainties are purely statistical; they are the diagonal entries of the fitting parameter covariance matrix (as returned by the Scipy non-linear least squares fitting function `curve_fit`) to the one-half power. Due to diffraction effects, the actual waists are likely smaller than the measured waists.

		w_0 (µm)	q_0 (nm)
Forward	x	3.56 ± 0.11	129 ± 65
	y	2.39 ± 0.04	-384 ± 23
Backward	x	3.34 ± 0.05	152 ± 30
	y	4.31 ± 0.14	-445 ± 84

Figure 3.5 shows two-dimensional slices of an alignment scan and Figure 3.6 shows one-dimensional transverse line-cuts through the intensity maximum. The signal from each beam is normalized by its maximum value. Furthermore, the zero of the coordinate axes for both beams is taken as the intensity maximum of the forward beam. Fitting the normalized transverse line cuts to the form $e^{-2(q-q_0)^2/w_0^2}$ provides a basic estimate of the trap waist w_0 and alignment offset q_0 along the coordinate $q \in \{x, y\}$ for both the forward and backward beams. A summary of the fit parameters is reported in Table

3.1. Using the scanning pinhole method, we can reduce the alignment offset to within a couple-hundred of nanometers. More precise alignment adjustments would require piezo actuation of the lens that is not currently available in our setup.

3.1.2 Split-beam detector

In this Section, we explain how the split beam detector works and estimate the voltage signal given a displacement of the microsphere. Then we consider sources of noise and their effects on measurements.

In Section 2.1.1 we saw how a microsphere offset from the focus of converging light rays experiences a restoring force back towards the focus. An additional effect is also apparent in Figure 2.1: When the microsphere is displaced from the optical axis, the primarily-transmitted rays deflect in the same direction as the microsphere's displacement. In the case of a dual beam optical trap, the deflected rays are collected and re-collimated by the counter-propagating beam's focusing lens. The collimating lens converts the angular deflection to a lateral offset. Measuring the offset of a trapping beam after it passes the microsphere provides a measurement of the microsphere's position. The cut mirror and balanced detector achieve this measurement.

Internally, the balanced detector consists of two photodiodes wired in the push-pull configuration. In this configuration, the power imbalance $P_2 - P_1$ between the two photodiodes generates a proportional photocurrent. The proportionality constant is called the *responsivity* and is $Q = 0.7\,\mathrm{A/W}$ at

1064 nm. Proportionality is only guaranteed if the input power is less than the saturation threshold $P_{\text{sat}} = 20\,\mu\text{W}$. A high-gain and low-noise transimpedance amplifier converts the small photocurrent difference into a large voltage signal. The transimpedance gain is $A = 180 \times 10^3\,\text{V/A}$. When the microsphere moves a distance x the detection power $P = P_2 + P_1$ is imbalanced by an amount $P_2 - P_1 = GxP$ where G is a geometric factor with units of inverse length. Precise calculation of G requires Mie scattering theory, but in the Rayleigh approximation one finds [86] $G \sim \lambda^{-1} D^3 / w_0^3$ where $D = 2R$ is the microsphere diameter, w_0 is the trap waist, and λ the trapping wavelength. Conversely, in the ray optics picture, the microsphere is much larger than the wavelength of light, so the wave properties at length-scales λ drop out of the problem. Dimensional analysis then suggests $G \sim D^{-1}$. In our experiment $D \approx 3\,\mu\text{m}$, $w_0 \approx 4\,\mu\text{m}$, and $\lambda \approx 1\,\mu\text{m}$, so it is reasonable to expect $G \approx 1\,\mu\text{m}^{-1}$ within a factor of 10. Combining the above considerations leads to an estimate for the detector *position calibration factor* relating the detector voltage V and the microsphere position x:

$$\beta = \frac{V}{x} = GPQA\,. \tag{3.1}$$

Setting $P = P_{\text{sat}}$ we estimate $\beta \approx 2.5\,\text{mV/nm}$. In Chapter 4 we will describe a method for measuring β based on Brownian motion in thermal equilibrium. Now that we understand how the balanced detection system works, a few comments regarding noise are in order. First, we discuss noise due to signal digitization then we focus on noise originating from the laser.

A digitizer used L bits $b_k \in \{0, 1\}$, $k = 0, 1, \ldots, L-1$ to encode each

voltage measurement $V = V_{\text{low}} + \mathcal{Q} \sum_k b_k 2^k$ where $\mathcal{Q} = (V_{\text{high}} - V_{\text{low}})/2^L$ is the *conversion resolution*, and $V_{\text{low}} = -V_{\text{high}}$ set the conversion's full-scale range. The bit string $\{b_k\}$ represents the voltage V. Due to the finite resolution of digitization, *quantization error* is introduced into the measured signal. In an ideal measurement, the signal occupies the full-scale range while quantization noise is confined to the least significant bit.

Of course, a digitizer also samples discretely in time at a rate f_{s}. Additional digitization error occurs from timing inaccuracies known as *jitter*. Small fluctuations in the sampling period $\delta t = 1/f_{\text{s}}$ can lead to errant measurements, especially for signals with high slopes. Quantization error, jitter, and other noise sources are combined into a digitizer's figure of merit known as the *effective number of bits* L'. We estimate the uncertainty in voltage measurements as half the conversion resolution evaluated with L'[1]. For the GaGe 1622 digitizer, $L' = 11.4$. Hence for a full-scale range of $\pm 1V$, we find a measurement uncertainty 601 µV. Bin averaging M uncorrelated measurements [see Equation (2.52)] reduces the uncertainty due to digitization by a factor $M^{-1/2}$.

The fastest resolvable signal must contain frequencies no larger than the *Nyquist frequency* $f_{\text{s}}/2$. Signals with frequencies greater than the Nyquist frequency will be *aliased*. In an aliased measurement high-frequency power will be incorrectly folded down to lower frequencies. Aliasing can be minimized by using a sampling rate f_{s} much larger than the highest signal frequency of

[1] Thermal *Johnson noise* (1 µV for 50 Ω at 1 MHz) is often smaller than digitization noise (31 µV for 16 bits at 2 V full scale) and therefore neglected here.

interest $f_{\max}$. We further low-pass filter the signal before digitization at a cutoff frequency f_c such that $f_{\max} \ll f_c \ll f_s$. Typical values for the GaGe 1622 digitizer in our experiment are $f_s = 25\,\text{MHz}$ and $f_c = 4\,\text{MHz}$ (Crystek CLPFL-0004-BNC).

The laser beam used to detect the microsphere's motion is subject to a variety of noise sources. Thermal noise in the laser head causes slow power drifts on the scale of seconds. Relaxation oscillations — an effect due to the quantized energy levels of the laser's gain medium — cause power fluctuations on the scale of microseconds. Both of these effects are mitigated by the laser's built-in noise eater and the common-mode rejection of the balanced photodiodes.

On the other hand, pointing instability of the laser and mechanical vibrations throughout the system are not common-mode and therefore contribute to the detection noise. Mechanical vibrations are minimized by mounting the system on a monolithic air-lifted optical table and setting the optical axis of the system relatively low (4 inches above the table). Additionally, the optical setup is enclosed in a multi-chamber acrylic box to minimize airflow and stabilize temperatures. The intrinsic pointing instability of the laser is quite low [87]. However, 60 Hz power line harmonics cause additional peaks in the noise spectrum that appear to manifest as pointing instabilities. Sometimes, audible acoustic noise can also be identified in the noise spectrum.

Even a perfect laser source is subject to shot noise due to the quantized nature of light. If the photons comprising the detected laser beam are of

frequency ω_0 and are detected at time t_i then the incident power is $P(t) = \hbar\omega_0 \sum_i \delta(t - t_i)$. Denote the average incident power as $\bar{P}$. Using properties of delta functions and definition (2.65) for the power spectral density gives [88]

$$S_{PP}(\omega) = \bar{P}^2\delta(\omega) + \bar{P}\frac{\hbar\omega_0}{2\pi}\,. \tag{3.2}$$

The first term represents the average signal power while the second represents uncorrelated (white) shot noise. Hence the relative uncertainty due to shot noise decreases as $\sim \bar{P}^{-1/2}$. Increasing the average power reduces the shot noise, but the saturation threshold of the detector's photodiodes limits the utility of this approach (though significant gains can be made [81] compared to the commercial detector used here). A promising alternative method uses structured light fields to reject the symmetric part of the detection beam that contains most of the optical power and none of the particle's position information [89]. No matter how it is reached, shot noise defines a fundamental noise floor that can only be surpassed by using a squeezed light source [90, 91].

The noise due to the detection electronics alone is called *dark noise*. The noise due to the detection electronics and the laser system is called *bright noise*. In Figure 3.7 we plot examples of the dark and bright voltage noise power spectral densities for our system. The spectra are computed from $N = 2^{24} \approx 8.4 \times 10^6$ points sampled at $f_\mathrm{s} = 25\,\mathrm{MHz}$ (full range input $\pm 500\,\mathrm{mV}$) for a total record time of $T_\mathrm{r} = 336\,\mathrm{ms}$ and averaged over 30 independent records. The spectral resolution with these acquisition settings is approximately 3 Hz. While the origin and decomposition of the observed noise can be challenging to determine, certain features may be quantified.

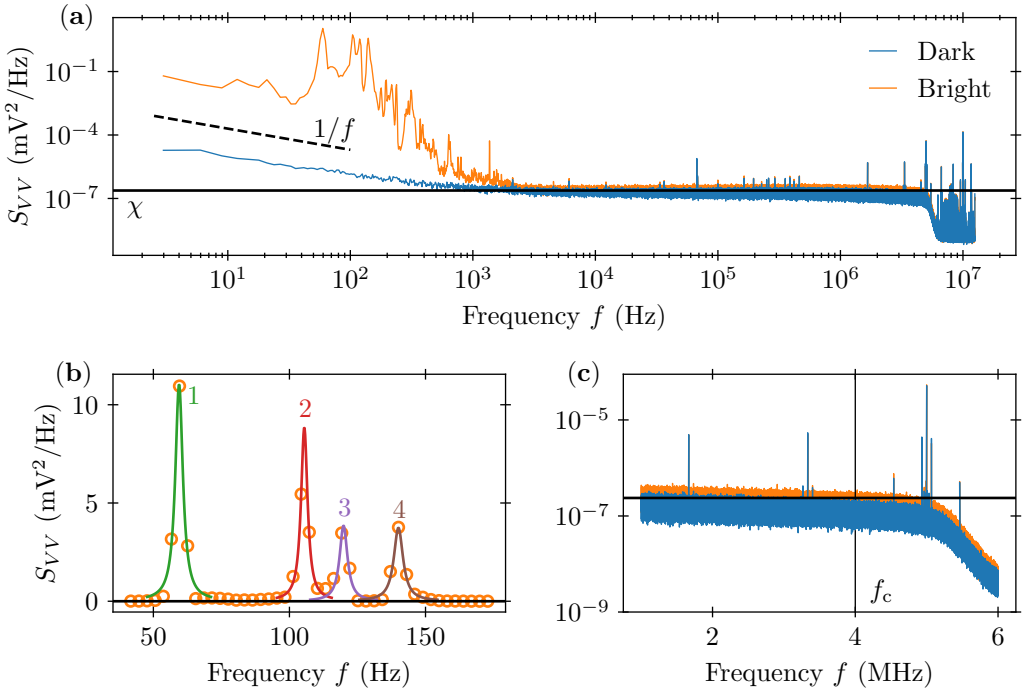

Figure 3.7: Voltage power spectral densities for dark (blue) and bright (orange) noise. (**a**) The full spectra on log-log-scale axes. The black dashed line depicts $1/f$ scaling and the solid black line depicts the bright-noise floor (computed as the average value between 500 kHz and 1.5 MHz and shown on all panels). (**b**) A zoom of the low-frequency bright noise plotted on linear-scale axes. The open symbols are the same data as in (**a**) and the solid lines are Lorentzian fits and numbered according to the fit parameters in Table 3.2. (**c**) A zoom of the high-frequency noise. The vertical line marks the anti-aliasing filter cutoff frequency f_c.

At the lowest observed frequencies, both bright and dark spectra scale as $\sim f^{-1}$. This so-called *one-over-f noise* or *flicker noise* is typical of most measurement systems across disciplines [92]. Near the 100 Hz-scale, the bright noise is dominated by broad resonances with frequencies that correspond to power-line harmonics and audible acoustics. These peaks are reasonably well fit (simultaneously) by a sum of four Lorentzian line shapes

$$S_{VV}(f) = \sum_{i=1}^{4} A_i \frac{\Gamma_i^2}{(f - f_{0,i})^2 + \Gamma_i^2} \,. \tag{3.3}$$

The fit values for each peak's amplitude A_i resonant frequency $f_{0,i}$ and width Γ_i are reported in Table 3.2. We find the details of these peaks can change over time. For example, we often observe an additional peak near 237 Hz that is not seen in Figure 3.7. The 237 Hz peak seems to originate from the building's chilled water pipes.

High-frequency noise is predominantly flat and interspersed with several additional resonances. The high-frequency resonances are electrical in nature and the noise floor is due to a combination of quantization noise, shot noise, and any remaining high-frequency classical laser noise or detector noise. A very simple noise model treats the observed noise spectrum as white and with a magnitude given by the average high-frequency noise floor, denoted χ. The bright noise floor ($\chi \approx 2.4 \times 10^{-7}\,\mathrm{mV^2/Hz}$) is only slightly higher than the detector noise floor suggesting the shot-noise-limit may be within reach at high frequencies. At frequencies above the anti-aliasing filter's cut-off frequency f_c and below the Nyquist frequency $f_\mathrm{s}/2$, a lower noise floor is observed. This is

Table 3.2: Results of un-weighted non-linear least-squares fitting of Equation (3.3) to the low frequency bright noise data. Such fitting methods are questionable for spectra obtained as average-periodograms (See Section 2.2.4). The results and uncertainties reported here are as given by Scipy's `curve_fit` that incorrectly assumes Gaussian-distributed data. Nonetheless, the fit results provide a convenient and easy way to quantify the observed low-frequency noise without detailed modeling.

Peak i	A_i ($\mathrm{mV}^2/\mathrm{Hz}$)	$f_{0,i}$ (Hz)	Γ_i (Hz)
1	11.1 ± 0.3	59.4 ± 0.1	1.7 ± 0.1
2	8.9 ± 2.2	105.1 ± 0.1	1.4 ± 0.3
3	3.9 ± 0.7	119.9 ± 0.3	1.7 ± 0.4
4	3.7 ± 0.3	140.0 ± 0.3	2.1 ± 0.2

essentially the noise due to the digitizer, excluding the laser and detector noise. As will be done in Chapter 4, care must be taken to analyze experimental data in a bandwidth where neither the bright noise's low-frequency resonances nor high-frequency floor significantly pollute the recorded signal.

3.2 Microspheres

In this section, we will provide a few details on the microspheres used in this work. We will also discuss our method for releasing single microspheres in the vicinity of the optical trap.

3.2.1 Microsphere geometry

The silica microspheres we use were purchased with a nominal diameter of 3.17 µm (Bangs Laboratories SSD5001). They are manufactured using the *Stöber process* [93] that is known to produce highly mono-dispersed and

spherical particles. We quantitatively assess our microspheres' geometry by imaging a sample of them with scanning electron microscopy. Image analysis reveals the size and shape distributions of the sample. An example image is shown in Figure 3.8 (**a**).

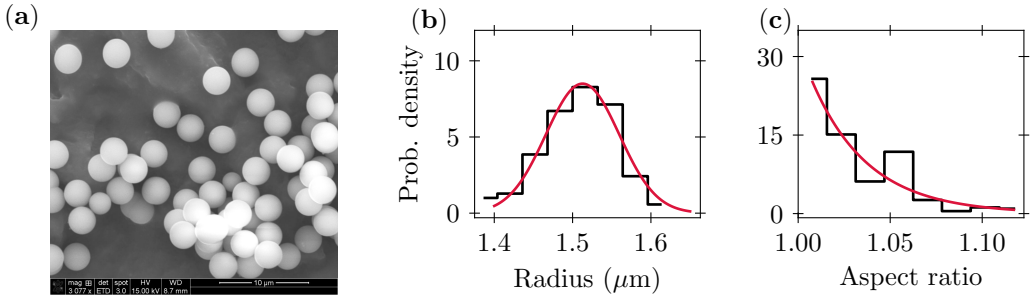

Figure 3.8: Silica microspheres and their geometry. (**a**) An example scanning electron microscope image. (**b**) The probability density (black steps) and a Gaussian fit (red line) of radius measurements made by analyzing 10 images like that shown in (**a**). (**c**) The probability density (black steps) and an exponential fit (red line) of aspect ratio measurements.

We measured the radius of the imaged spheres using the Particle Sizer plugin [50] for the Fiji distribution of ImageJ, an open-source image analysis software. We operated the plugin with default settings and in "single particle mode" to exclude touching and overlapping microspheres. Once an image was analyzed, we manually excluded false positives by inspection. In total, we measured 219 spheres and fit the histogram of measured radii to a one-dimensional Gaussian probability density. Figure 3.8 (**b**) depicts the histogram and its fit. The fitting procedure yields the sample mean $\mu_R = 1.511\,\mu\text{m}$ and standard deviation $\sigma_R = 0.044\,\mu\text{m}$. Hence the relative uncertainty in the microsphere size is $\sigma_R/\mu_R = 2.9\%$. Our measurement provides a marked

improvement over the manufacturer-stated relative uncertainty of 10%. The measured radius is slightly smaller than the manufacturer's claimed radius of 1.585 µm.

Using similar image analysis techniques, we also measure the aspect ratio $a/b \geq 1$ of the microspheres. The probability distribution of the measured aspect ratios and its fit to an exponential distribution is shown in Figure 3.8 (**c**). From the fit, we find the mean of $\epsilon = a/b - 1$ is $\mu_\epsilon = 0.028$. At this level of asphericity, corrections [94] to the Stokes drag $\gamma_0 = 6\pi\eta R$ are below 1% and therefore ignorable compared to the uncertainty in R.

While the Stöber process does indeed produce highly spherical and mono-dispersed microspheres, their density can vary significantly. In Chapter 4 we will describe our Brownian-motion-based method for determining a trapped microsphere's density for inertial mass sensing. For now, we move on to describe our method for releasing microspheres.

3.2.2 Launching single microspheres with ultrasonic vibration

The silica glass microspheres we purchase are delivered as a dry powder. As is apparent in Figure 3.8 (**a**), the microspheres tend to form clusters. They also adhere to a silica glass coverslip when pressed. The force required to separate two adhered microspheres is $F_{\text{sphere}-\text{sphere}} = 2\pi CR$ where the material-specific constant C is called the *effective solid surface energy* [95]. Separating two 1 µm-diameter silica spheres takes about 88 nN [96], so we estimate $C \approx 28\,\text{nN}/\mu\text{m}$. Separating a sphere from a flat surface requires twice

as much force [95]: $F_{\mathrm{flat-sphere}} = 4\pi CR$, or $\sim 176\,\mathrm{nN}$ for a 1 µm-diameter silica sphere on a silica substrate. Thus we conclude that releasing microspheres from a glass coverslip very likely releases single microspheres since it takes about twice as much force to separate them from the substrate than from each other. Accelerating a microsphere-coated coverslip at $a = F_{\mathrm{flat-sphere}}/m \propto R^{-2}$, where m is the mass of the microsphere, should release single microspheres into the air. For a 1 µm-diameter silica sphere the required acceleration is immense: $a \approx 1.8 \times 10^8\,\mathrm{m/s^2}$.

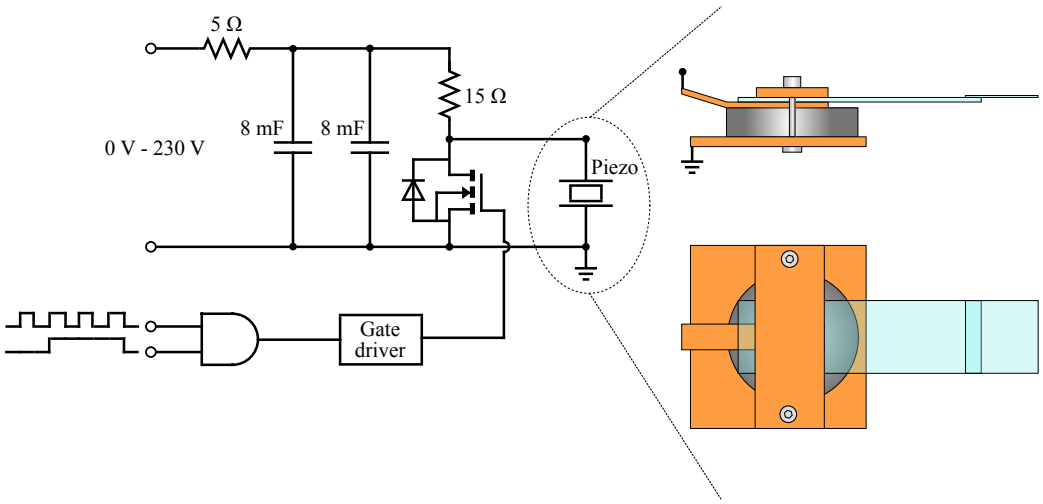

Figure 3.9: Schematic circuit used to generate high power pulses. Also shown is a rendering of the piezo element and clamping system from the top (upper rendering) and side (lower rendering). The body of the clamp is made of copper and is electrically grounded to the pulse generator. The positive terminal is constructed from a flat copper wire that is isolated from the clamp body by the glass slide. A number 2 coverslip dosed with microspheres is epoxied to the end of the glass slide.

Our system for launching microspheres is depicted schematically in Figure 3.9. The system relies on a resonantly driven piezoelectric element (piezo, APC International 70-2221) clamped to a glass slide with a microsphere-coated cover slip epoxied to its end. The purpose of the cover slip is to increase the oscillation amplitude and therefore increase the acceleration. The piezo manufacturer claims a high resonant frequency of $\sim$344 kHz. The displacement — and hence acceleration — of the piezo is proportional to the voltage across it. When driven on resonance the electrical-to-mechanical coupling is maximized and therefore so is the acceleration.

We measured the small-signal acceleration of the microsphere launching system using a laser Doppler vibrometer (Polytec PSV-500). In this experiment, the drive frequency is chirped from DC to 1 MHz while the vibrometer measures the acceleration of the coverslip. The ratio of the acceleration's spectrum to the drive-chirp spectrum, shown in Figure 3.10, identifies a peak acceleration of $7 \times 10^4\,(\mathrm{m/s^2})/\mathrm{V}$ at a resonant frequency of 348 kHz. By using a chirp, high spectral resolution is achieved, but only $\sim$16 mV is applied per frequency bin and for insufficient time for the oscillations to reach steady-state. The steady-state acceleration is likely higher by about a factor of 10 [97].

On resonance, the piezo's impedance reduces to just a few Ohms. Therefore, high voltage resonant drive demands high current. To meet these demands we operate a custom-built high-power pulse generator [98], also shown in Figure 3.9. In the high-power pulse circuit, two large capacitors (8 mF, Digikey 338-1236-ND) store an electric charge that can be delivered to the piezo.

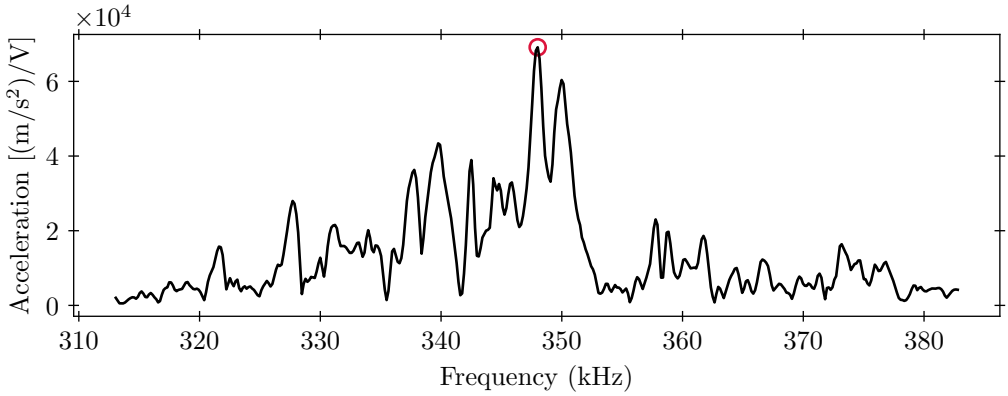

Figure 3.10: Ultrasonic microsphere launching system's small-signal acceleration, measured near the center of the coverslip using a laser Doppler vibrometer. The red circle marks the peak acceleration.

The capacitors are maintained at a constant voltage using a supply of up to 300 V (TDK Lambda 300-5). A high-power metal–oxide–semiconductor field-effect transistor (MOSFET, Vishay IRFPS40N50L) switches the current on and off at the frequency set by a square wave function generator (Stanford Research Systems DS345). A pulse generator gates the function generator so that high-power pulses of a known duration can be applied on demand. Since the MOSFET has a large input capacitance (8110 pF), we must drive its gate with a high-power, high-speed gate driver (Microchip TC4422).

The ability of the system to release microspheres depends on several control parameters like the capacitor charging voltage, the oscillation frequency, and the oscillation duration. In practice, we find that highly efficient release of microspheres can be achieved for a variety of control parameters. A typical sequence for a freshly-dosed cover slip is as follows. First, at a low volt-

age of 5 V to 20 V and a duration set to a large value of 100 ms, several pulses are delivered at frequencies ranging from 342 kHz to 348 kHz. These initial pulses serve to break up small clumps of microspheres and also shake off large clumps that are only weakly bound to the cover slip. Then, to attempt to release and trap microspheres, we reduce the pulse length to 10 ms and slowly increase the voltage until a stream of microspheres visibly falls through the HeNe laser, as seen by the naked eye or the imaging camera, typically between 30 V to 60 V. At this point, we find it helpful to drift through the parameter space of drive frequency and pulse duration until either a microsphere is trapped or microspheres no longer appear to be releasing. In the case of the latter, the drive voltage is increased. It can also be helpful to slightly reposition the coverslip with respect to the trap or tighten the screws clamping the glass slide to the piezo. If the system is well aligned, we find roughly 1 in 10 trapping attempts succeed.

The apparatus described here for launching microspheres is essentially the same as that built in our group nearly a decade ago [98] and another recently investigated in more detail [97]. Launching microspheres with diameters less than one micrometer via ultrasonic vibration may be achieved by using a polytetrafluoroethylene-coated glass slide [99]. An alternative method uses laser-induced acoustic desorption [100]. In this method, a laser pulse is focused onto the back side of a metal substrate whose front side is dosed with microspheres. The sudden absorption of optical energy sources a shockwave in the substrate that can launch the microspheres. We use similar methods

to generate acoustic impulses that are detected in the microsphere's motion. Moving toward our acoustic detection results, we next describe the various acoustic sensors and sources used in our experiment.

3.3 Acoustic sensors and sources

One of the primary results of this work is to measure acoustic fields by monitoring the movements of an optically trapped microsphere. Our acoustic detection methodology will be covered in detail in Section 4.2. There, we will use two types of sound sources and two types of acoustic detectors to validate our microsphere-based measurements. This section specifies the technical details of these sources and detectors.

3.3.1 Microphone and Microflown

In Section 2.3.4 we saw how the conservation of mass and energy in a fluid lead wave solutions in the fluid's velocity and pressure. Therefore, an instrument sensitive to a fluid's pressure or velocity could be used to detect sound waves. We use both types of detectors for the following reasons. Owing to the microsphere's small size and hence small inertia, its motion is sensitive to high-frequency sound waves. The highest-bandwidth commercially available acoustic detectors measure pressure. On the other hand, our microsphere is primarily sensitive to acoustic velocity, not pressure, but acoustic velocity sensors are not commercially available at high bandwidth. Therefore, we will compare the results of our microsphere-based acoustic sensor to both a high-

bandwidth pressure microphone and a calibrated acoustic velocity sensor.

A familiar pressure-sensitive instrument is a microphone. Most microphones operate under the same working principle: A small (millimeter to centimeter scale) cavity is sealed with a tight membrane, setting the cavity's internal pressure. When a sound wave's pressure field changes the external pressure, the membrane flexes in response. Measuring the membrane's deflection, usually by electrical means, provides a signal linearly-related to the sound pressure. Usually, a small hole in the backside of the cavity allows the pressure differential to equalize over time scales long compared to any acoustic signals of interest. Such venting lower-bounds the microphone's measurement bandwidth.

A microphone's *sensitivity* is the ratio of the output voltage to the input acoustic pressure. A membrane has many intricate vibrational modes that can make the sensitivity a complicated function of frequency. The bandwidth of a microphone is typically upper-bound by the membrane's first resonant frequency so that the sensitivity is constant or slowly varying with frequency. High-quality microphones are amplified so that the sensitivity is as constant as possible. Inevitably, higher bandwidth microphones are smaller and under more tension so that the first resonant frequency is high. High tension comes with a trade-off of low sensitivity since a tighter membrane must be driven harder to achieve the same displacement as a looser membrane. Additionally, microphones are either *free-field*-type or *pressure*-type. A free-field microphone is calibrated so that it measures the acoustic pressure field as if

the microphone was not present. A pressure-type microphone measures the actual acoustic pressure on the membrane.

In our measurements, we use a state-of-the-art high-bandwidth (calibration range 10 Hz to 200 kHz) pressure microphone (GRAS 46DE with 12BA power module). The entire sensor, including the preamplifier, is less than 1/8-inch in diameter, making it the smallest measurement microphone set in the world [101]. Figure 3.11 shows our microphone's sensitivity curve $s_p(f)$ as provided by the manufacturer, including their corrections for free-field conditions at normal incidence and the protective grid removed. A pistonphone calibration unit (GRAS 42AG) provides a standardized way to set the sensitivity at a single sound level and frequency since the sensitivity may change slightly with environmental conditions like temperature and humidity. The frequency-dependent sensitivity can then be re-scaled to match the one-point measurement provided by the pistonphone. We have never measured a sensitivity different from the manufacturer-stated value of 0.68 mV/Pa at 250 Hz.

Contrary to microphones the *Microflown*[2] detects the velocity wave of an acoustic field [102, 103]. The Microflown operates on the principle of hot-wire anemometry. In the Microflown, two nanometer-scale platinum wires are fixed parallel to one another and separated laterally by a couple of microns. Both wires are driven with current such that their temperature is approxi-

[2]Sometimes *microflown* is used as a generic name for a velocity-sensitive acoustic sensor. We choose to refer to the instrument as a proper noun because its inventors started the company called Microflown Technologies and sell the Microflown as a product.

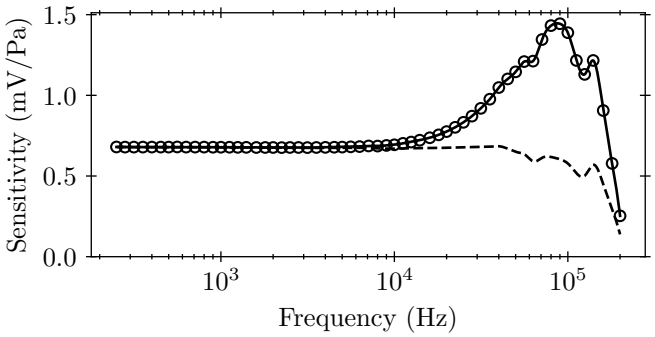

Figure 3.11: Microphone sensitivity $s_p(f)$ for frequencies from 250 Hz to 200 kHz. The open circles are the data points provided by the manufacturer and the solid line is our cubic interpolation of the data that enables evaluation of the sensitivity at arbitrary frequencies. The dashed line shows the cubic interpolation of the sensitivity without the manufacturer-provided corrections for free-field, protective-grid-removed conditions.

mately 500 K. In the absence of flow, both wires have the same temperature. When air flows across the wires, advection imbalances their temperature by an amount proportional to the flow speed. Accurately measuring the temperature imbalance is possible due to the highly temperature-dependent resistance of platinum. Though the velocity-sensitive wires are themselves small, the unit is housed in a 1/2-inch diameter package, making it somewhat bulky compared to our microphone. The high-frequency sensitivity of the Microflown is limited by diffusive heat transfer between the wires as well as their finite heat capacities. At low frequencies, the sensitivity is limited by thermal-boundary-layer and packaging effects [104].

The Microflown is calibrated up to 20 kHz by the manufacturer by

fitting their sensitivity measurements to

$$g(f) = \frac{g_0}{\sqrt{1 + f_1^2/f^2}\sqrt{1 + f^2/f_2^2}\sqrt{1 + f^2/f_3^2}\sqrt{1 + f_4^2/f^2}}\,, \tag{3.4}$$

$$\psi(f) = \arctan\left(\frac{C_1}{f}\right) - \arctan\left(\frac{f}{C_2}\right) - \arctan\left(\frac{f}{C_3}\right) + \arctan\left(\frac{C_4}{f}\right)\,, \tag{3.5}$$

where $g(f)$ is the sensitivity amplitude and $\psi(f)$ is the sensitivity phase. The complex sensitivity is $s_u(f) = g(f)e^{i\psi(f)}$. Table 3.3 reports the fit values for g_0, f_i and C_i, $i = 1, 2, 3, 4$. Figure 3.12 plots the amplitude and phase of the sensitivity over the calibration range.

Table 3.3: Our Microflown sensitivity fitting parameters provided by the manufacturer

Quantity	Value	Unit
g_0	11.4	V/(m/s)
f_1	22	Hz
f_2	595	Hz
f_3	5 456	Hz
f_4	142	Hz
C_1	16	Hz
C_2	570	Hz
C_3	22 551	Hz
C_4	142	Hz

To make calibrated acoustic measurements with either available sensor, one may record a voltage signal $V(t)$ and then filter the result in post-processing according to the relevant sensitivity $s(f)$. Introducing the notation $\mathcal{F}(\cdot)$ for the Fourier transform and $\mathcal{F}^{-1}(\cdot)$ for its inverse, the signal in physical units $x(t)$ is

$$x(t) = \mathcal{F}^{-1}\left\{\frac{\mathcal{F}[V(t)]}{s_x(f)}\right\}\,, \tag{3.6}$$

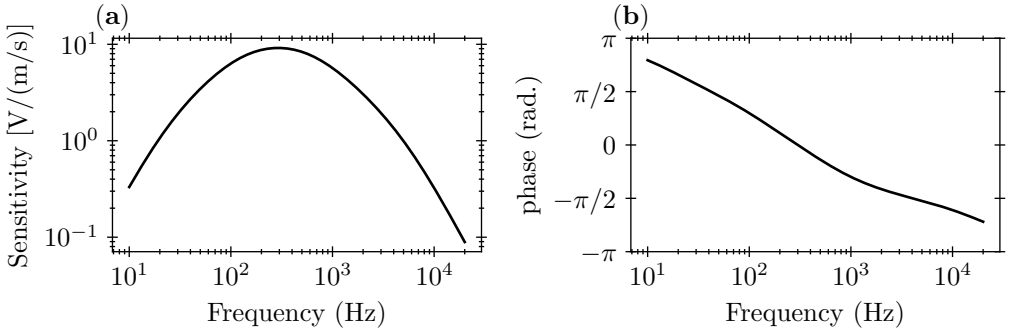

Figure 3.12: Our Microflown's sensitivity (**a**) amplitude and (**b**) phase.

where $x = p$ corresponds to a pressure measurement with the microphone and $x = u$ corresponds to a velocity measurement with the Microflown. To evaluate Equation (3.6), one must know the sensitivity $s_x(f)$ at the frequencies corresponding discrete Fourier transform $\tilde{x}_k = \tilde{x}(f_k)$. This is possible through the Microflown's fitting functions (3.4) and (3.5) and the microphone's interpolating function (plotted in Figure 3.11). Since we only know the sensitivity for frequencies $f > 0$ and the measured signal is purely real-valued, we use the one-sided Fourier transform (Scipy's `rfft` and `irfft`) to evaluate Equation (3.6).

3.3.2 Piezoelectric speakers and laser ablation

This Section details the devices used to generate sound to test our microsphere as an acoustic sensor. We use two piezoelectric speakers and laser ablation.

One of the piezo speakers has a resonant frequency of 40 kHz (Mu-

rata MA40S4S). For a given drive voltage, the sound pressure generated by the speaker falls off by about 20 dB re 20 µP per 5 kHz of detuning from resonance. The second piezo speaker has a resonant frequency of 4 kHz (TDK PS1240P02BT). The frequency response of the 4 kHz piezo is more intricate, exhibiting a sharp drop below resonance and additional peaks above resonance. For example, the sound pressure at 3 kHz is approximately 35 dB re 20 µP below that of resonance, the sound pressure at 10 kHz is only 20 dB re 20 µP below that of resonance[3]. Both speakers are driven directly by a computer-controlled function generator (Agilent 33250A). The LabView control loop enables the application of pure tones or tone bursts at voltages of up to 10 Vp − p. Tone bursts may be delayed with respect to the acquisition trigger.

The optical setup used for laser ablation, described in Section 3.1, provides a source of sharp acoustic pulses. A pulsed laser focused to a small spot on an interface or within a medium can deposit a vast amount of energy in a short amount of time. This phenomenon has myriad technical applications from micro-machining [105] to laser-induced-breakdown spectroscopy [106] as well as more general studies of light-plasma interactions [107]. Even within the sub-field of pulsed-laser acoustics, the literature spans numerous applications like non-contact damage detection [108], medical imaging [109], and scale-modeling of sonic booms [110]. As an acoustic source, at least two regimes are present depending on the laser's pulse energy. At lower energies, in the

[3]The frequency response characteristics reported here were estimated from the corresponding product data-sheet.

thermo-elastic regime, the sudden deposition of heat causes a rapid increase in temperature and therefore expansion, leading to an acoustic wave [111]. At higher energies, in the *ablative* regime, solid substrates may be vaporized leading to a sudden ejection of mass that sources a shock wave [112]. A shock wave is a non-linear fluid phenomenon[4] in which highly compressed zones travel faster than the bulk medium's sound speed while the rarefied zones travel slower. Unlike linear acoustics, the different travel speeds at different points on a shock wave's profile lead to distortion and a rapid loss of amplitude [114]. We operate our system in the ablative regime to generate sound pulses with high-frequency content.

Our LabView control program communicates with our pulsed laser in two ways. RS-232 serial communication is used to issue commands and read responses in between acquisitions. Commands may be issued, for example, to set the flash lamp energy (and hence the pulse energy), set the internal-trigger repetition rate, or read the system's temperature. When enabled, the program will automatically warm up the laser to a desired operating point (around 39 °C) by operating at a high energy and repetition rate. Alternatively, digital pulses for the flash lamp and Q-switch may be sent to trigger laser pulses on demand and at a well-defined time with respect to an acquisition.

[4]Non-linearities in fluids are often thought of as the velocity advection term in the Navier–Stokes equations. Here the non-linearity arises from how a medium's comprehensibility depends on its pressure [113]

Chapter 4

Results

We come now to a description of the experiments undertaken with the apparatus described in Chapter 3 and using the tools developed in Chapter 2. The results are organized into two major sections each with differing viewpoints on Brownian motion and each undertaken with slightly different methodologies.

In Section 4.1 we report the results of a measurement campaign devoted to determining the mass of an optically trapped microsphere. These results have been published in [115] under the title *Weighing an optically trapped microsphere in thermal equilibrium with air*. In [115], the statistical properties of Brownian motion are leveraged to deduce the trapped microsphere's mass in three ways. To compare the methods fairly, and to compare ours to alternative methods from the literature, much effort is expended on careful characterization and error analysis. We find that measuring the instantaneous velocity variance provides an accurate and precise mass measurement using a fraction of the data required by alternative methods.

In Section 4.2 the perspective is shifted. Here, we measure the microsphere's motion when subjected to a sound field. Many approximations are

made to deduce the sound field in proper physical units. Despite the relative simplicity of our analysis techniques, adequate agreement with traditional sensors is observed within the limits of their sensitivity and bandwidth. We then take a step beyond traditional sensors and attempt to measure sound fields with the frequency content outside their bandwidth. Again, it is the microsphere's velocity degree of freedom that enables our measurements.

In the inertial mass sensing experiment, Brownian motion is the signal while in acoustic detection, it is noise. In both cases, the (essentially) white thermal noise spectral density is filtered by the microsphere's inertia. At angular frequencies beyond the inverse momentum relaxation time $2\pi f > \tau_{\mathrm{p}}^{-1}$, velocity fluctuations decay as f^{-2} [See Equation (2.130)]. In the case of acoustic detection, it is true that the microsphere's inertia also reduces its mechanical responsivity at high frequencies. However, acoustic waves at high frequencies are necessarily high energy: If a medium oscillates with an amplitude d at angular frequency $2\pi f$, its kinetic energy scales as f^2.

We turn now to a discussion of the weighing results. Much of the prose is adapted from [115], but all the data and figures have been recompiled for the present document.

4.1 Trap calibration and inertial mass sensing

Optical trapping of nano- and micro-scale objects [12, 21] has become a paradigmatic tool in diverse fields, from micro-manipulation of biological samples [20, 22, 116–124] to center-of-mass cooling experiments [34, 125, 126]

aiming to observe macroscopic quantum effects [127–131], to metrology experiments [132–134] with optomechanical sensing applications [135–139].

Many such applications must monitor the trapped particle's position as a function of time, so a position-sensitive detector must be calibrated. We have estimated our split-beam detector's calibration constant in Section 3.1.2, but in practice, one must measure the calibration factor for each experiment. Such measurement-based calibration usually requires knowledge of the trapped particle's mass [132]. However, silica nano and microspheres, often the object of study in levitated optomechanics experiments, do not have a readily-known mass. Indeed, the Stöber process used to manufacture these particles [93] yields very spherical results with a low dispersion of radius, as demonstrated in Section 3.2, but their mass density can vary by over 20% [140, 141][1]. Calculated with these values, the uncertainty in mass is about 22%. For this reason, recent work has focused on mass metrology of nano and microspheres optically trapped in vacuum using methods of electrostatic levitation [141], oscillation [133], and trapping potential nonlinearities [134], and, most recently a drop-recapture method performed in air [142]. The mass uncertainty achieved in each of these experiments is at the level of one to a few percent. Each has unique advantages like no assumptions on particle geometry, and distinct challenges, e.g., control of the particle's charge, accurate modeling of local potentials (gravitational, electric, or optical), or vacuum capabilities including

[1]The mass density variation is due to pores in the microspheres, so the actual density is lower than that of bulk silica.

feedback cooling.

Here, we demonstrate a mass metrology experiment with uncertainty similar to previous work but performed on a 1.5 µm radius silica microsphere optically trapped in air [143] at room temperature and pressure. Our experiment employs a dual-beam optical trap [12,144], described in detail in Chapter 3. Our system remains in thermal equilibrium at all times making for a simple protocol. Moreover, we explore two distinct methodologies leveraging our detector's high spatiotemporal resolution. First, in our *spectral method*, we fit an average voltage signal power spectral density to simultaneously extract parameters that make no assumptions on the physical conditions of the experiment. We then fix conditions known with high accuracy — the air temperature T, air viscosity η, and particle radius R — to compute the harmonic trap strength κ, microsphere mass density ρ, and detector calibration factor β, as well as the uncertainties and correlations of these parameters. The microsphere mass is similarly calculated by combining fitting and fixed parameters.

In the second *equipartition method*, we compute the voltage signal and voltage-derivative signal variances from which we deduce the particle mass in two additional ways. Doing so requires a detector with sufficient resolution to observe the particle's instantaneous velocity, pioneered in [34, 81]. The equipartition methods additionally require knowledge of either the harmonic trap strength κ or calibration factor β which must be determined via the spectral method first. The spectral method demands a high volume of data to sufficiently smooth the experimental power spectral densities and is in that

sense slow. The equipartition methods, once an initial spectral calibration is performed, require 10× shorter data traces to achieve similar uncertainty in subsequent mass measurements.

All the data presented in this section were collected while monitoring a single trapped microsphere. To check for systematic bias in our method, we have recorded data at 14 different trapping laser powers $P = P_{\mathrm{F}} + P_{\mathrm{B}}$ where P_{F} is the power of the forward beam and P_{B} is the power of the backward beam. The ratio $P_{\mathrm{F}}/P_{\mathrm{B}} = 0.8 \pm 0.1$ is held approximately constant. P ranges from 4.8 mW to 257 mW. At each power, we collect $n = 40$ records of the voltage signal, each $T_{\mathrm{r}} = 84\,\mathrm{ms}$ long, at a sampling rate of $f_{\mathrm{s}} = 50\,\mathrm{MHz}$ and full-scale input of $\pm 1\,\mathrm{V}$. In post-processing, the signals are low-pass filtered by bin-averaging averaging together non-overlapping blocks of $M = 256$ samples for improved spatial resolution [Equation (2.52)]. The new effective sampling rate is 195 kHz. We compute the experimental voltage power spectral density $\hat{S}_{VV,k} = \hat{S}_{VV}(f_k)$ using Bartlett's method [Equation (2.89)]. Now let us see how voltage power spectral densities may be used to characterize our system.

In what follows, we first rigorously characterize our system in Section 4.1.1. Then, the mass measurement techniques are described in Section 4.1, followed by a discussion of the results in Section 4.1.3.

4.1.1 Power spectral density parameter estimation

In thermal equilibrium, the position power spectral density of the microsphere's motion is given by Equation (2.129). On the other hand, the detec-

tor's voltage signal $V(t)$ is related to the microsphere's position $x(t)$ through Equation (3.1) as $V(t) = \beta x(t)$. Therefore, the (one-sided) theoretical voltage power spectral density is

$$S_{VV}(\omega) = \beta^2 \frac{4k_{\mathrm{B}}T\gamma_0}{(m\omega^2 - \kappa)^2 + \gamma_0^2\omega^2}\,. \tag{4.1}$$

Once a set of trials is collected, we fit the experimental data $\hat{S}_{VV}$ to the model

$$S_{VV}(f;\boldsymbol{\theta}) = \frac{1}{a + bf^2 + cf^4}\,, \tag{4.2}$$

wherein we have defined the column vector of free parameters $\boldsymbol{\theta} = (a, b, c)^{\mathrm{T}}$. The fit is performed using the maximum likelihood estimation method [145–147], as described in Section 2.2.4. In fact, the minimization of the negative-log-likelihood $\ell(\hat{S}_{VV};\boldsymbol{\theta})$ [Equation (2.93)] with respect to $\boldsymbol{\theta}$ can be very accurately approximated analytically and implemented numerically [146], thereby providing good start values for the minimization.

In the end, the minimization provides the best fit parameters $\hat{\boldsymbol{\theta}} = (\hat{a}, \hat{b}, \hat{c})^{\mathrm{T}}$ that maximize the likelihood of the data given the model: $\mathcal{L}(\hat{S}_{VV};\boldsymbol{\theta}) = \exp\left[-\ell(\boldsymbol{\theta}, \hat{S}_{VV})\right]$. In Figure 4.1 (**a**) we show experimental power spectral densities and their best-fit curve for two different trapping laser powers. In Figure 4.1 (**b**) we consider the data-to-fit ratio's probability distribution and compare it to the expected unit-mean Erlong distribution, provided by re-scaling Equating (2.91),

$$\mathcal{P}_{\hat{S}_{VV}/S_{VV}}(z) = \frac{n^n}{(n-1)!} z^{n-1} e^{-nz}\,. \tag{4.3}$$

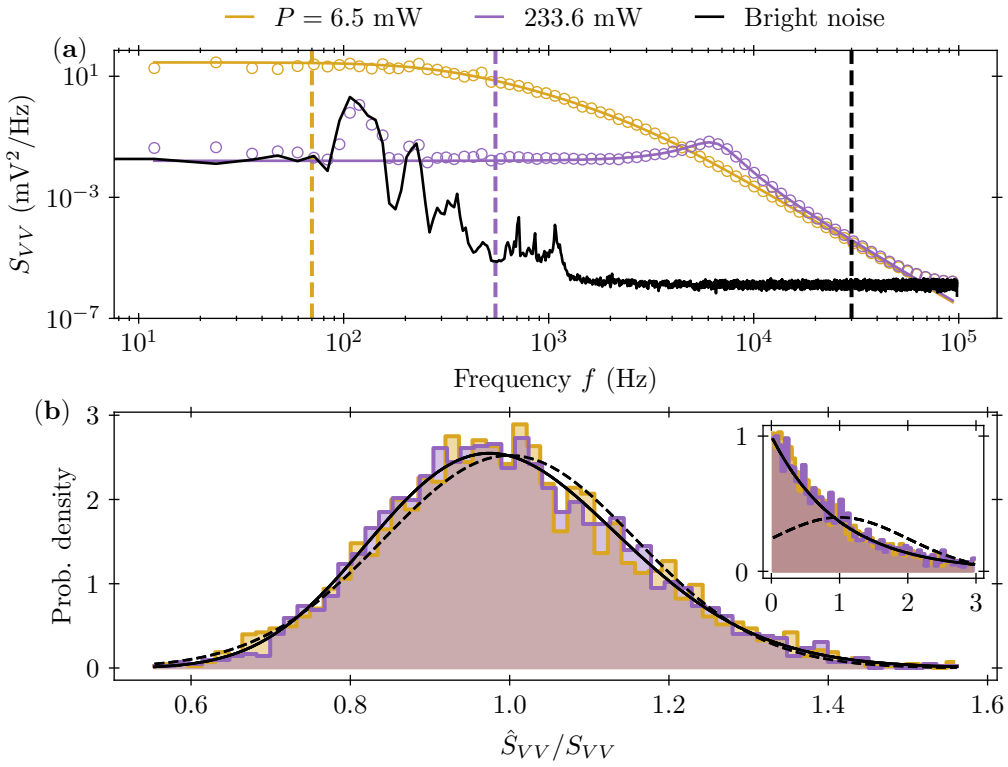

Figure 4.1: (**a**) Example voltage power spectral densities (open symbols, averaged over geometrically-spaced frequency bins for visualization purposes) and their fits (solid lines) for high (purple) and low (gold) trapping laser powers. The vertical dashed lines represent the upper (black, shared) and lower (color-coded by trap power) frequency bounds used for the fits. The solid black line shows the bright noise of the detection system with no frequency-bin averaging. (**b**) The probability density of the ratio between the data and fit from (**a**) (filled histograms). The solid black line corresponds to the universally-expected Erlong distribution. The dashed black line corresponds to a Gaussian distribution with the same variance $1/n$ as the Erlong distribution, where $n = 40$ is the number of averaged experimental spectra. The inset shows the same ratio but when the fit is performed after only $n = 1$ spectral average and the Erlong distribution reduces to the exponential distribution.

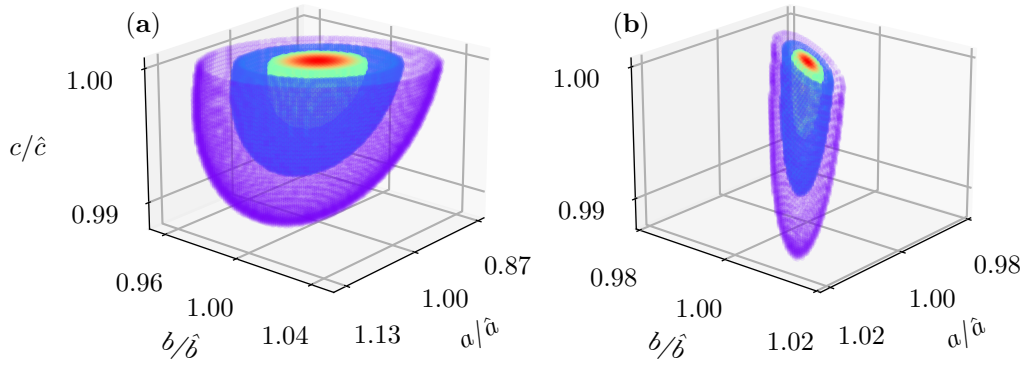

Figure 4.2: Visualizing the likelihood $\mathcal{L}$ for (**a**) low (6.1 mW) and (**b**) high (234 mW) trapping laser powers. For this visualization, we plot isosurfaces taken at Gaussian widths of 3-sigma (purple), 2-sigma (blue), and a core from the maximum likelihood (red) to the 1-sigma-width (green). Further, we have cut the data cloud in half to better visualize the isosurfaces. The quality and quantity of parameter correlations appear to depend on the trapping laser power.

As n increases, the distribution becomes more Gaussian-like, but a non-Gaussian bias remains clear even for $n = 40$.

To measure the fitting parameter's uncertainty and correlation, and inspired by the *profile likelihood* method [145,147], we scan $\boldsymbol{\theta}$ in the vicinity of $\hat{\boldsymbol{\theta}}$ over a volume of parameter space to build up a three-variate distribution $\mathcal{L}$. Figure 4.2 visualizes example results of such a parameter scan. The parameter scans may be fit to a three-variate Gaussian distribution

$$\mathcal{P}_{\mathrm{G}}(\boldsymbol{\theta}; \hat{\boldsymbol{\theta}}, \boldsymbol{\Sigma}_{\boldsymbol{\theta}}) = \exp\left[-\frac{1}{2}(\boldsymbol{\theta} - \hat{\boldsymbol{\theta}})^{\mathrm{T}} \boldsymbol{\Sigma}_{\boldsymbol{\theta}}^{-1} (\boldsymbol{\theta} - \hat{\boldsymbol{\theta}})\right] . \tag{4.4}$$

The vector $\hat{\boldsymbol{\theta}}$ resulting from the fit is taken as the best-fit parameter set. The matrix $\boldsymbol{\Sigma}_{\boldsymbol{\theta}}$ resulting from the fit provides the variance-covariance matrix of the

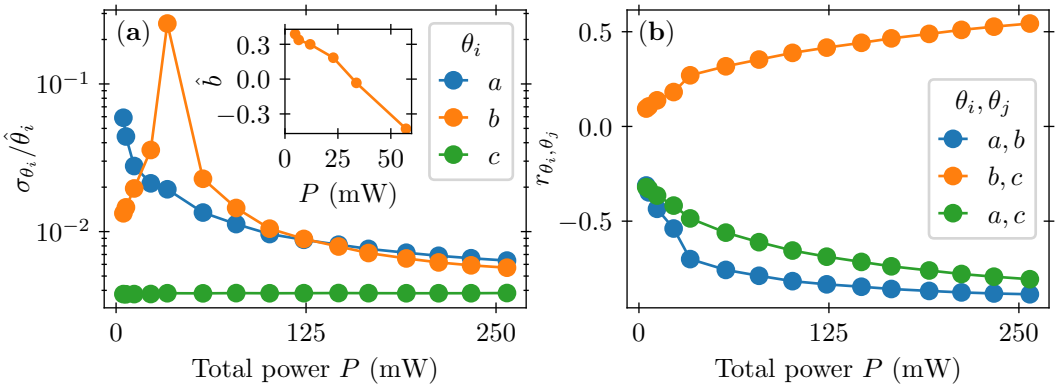

Figure 4.3: (**a**) The relative uncertainty in parameter θ_i found at each trapping laser power. The divergence observed for $\sigma_b/\hat{b}$ near $P = 25\,\mathrm{mW}$ is due to the zero crossing seen in the inset. (**b**) Correlations among the power spectral density fitting parameters.

fitted parameters:

$$\boldsymbol{\Sigma}_{\boldsymbol{\theta}} = \begin{pmatrix} \sigma_a^2 & \sigma_{ab}^2 & \sigma_{ac}^2 \\ \sigma_{ab}^2 & \sigma_b^2 & \sigma_{bc}^2 \\ \sigma_{ac}^2 & \sigma_{bc}^2 & \sigma_c^2 \end{pmatrix}.$$

The uncertainty in parameter θ_i is $\sigma_{\theta_i} = ([\Sigma_{\boldsymbol{\theta}}]_{i,i})^{1/2}$ for $i \in \{1, 2, 3\}$ and the correlation coefficient between parameters θ_i and θ_j is $r_{\theta_i,\theta_j} = [\Sigma_{\boldsymbol{\theta}}]_{i,j}/(\sigma_{\theta_i}\sigma_{\theta_i})$, for $i \neq j \in \{1, 2, 3\}$. Figure 4.3 visualizes the relative uncertainties and correlations found for $\boldsymbol{\theta} = (a, b, c)^{\mathrm{T}}$ at each trapping laser power.

The fitting parameters $\boldsymbol{\theta}$ may be used to deduce a more physical set of parameters: trap strength κ, microsphere density ρ, and calibration constant β. Each of the physical parameters $\boldsymbol{\Theta} = (k, \rho, \beta)^{\mathrm{T}}$ are functions of the fitting parameters $\boldsymbol{\theta}$ and constant parameters R, T, and η. That is, $\boldsymbol{\Theta} = \boldsymbol{\Theta}(\boldsymbol{\phi})$, where we have defined the vector of independent variables $\boldsymbol{\phi} = (\boldsymbol{\theta}, R, \eta, T)^{\mathrm{T}}$.

For explicit formulae, we find

$$k(\boldsymbol{\phi}) = 12\pi^2\eta R\sqrt{\frac{a}{b+2\sqrt{ac}}}\,, \tag{4.5}$$

$$\rho(\boldsymbol{\phi}) = \frac{9\eta}{4\pi R^2}\sqrt{\frac{c}{b+2\sqrt{ac}}}\,, \tag{4.6}$$

$$\beta(\boldsymbol{\phi}) = \sqrt{\frac{6\pi^3\eta R}{k_{\mathrm{B}}T}}\frac{1}{\sqrt{b+2\sqrt{ac}}}\,. \tag{4.7}$$

The set of fixed parameters was chosen to propagate the least uncertainty to the physical parameters. As already discussed, R is known to within a few percent. The temperature may be easily measured with sub-Kelvin accuracy so the uncertainty in T is mostly due to fluctuations in temperature during an acquisition. Across the entire collection campaign, the temperature varied by less than 0.8 K. The viscosity of air is primarily temperature dependent [148], exhibiting a relatively weak $\sim T^{1/2}$ scaling. Further corrections for relative humidity, taken as a constant 50% throughout the collection campaign, slightly improve the theoretical accuracy of η to less than 0.1% [2] [149]. A large swing of 50% relative humidity changes η by less than 1% while a swing of 1 K in temperature changes η by even less.

In light of the above uncertainty considerations, the variance-covariance matrix of the independent variables may be approximated in the block-diagonal form $\boldsymbol{\Sigma}_{\boldsymbol{\phi}} = \mathrm{diag}(\boldsymbol{\Sigma}_{\theta}, \sigma_R^2, \sigma_\eta^2, \sigma_T^2)$ where we have estimated $\sigma_\eta = 0.18\,\mu\mathrm{Pa\,s}$ and

[2] In our original publication [115], only temperature dependence was accounted for. We now have humidity sensors so that we may refine the set value of viscosity for each experiment. Retroactively analyzing the published data including effects of typically-observed humidity negligibly changes the published results.

$\sigma_T = 0.8\,\mathrm{K}$. Relative uncertainty in R ($\sim 3\%$) dominates that of T ($\sim 0.3\%$) and η ($\sim 1\%$). The block diagonal form assumes measurement correlation exists only between the fitted parameters. Then, the variance-covariance matrix of the physical parameters in terms of the fitting and constant parameters is given by the error propagation equation [150]

$$\boldsymbol{\Sigma}_{\boldsymbol{\Theta}} = \boldsymbol{J}_{\boldsymbol{\Theta}} \boldsymbol{\Sigma}_{\boldsymbol{\phi}} \boldsymbol{J}_{\boldsymbol{\Theta}}^{\mathrm{T}} \,. \tag{4.8}$$

By definition, the Jacobian matrix evaluated at the optimal fitting parameters is $(J_{\boldsymbol{\Theta}})_{i,j} = [\partial \Theta_i / \partial \phi_j]_{\boldsymbol{\theta}=\hat{\boldsymbol{\theta}}}$. Further defining

$$u_1 = \frac{3}{16\pi^3 R^3}\,, \quad u_2 = \frac{1}{2\sqrt{6\pi\eta R k_{\mathrm{B}} T}}\,, \tag{4.9}$$

$$d_1 = b + 2\sqrt{ac}\,, \quad d_2 = b + 2\sqrt{ac}\,, \tag{4.10}$$

lets us express the Jacobian as

$$\frac{\partial \boldsymbol{\Theta}}{\partial \boldsymbol{\phi}} = \frac{6\pi^2 \eta R}{\sqrt{a d_2^3}} \times \begin{pmatrix} d_1 & -a & -\sqrt{a^3/c} & 2ad_2/R & 2ad_2/\eta & 0 \\ -u_1 c & -u_1\sqrt{ac} & u_1 d_1 \sqrt{a/c} & -4u_1 d_2 \sqrt{ac}/R & 2u_1 d_2 \sqrt{ac}/\eta & 0 \\ -u_2\sqrt{c} & -u_2\sqrt{a} & -u_2 a/\sqrt{c} & u_2 d_2 \sqrt{a}/R & u_2 d_2 \sqrt{a}/\eta & -u_2 d_2 \sqrt{a}/T \end{pmatrix}. \tag{4.11}$$

The square root of the diagonal entries of Equation (4.8) are then our best estimate for the uncertainty in physical parameters $\boldsymbol{\Theta} = (\kappa, \rho, \beta)^{\mathrm{T}}$. In Figure 4.4 we plot the best-fit parameters with error bars. As expected, the trap strength [Figure 4.4 (**a**)] scales linearly with the total trapping laser power. Fitting a straight line provides the scaling $\kappa/P \approx 0.18\,(\mathrm{fN/nm})/\mathrm{mW}$. The

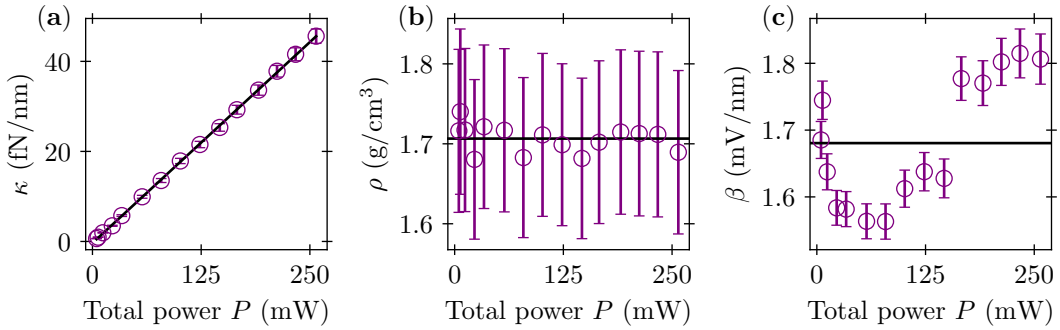

Figure 4.4: (**a**) Trap strength, (**b**) microsphere density, and (**c**) detector calibration constant deduced by voltage power spectral density fits. In (**a**), the solid black line is a linear fit. In (**b**) and (**c**) the solid black line marks the mean value over all trapping laser powers.

microsphere density ρ [Figure 4.4 (**b**)] is independent of power within the measurement's uncertainty.

On the other hand, the calibration factor β [Figure 4.4 (**c**)] shows a clear non-monotonic trend with trapping laser power. One might expect heating effects at higher laser powers could explain β's trend, but our result's non-monotonicity makes such an explanation unlikely. Indeed, the calibration factor and the temperature both primarily scale the overall power spectral density (4.1) multiplicatively without changing its shape (except for effects due to viscosity's temperature dependence). Thus, we conclude heating of the microsphere due to the laser is inconsequential because of the strong environmental coupling. This is not the case for experiments in vacuum [151]. Moreover, we find the observed trend in β is reproducible when the power-scan experiment is repeated with different microspheres, suggesting the source β's variation could be slight beam deviations caused by the half-wave-plate-

polarizing- beam-splitter pairs used to control the trapping and detected powers. Such beam deviations could change the geometric factor entering the theoretical prediction for β [Equation (3.1)]. Nonetheless, we see our rough estimate $\beta \approx 2.5\,\mathrm{mV/nm}$ is accurate within a factor of 2, which is quite an acceptable agreement considering the estimate relied on simple dimensional arguments.

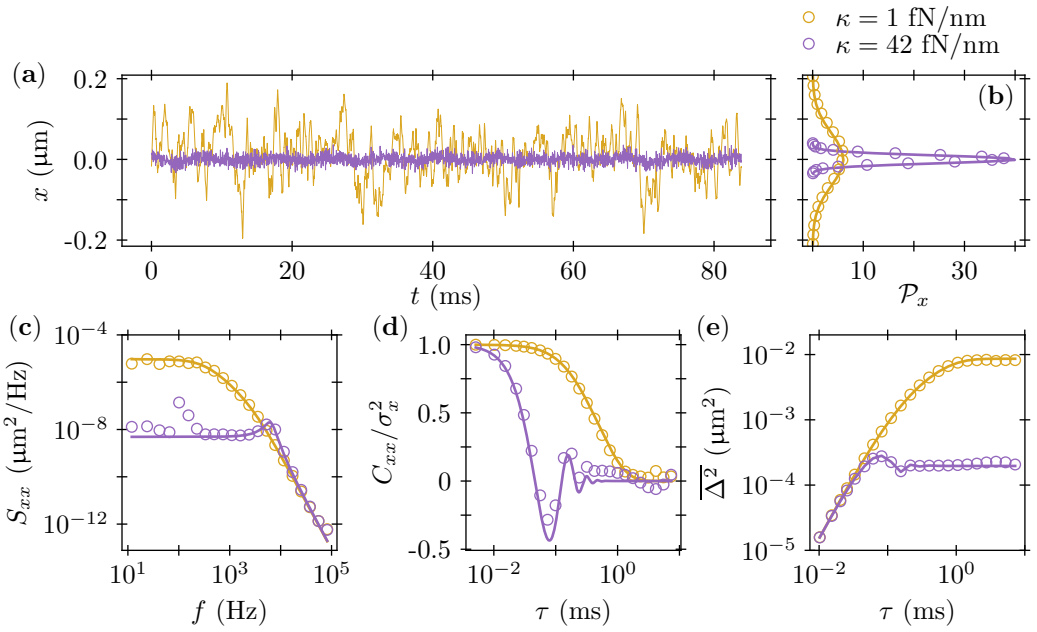

Figure 4.5: (**a**) The position of a silica microsphere undergoing Brownian motion subject weak ($\kappa = 2\,\mathrm{fN/nm}$, gold) and strong ($\kappa = 44\,\mathrm{fN/nm}$, purple) harmonic confinement. The experimental results (open symbols) and theoretical predictions (solid curves) are shown for the (**b**) position probability density, (**c**) position power spectral density, (**d**) normalized position autocorrelation function, and (**e**) mean squared displacement.

As a further cross-check of our results, we can also compute the other statistical quantities defined in Section 2.3.3. Figure 4.5 shows the position

statistics of experimentally-observed Brownian motion, in analogy to the simulation data shown in Figure 2.10. Results are shown for the same high and low trapping laser powers as in 4.3. Similarly, the velocity statistics are shown in Figure 4.6.

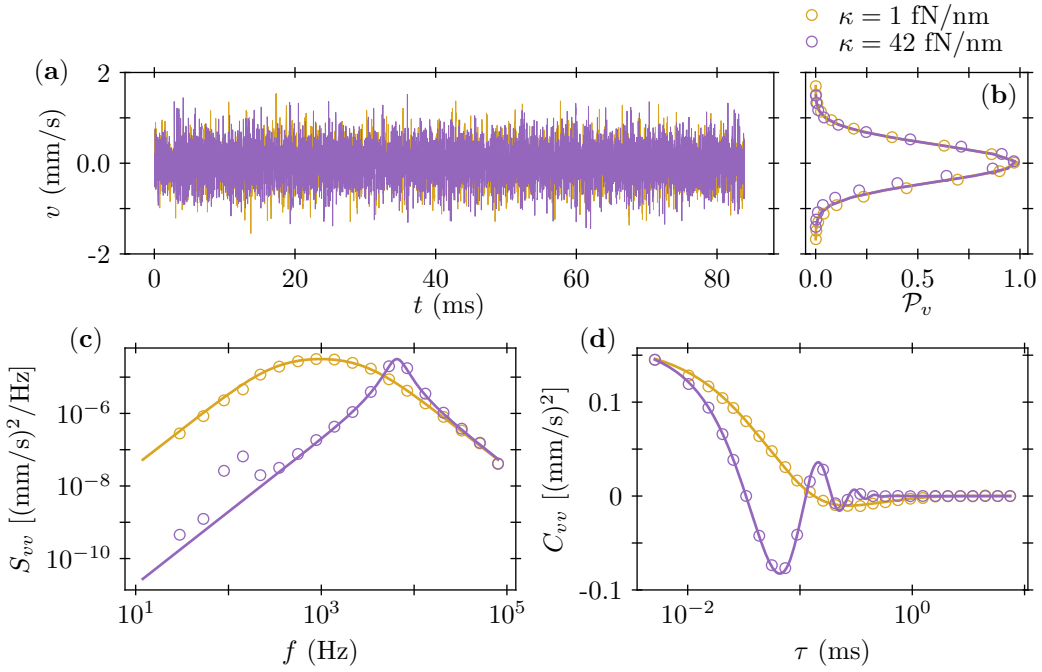

Figure 4.6: (**a**) The velocity of a silica microsphere undergoing Brownian motion subject weak ($\kappa = 2\,\mathrm{fN/nm}$, gold) and strong ($\kappa = 44\,\mathrm{fN/nm}$, purple) harmonic confinement. The experimental results (open symbols) and theoretical predictions (solid curves) are shown for the (**b**) velocity probability density, (**c**) velocity power spectral density, and (**d**) velocity autocorrelation function.

We observe excellent agreement between the data and corresponding theoretical predictions upon characterizing our system through power spectral density analysis. The velocity statistics are better predicted than the position

statistics because the troublesome low-frequency noise does not as significantly pollute the velocity data. Figure 4.6 (**c**) clearly shows the velocity variance due to Brownian motion is larger than the variance due to noise near the 100 Hz band. Meanwhile Figure 4.5) (**c**) shows the variance due to low-frequency noise is comparable to that of Brownian motion near the 100 Hz band. Herein lies the power of spectral analysis: we conveniently remove the effect of low-frequency noise in the voltage signal by setting the frequency bounds of the fit, as exemplified in Figure 4.3.

We have now established how to characterize an optically trapped microsphere through analysis of the detector's voltage power spectral density. We next leverage our well-characterized system to measure the mass of the optically trapped microsphere in three ways.

4.1.2 Mass measurements

Upon learning power spectral density fitting parameters, it is straightforward to estimate the mass using the density and radius of the microsphere as $m_1 = 4\pi\rho R^3/3$. However, the equipartition theorem, $k_{\mathrm{B}}T = m\sigma_{\dot{x}}^2 = \kappa\sigma_x^2$, provides two additional possibilities: $m_2 = k_{\mathrm{B}}T/\sigma_{\dot{x}}^2$ and $m_3 = \kappa\sigma_x^2/\sigma_{\dot{x}}^2$ Explicitly, the three mass measurements $\mathbf{m} = (m_1, m_2, m_3)^{\mathrm{T}}$ written in terms of the

augmented independent variables $\boldsymbol{\phi}' = (a, b, c, \sigma_{\dot{V}}^2, \sigma_V^2, R, \eta)^{\mathrm{T}}$ read

$$m_1(\boldsymbol{\phi}') = 3\eta R\sqrt{\frac{c}{b + 2\sqrt{ac}}}\,, \tag{4.12}$$

$$m_2(\boldsymbol{\phi}') = 6\pi^3\eta R\frac{1}{\sigma_{\dot{V}}^2(b + 2\sqrt{ac})}\,, \tag{4.13}$$

$$m_3(\boldsymbol{\phi}') = 2\pi^2\eta R\frac{\sigma_V^2}{\sigma_{\dot{V}}^2}\sqrt{\frac{a}{b + 2\sqrt{ac}}}\,. \tag{4.14}$$

All three measurements are independent of temperature T.

The benefit of m_2 and m_3 is that, once a power spectral density fit calibrates the system, further data can be collected to estimate the variances $\sigma_{\dot{V}}^2$ and σ_V^2, which may be used to update the mass measurement if it changes with time. Of course, there is nothing to update if the mass is unchanging like in our power-scan experiment. Nonetheless, to make use of methods m_2 or m_3, we must make an adequate estimate of the variances. We deduce a signal's variance by creating a histogram of its mean-subtracted values and least-squares fitting a Gaussian distribution (2.86) with variance as the only free parameter. Figure 4.7 (**a**)-(**b**) shows the position and velocity (proportional to V and $\dot{V}$, respectively) histogram fits for signals of length $\tau = 0.3\,\mathrm{s}$ (i.e. 4 of the 40 available records) at both high and low trapping laser powers.

The uncertainty in voltage and voltage-derivative variances must be quantified and propagated to m_2 and m_3. The systematic uncertainty due to digitization is negligible compared to that caused by noise in the system. Hence, for error propagation, we take a statistical approach to measuring the systematic uncertainty. In particular, we take the histogram fit's covariance

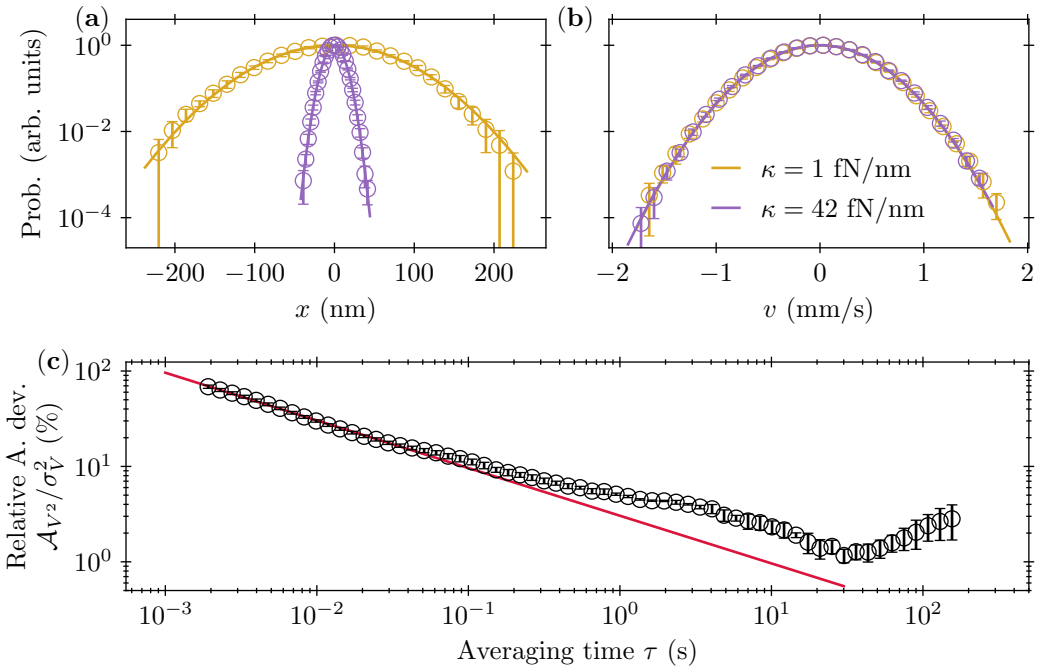

Figure 4.7: (**a**) Position histogram (open circles) computed from 0.3 s of data for weak (gold) and strong (purple) traps and shown on semi-logarithmic axes. Error bars reflect the standard deviation across 10 trials. The solid lines are Gaussian fits with variance as the only free parameter. (**b**) As in (**a**) but for the velocity degree of freedom. (**c**) relative Allan deviation stability analysis. Error bars reflect the standard deviation across three trials. The red line marks the thermally-limited trend $\tau^{-1/2}$.

matrix added in quadrature with the fluctuations observed across 10 trials per trapping power. Note this is a slight abuse of the distinction between systematic and statistical uncertainty. For this study we use "statistical" uncertainty for fluctuations observed in parameters across trapping laser powers and "systematic" uncertainty for the values used in error propagation at each laser power.

How much data should be used to compute the variance? For an uncorrelated voltage signal of length τ, the uncertainty in estimating its variance scales as $\tau^{-1/2}$, which is a thermally-limited trend. However, at short times ($\tau < \tau_{\mathrm{p}}$), the data are correlated due to the microsphere's ballistic dynamics. At long times, slow drifts in the system tend to pollute the signal's variance. One way to quantify the optimal amount of data to use for computing the variance is the Allan-deviation stability analysis [60, 61, 132, 138].

The Allan deviation is the square root of the Allan variance, Equation (2.60). For a variance stability analysis, we compute the relative Allan deviation of V^2 as $\mathcal{A}_{V^2}(\tau)/\sigma^2_{V,\mathrm{opt}}$. Intuitively, the relative Allan deviation measures the variability in variance measurements from signals of length τ compared to the variance $\sigma^2_{V,\mathrm{opt}}$ found using a signal of optimal length, i.e. the variance of a length-τ_0 signal where τ_0 is the Allan-minimum averaging time.

Figure 4.7 (**c**) shows the results of our Allan deviation experiment, performed three times at 22.8 mW of trapping laser power. This test was performed with the same microsphere as the power-scan experiment but with a much lower sampling rate of $f_{\mathrm{s}} = 20\,\mathrm{kHz}$. The low sampling rate allows for long

($T_{\mathrm{rec}} = 14\,\mathrm{m}$) records within the limitations of the digitizer's onboard memory. On the downside, such a low sampling rate prohibits us from computing the voltage derivative signal. However, within the harmonic-trap approximation, the Allan-minimum averaging time should be identical for the voltage variance and the voltage-derivative variance [132]. According to our Allan deviation analysis, the system is stable out to about 30 s, so using 0.3 s of data for estimating the variances allows for 100 independent mass measurements before the slow drifts demand re-calibration of the apparatus. It is in this sense that methods m_2 and m_3 are faster than m_1.

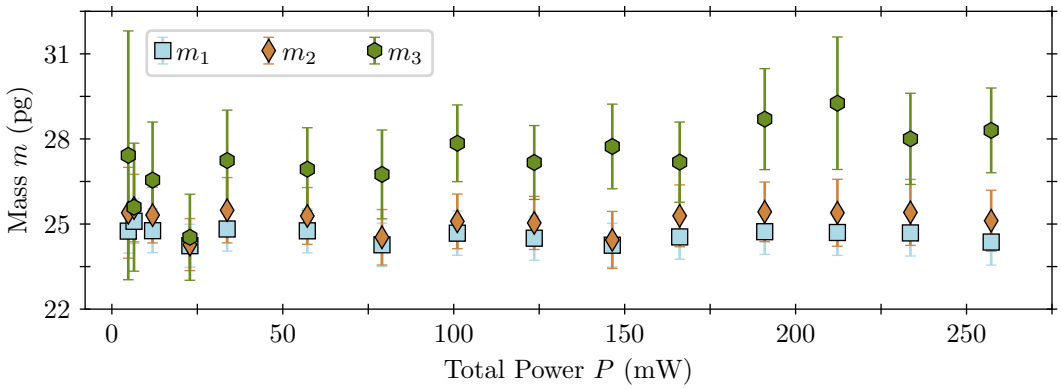

Figure 4.8: Comparing our three methods for inertial mass sensing.

In Figure 4.8 we show the results of our three mass measurement procedures. We find $\mu_{m_1} = 24.6\,\mathrm{pg}$, $\mu_{m_2} = 25.1\,\mathrm{pg}$, and $\mu_{m_3} = 27.3\,\mathrm{pg}$ where the mean values μ are taken over the 14 experiments at different total trapping laser powers. Reported error bars are calculated from the power spectral density fit's covariance matrix and uncertainties in both variances and fixed parameters $\boldsymbol{\Sigma}_{\boldsymbol{\phi}'} = \mathrm{diag}(\boldsymbol{\Sigma}_{\boldsymbol{\theta}}, \sigma^2_{\sigma^2_V}, \sigma^2_{\sigma^2_{\dot{V}}}, \sigma^2_R, \sigma^2_\eta)$. Specifically, error bars for the

mass measurements are given by the square root of the diagonal entries of $\mathbf{\Sigma_m}$ where

$$\mathbf{\Sigma_m} = \boldsymbol{J}_\mathbf{m} \mathbf{\Sigma}_{\boldsymbol{\phi}'} \boldsymbol{J}_\mathbf{m}^{\mathrm{T}}\,, \tag{4.15}$$

and the mass-measurement Jacobian is

$$\frac{\partial \mathbf{m}}{\boldsymbol{\phi}'} = \frac{6\pi^2 \eta R}{\sqrt{a d_2^3}} \times \begin{pmatrix} -v_1 c & -v_1\sqrt{ac} & v_1 d_1 \sqrt{a/c} & 0 & 0 & v_1 d_2 \sqrt{ac}/R & 2v_1 d_2 \sqrt{ac}/\eta \\ -v_2\sqrt{c/d_2} & -v_2\sqrt{a/d_2} & -v_2 a/\sqrt{c d_2} & -v_2\sqrt{a d_2}/\sigma_{\dot{V}}^2 & 0 & v_2\sqrt{a d_2}/R & v_2\sqrt{a d_2}/\eta \\ v_3 d_1 & -v_3 a & -v_3\sqrt{a^3/c} & -2v_3 a d_2/\sigma_{\dot{V}}^2 & 2v_3 a d_2/\sigma_V^2 & 2v_3 a d_2/R & 2v_3 a d_2/\eta \end{pmatrix}, \tag{4.16}$$

for which we have defined

$$v_1 = \frac{1}{4\pi^2}\,, \quad v_2 = \frac{\pi}{\sigma_{\dot{V}}^2}\,, \quad v_3 = \frac{\sigma_V^2}{\sigma_{\dot{V}}^2}\,. \tag{4.17}$$

As mentioned above, we refer to such error bars as systematic uncertainty, denoted $\sigma_{m_i}^{\mathrm{sys.}}$, $i = 1, 2, 3$. The statistical uncertainty (or fluctuation), denoted $\sigma_{m_i}^{\mathrm{stat.}}$, is calculated as standard deviation across the 14 experiments. Measurement m_1 has the smallest relative error bars (3.2% when averaged over the 14 experiments) and the smallest relative statistical uncertainty (0.9%). Measurement m_2, which supplements the power spectral density analysis by estimating the voltage-derivative variance in the time domain, agrees well with m_1, albeit with average relative error bars at 4.3% and relative statistical fluctuations at 1.6%. The benefit of m_2 is that, once an initial power spectral density analysis is performed, parameters like mass (or temperature) can be subsequently updated 10 times faster than collecting data for additional m_1 measurements. Measurement m_3 has the largest systematic and statistical

relative uncertainties, 6.8% and 4.2% respectively. Furthermore, method m_3 displays an additional systematic error in that it deviates from m_1 and m_2 by nearly 10%. The bias in m_3 may be traced to the excess time-domain variance originating from the noise in the $\sim 100\,\mathrm{Hz} \pm 70\,\mathrm{Hz}$ band.

For comparison, the mass according to the manufacturer values of density $\rho_{\mathrm{Bangs}} = 2.0\ \mathrm{g/cm^3}$ ($\sigma_{\rho_{\mathrm{Bangs}}}/\rho_{\mathrm{Bangs}} = 20\%$) and our radius measurement $R = 1.51\,\mu\mathrm{m}$, ($\sigma_R/R = 2.9\%$) is $m_{\mathrm{Bangs}} = 28.8\,\mathrm{pg}$ with an uncertainty of 22%, which agrees with all our mass measurements within the uncertainty tolerance, despite the discrepancy in mean values.

4.1.3 Discussion

A recent experimental effort [133] measured the mass of $R = 0.143\,\mu\mathrm{m}$ silica spheres, optically trapped in vacuum, to be 4.01 fg with 2.8% uncertainty using 40 s of position data. Their oscillating electric field method does not assume any particular particle shape or density, though a density of 2.2 $\mathrm{g/cm^3}$ agrees with their measurements. In [141], a 2.6 µm radius sphere is optically trapped and levitated with a static electric field as the trapping laser power is reduced, resulting in a mass measurement of 84 pg with 1.8% uncertainty using 42 minutes of data. The density is also measured to be 1.55 $\mathrm{g/cm^3}$ with 5.2% uncertainty. A third strategy used in [134] stabilizes oscillations of a 0.082 µm radius sphere in the nonlinear-trapping regime to deduce the detector calibration constant with 1.0% uncertainty and a mass of 3.63 fg with 2.2% uncertainty. Finally, very recent work [142] used a drop-recapture

method and camera-based detection with a time resolution that could not quite resolve the microsphere's instantaneous velocity. Fitting position autocorrelation functions, they measure their resin particle's radius to be 2.3 µm with 4.3% statistical uncertainty. In the drop-recapture experiments, 90 s worth of trials are used to deduce a mass of 55.8 pg with 1.4% statistical uncertainty and 13% systematic uncertainty. The authors combine the radius and mass measurements to deduce a density of 1.1 g/cm^3 with 9.1% statistical uncertainty.

As a comparison, we present a summary of our inertial mass sensing parameter values and uncertainties in Table 4.1. Based entirely on thermal equilibrium analysis, our two most accurate mass estimates have uncertainties of 3% to 4% as compared to the 1% to 2% uncertainty in vacuum-dependent and 13% in the air-based, nonequilibrium methods. Further, all of our measurements are made with significantly shorter position data traces: Our spectral method m_1 used a total of 3 s of position data while our equipartition methods m_2 and m_3 used 0.3 s of position data. Interestingly, our density measurement has comparable accuracy to the recent body of work using silica particles, all of which sourced particles from the same manufacturer. The variability and apparent radius dependence of measured density values underscore the parameter's uncertainty inherent to the manufacturing process.

Most of the existing mass sensing methods have been demonstrated in a high vacuum environment where the experimental goals center around ground-state cooling or exceptionally sensitive force transduction. Addition-

ally, the existing methods rely on forces external to the trap, often driving the system out of equilibrium and limiting their utility as environmental sensors. Our method has the advantages of speed in that between 10× and 100× less data are required compared to other methods; environmental coupling, which unlocks future sensing applications; and simplicity in that no additional experimental setup is required beyond trapping and monitoring.

Disadvantages include the requirements of environmental coupling, enough spatiotemporal resolution to resolve the instantaneous velocity, and accurate knowledge of the particle's radius and medium's viscosity. While an advantage for future applications, environmental coupling critically limits the heating effects of the trapping laser and enables fast equilibration with the environment, so our method could face complications in vacuum-based experiments. Instantaneous velocity resolution enables our fastest measurement, m_2, but can be much more difficult in a liquid environment, though certainly possible [81,89]. The trapped particle's geometry was quantified statistically in our experiment, but less uniform samples could significantly alter the error analysis. In such cases, in situ measurements of the trapped particle with optical microscopy, light scattering, or autocorrelation function analysis could improve the error budget. Finally, knowledge of the air's viscosity is quite reliable. On the other hand, a liquid's viscosity is more sensitive to temperature changes, and additives like glucose used in biophysics experiments or sodium chloride used in Casimir force measurements [152] can introduce additional uncertainties.

Error analysis and comparison to equilibrium Brownian motion theory

Table 4.1: Table of values and uncertainties. Reported values are the average over the power scan experiment, except for κ and σ_V^2 for which we report the range since these quantities scale with P. Also reported are the relative systematic uncertainties (sys.) averaged over the power scan experiment and the statistical uncertainties (stat.) that express the relative standard deviation over the power scan, where applicable. For κ, the reported statistical uncertainty is the average relative residual with respect to the linear fit shown in Figure 4.4 (**a**).

Quantity	**Value**	**Uncertainty** (%)		**Unit**
		sys.	stat.	
R	1.51	2.9	-	µm
η	18.172	0.1	0.03	µPa s
T	295.50	0.3	0.05	K
$\sigma_{\dot{V}}^2$	0.46	2.3	-	$\mathrm{mV^2/\mu s^2}$
σ_V^2	$(3.29 \times 10^{-4}, 0.02)$	5.3	-	$\mathrm{V^2}$
κ	(0.64, 45.6)	3.4	2.4	fN/nm
ρ	1.71	6.0	1.0	$\mathrm{g/cm^3}$
β	1.68	1.8	5.5	mV/nm
m_1	24.6	3.2	0.9	pg
m_2	25.1	4.3	1.6	pg
m_3	27.3	6.8	4.2	pg

has elevated our optical trapping apparatus to a well-characterized tool for environmental sensing applications. In the next section, we take a step toward demonstrating such environmental sensing by testing our system as an acoustic detector.

4.2 Acoustic sensing

Several properties make optically trapped microspheres attractive detectors: They are small, easily perturbed, and hence locally sensitive; they are mechanically un-tethered; their position may be monitored with high spatiotemporal resolution; and their operation is feasible in vacuum, gaseous, and liquid environments. Several experiments have demonstrated the power of optically-trapped-microsphere-based detection schemes including kinesin molecule stepping [153], zeptonewton force sensing [136], state-of-the-art torque sensitivity [154], absolute pressure and gaseous species identification [155], ultra-fast viscosity measurements [89], Casimer force measurements [152], and searches for new physics [156], including proposals to measure high-frequency gravity waves [157]. There have also been many demonstrations of optically trapped microspheres used to measure low-frequency fluid flows [158–163].

In what follows, we describe and demonstrate a new sensing modality for optical tweezers: acoustic detection. To this end, the remainder of this Section is divided into three Subsections. First, in 4.2.1 we define the instrument's sensitivity and predict the magnitude of minimum-detectable signals. Second, in 4.2.2 we validate our device by measuring tone bursts and compar-

ing results with state-of-the-art commercially-available transducers. Third, in 4.2.3 we look beyond the bandwidth of the traditional sensors by measuring impulsive sounds generated through laser ablation. Finally, in 4.2.4 we discuss our results in the context of the most-similar work performed to date.

4.2.1 Calibration and predicted performance

Recall from Section 4.1.1 that the position calibration factor β, relating the detector voltage and microsphere position through $V(t)/x(t) = \beta$, may be accurately determined through spectral density analysis. Additionally, recall from Section 2.3.4 the transfer function $H(\omega) = \tilde{v}(\omega)/\tilde{u}(\omega)$ [Equation (2.148)] relating the complex harmonic (Fourier) amplitude of the microsphere's velocity $\tilde{v}(\omega)$ to that of an external flow's $\tilde{u}(\omega)$. Since $\tilde{v}(\omega) = -i\omega\tilde{x}(\omega)$, we have a straightforward estimate for the sensitivity of our system to external flow fields

$$s'_u(\omega) = \frac{-i\beta H(\omega)}{\omega}\,. \tag{4.18}$$

Assuming plane-wave acoustic fields such that $p/u = Z_0$, we may measure acoustic pressures using the sensitivity

$$s'_p(\omega) = s'_u(\omega)/Z_0\,. \tag{4.19}$$

The prime on s' distinguishes the sensitivity of our microsphere-based system from that of the microphone s_p and the Microflown s_u, defined in Section 3.3.1. Figure 4.9 compares the magnitude-sensitivities of our traditional acoustic detectors to that of our microsphere. We see that $|s'_p| > |s_p|$ except for a region near 150 kHz and that $|s'_u| > |s_u|$ for all frequencies.

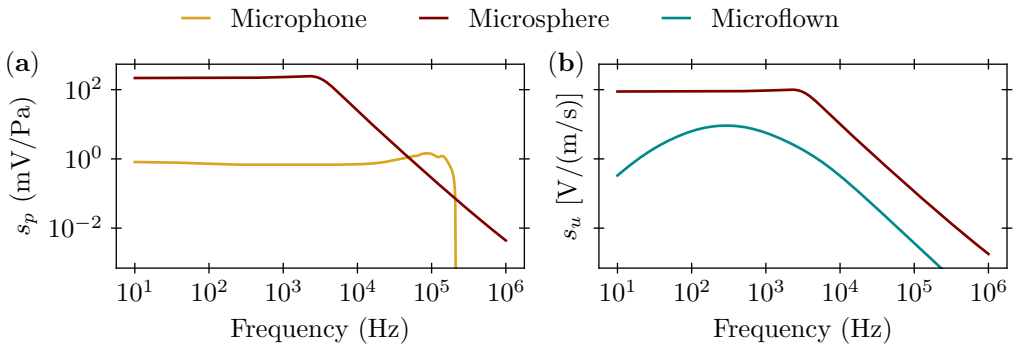

Figure 4.9: Comparing the acoustic-detection sensitivity of our microsphere system to (**a**) our pressure microphone, including free-field and protective-grid-removed corrections and (**b**) our Microflown. For this visualization we have set $R = 1.5\,\mu\text{m}$, $\kappa = 10\,\text{fN/nm}$, $\rho = 1700\,\text{kg/m}^3$, $\beta = 1.7\,\text{mV/nm}$. For air at $T = 300\,\text{K}$ and 50% relative humidity, we adopt the values $\eta = 18.3\,\mu\text{Pa}\,\text{s}$, $\rho_\text{f} = 1.17\,\text{kg/m}^3$, and $c_0 = 346.3\,\text{m/s}$.

To evaluate the transfer function H we must know the trap strength κ and microsphere density ρ as well as the fluid's viscosity η, density ρ_f, and sound speed c_0. The equilibrium Brownian motion calibration methods described in Section 4.1.1 may be used to determine κ, ρ, and β. Conversely, η, ρ_f, c_0 may be determined with high accuracy for air using measurements of temperature, relative humidity, and barometric pressure [149, 164]. Furthermore, for a digitized record, the factor $-i/\omega$ appearing in Equation (4.18) that converts between position and velocity is replaced by the reciprocal of Equation (2.80). Once evaluated, the microsphere's sensitivity formulae may be used to convert voltage signals to acoustic measurements using Equation (3.6).

Beyond sensitivity, an important quantifier of any sensor is its self-

noise. Self-noise is the signal measured in the absence of a source. For our microsphere, the self-noise is a combination of Brownian motion and noise in the laser/detection system. The former is well modeled by the ideal Brownian motion voltage power spectral density S_{VV} [Equation (4.1)] and the latter by a constant noise floor $\chi \approx 0.24\,\mu\mathrm{V}^2/\mathrm{Hz}$ (at least for frequencies $f \gtrsim 1\,\mathrm{kHz}$). Hence the velocity self-noise spectral density of our sensor according to Equation (2.78) is

$$S_{\mathrm{nn},u}(\omega) = \frac{S_{VV}(\omega) + \chi}{\left|s_p'(\omega)\right|^2} = \omega^2 \frac{S_{xx}(\omega) + \beta^{-2}\chi}{\left|H(\omega)\right|^2} \tag{4.20}$$

Similarly, the pressure self-noise is $S_{\mathrm{nn},p}(\omega) = Z_0^2 S_{\mathrm{nn},u}(\omega)$. Figure 4.10 (**a**) plots the velocity and pressure self-noise power spectral density predictions. It is clear that Brownian motion dominates the self-noise for $f \lesssim 10^5$ Hz and that the detection noise floor dominates for $f \gtrsim 10^5$ Hz. When Brownian motion dominates, the self-noise is quite flat and near the DC value $S_{\mathrm{nn},u}(\omega \to 0) = 4k_\mathrm{B}T/\gamma$.

The concept of band-limited variance [Equation (2.75)] suggests the cumulative self-noise spectral density as an estimate for the frequency-dependent, minimum-detectable acoustic signals:

$$u_{\min} = \sqrt{\int_0^f \mathrm{d}f'\, S_{\mathrm{nn},u}(2\pi f')}\,, \quad p_{\min} = \sqrt{\int_0^f \mathrm{d}f'\, S_{\mathrm{nn},p}(2\pi f')}\,. \tag{4.21}$$

The predicted minimum-detectable signals are shown in Figure 4.10 (**b**).

Having established the operating principle and basic performance expectations, we next turn to tests of the microsphere as an acoustic detector.

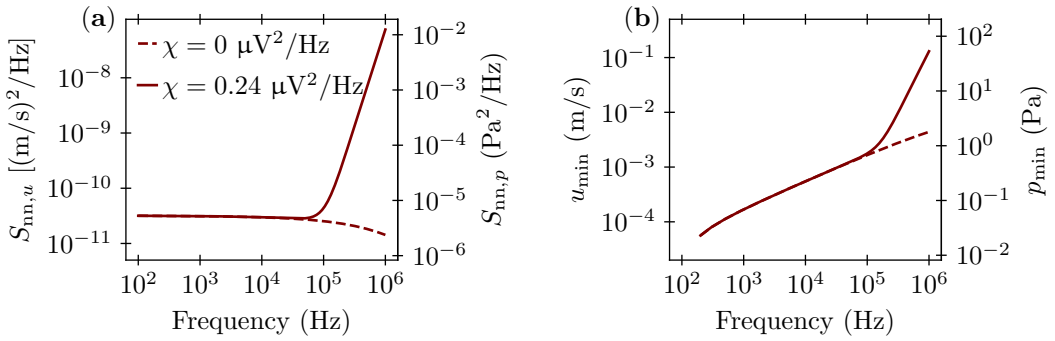

Figure 4.10: **(a)** The predicted self-noise spectral density for velocity (left axis) and pressure (right axis, assuming plane-wave impedance). The dashed line excludes the effects of the detection system's noise floor. (**b**) The predicted minimum-detectable acoustic amplitudes for velocity and pressure.

4.2.2 Tone-burst sound source

We have measured the response of our microsphere to acoustic bursts of pure tones at frequencies 4 kHz and 40 kHz using the piezoelectric speakers discussed in Section 3.3.2. Being only $1/8^{\mathrm{th}}$ inch in diameter, the microphone is placed behind and slightly between the two trap lenses. The Microflown is a bulkier 1/2 inch diameter and so is placed just below the trap lenses. Either piezo speaker may be fixed to a motorized stage that translates parallel to the sound's propagation direction.

We collect 100 records of length $T_{\mathrm{r}} = 9.5\,\mathrm{ms}$ at a sampling rate of 25 MHz. Each record captures the response to one tone-burst pattern. We repeat six such measurement cycles at 10 mm-incremented source distances x_0. The minimum distance is 44 mm. The source-distance scan is repeated twice: once while measuring the microsphere and Microflown simultaneously

and once while measuring the microsphere and the microphone simultaneously. For this experiment, we were able to keep the same microsphere trapped while manually swapping between the two piezo speakers.

Figure 4.11 shows the results for the 40 kHz speaker source-distance scan. Our microsphere results appear to agree well with both commercial sensors for shorter source distances and earlier times. It is possible that at further distances scattering and diffraction break the homogeneity of the acoustic wave at length scales comparable to the separation between the sensors. In other words, the sensors may not be measuring the same acoustic field. Scattering and diffraction could also explain why, since the microphone is placed closer to the optical trap center than the Microflown, we see greater agreement between the microsphere and microphone, Figure 4.11 (**a**), as compared to the microsphere and Microflown, Figure 4.11 (**b**), even at the furthest source distances. The data shown in Figure 4.12 are like that in Figure 4.11, but with the 4 kHz piezo speaker. We find somewhat better agreement at further distances compared to the 40 kHz piezo speaker, though the amplitudes are roughly 10× smaller.

A more quantitative comparison of the early-time and short-distance agreement is shown in Figure 4.13. So far, the results we have presented reflect an ensemble average of 100 records, providing 10× noise reduction. For Figure 4.14 we perform the same analysis as in Figure 4.13 but without ensemble averaging. Indeed, a quite satisfactory agreement is observed even with these 1-shot measurements.

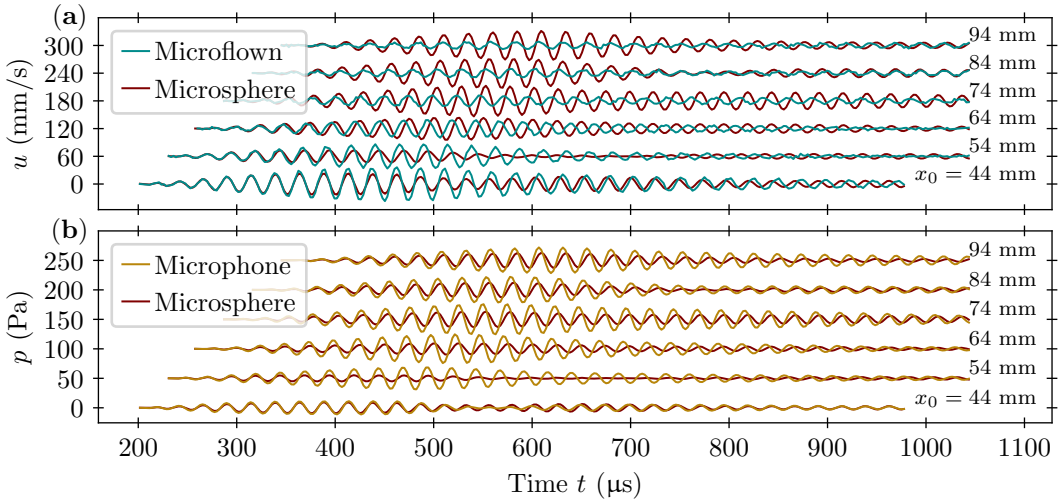

Figure 4.11: 40 kHz tone-burst distance scan. The burst pattern consists of 9 periods driven at 9V. All sensors are analyzed with a bandwidth of 200 kHz and ensemble-averaged over 100 records. (**a**) Velocity measurements are shifted by 60 mm/s relative to one another for visualization purposes. (**b**) Pressure measurements are relatively shifted by 50 Pa.

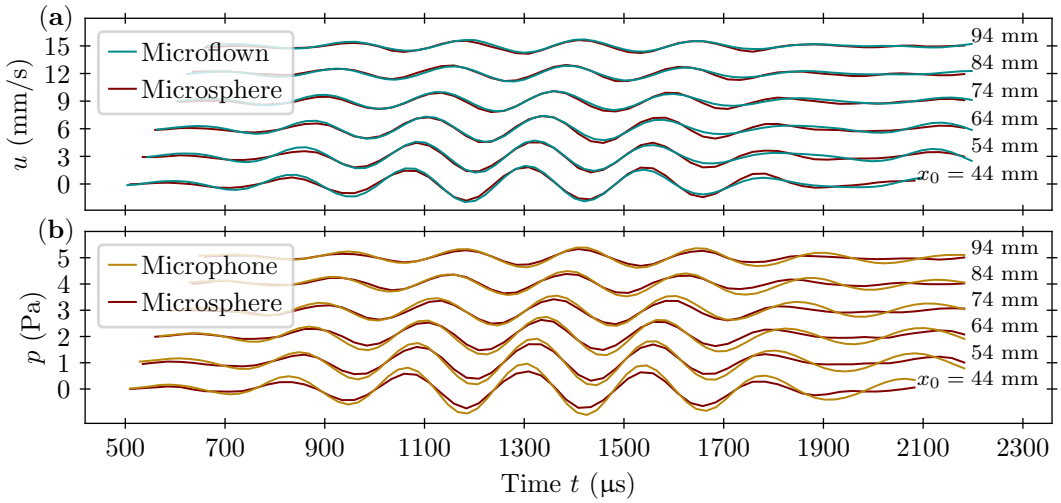

Figure 4.12: 4 kHz tone-burst distance scan. Here, the burst pattern consists of 3 periods driven at 3V. All sensors are analyzed with a bandwidth of 20 kHz and ensemble-averaged over 100 records. Velocity measurements are relatively shifted by 3 mm/s. (**b**) Pressure measurements are relatively shifted by 1 Pa.

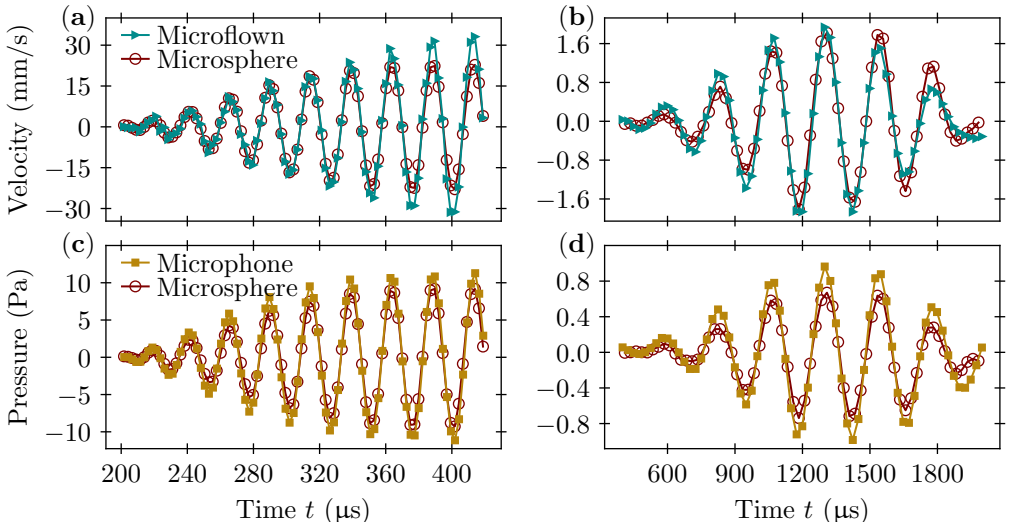

Figure 4.13: Comparing tone burst measurements between (**a** - **b**) the microsphere and Microflown, and (**c** - **d**) the microsphere and microphone. The source distance is $x_0 = 44\,\text{mm}$. All other parameters are as given in Figure 4.11 (40 kHz, left column) or Figure 4.12 (4 kHz, right column).

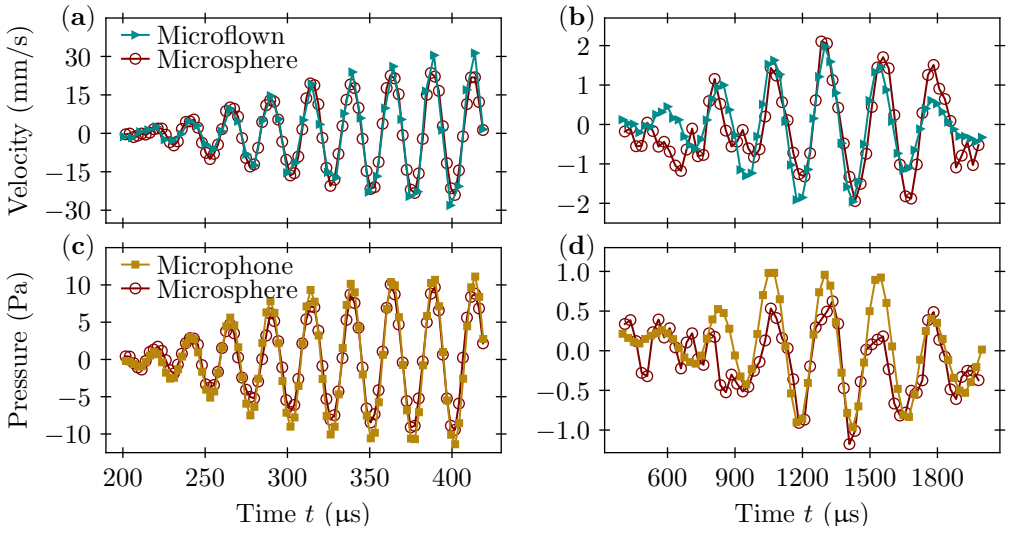

Figure 4.14: Single-shot tone-burst measurement comparison. We show a single record from the ensemble averages shown in Figure 4.13. We also reduced the bandwidth of the Microflown measurement from 200 kHz to 100 kHz to suppress excess electronic noise in the 40 kHz tone-burst measurement.

4.2.3 Laser-ablation sound source

Having validated our sound sensing methodology via tone-burst measurements in the previous section, we now attempt to measure sounds with significantly higher frequency content. Laser ablation of an aluminum target provides an impulsive sound source for this purpose. As described in Chapter 3, a 532 nm, 5 ns laser pulse is focused to about 75 µm on an aluminum target. Here, the pulse energy was set to approximately 10 mJ. Between each pulse, the target is rotated using a stepper motor about an axis parallel to, but laterally displaced from, the incoming pulse. Rotating the target in this way ensures a fresh target is ablated during each record of an acquisition. The rotatable target, steering mirror, and focusing lens (100 mm focal length) are all mounted on a platform that secures to the same motorized stage used to translate the piezo speakers of the previous section.

We collect 10 records of an ablation signal, each 2.6 ms in length, at a sampling rate of $f_s = 25$ MHz. After the 10 records are collected, the ablation source is translated 2.1 mm further away. The minimum distance is 44 mm and 30 such translations are performed, hence the maximum displacement is 104 mm. Simultaneous with recording the microsphere signal, we also record the microphone signal. We do not report impulsive measurements with the Microflown because it has insufficient sensitivity at high frequencies to make reliable measurements. In post-processing, we lowpass filter the signals to the desired bandwidth via bin-averaging. The microphone bandwidth is set to 200 kHz and the microsphere bandwidth is set to 1 MHz.

Figure 4.15 shows the 10-record-ensemble-average ablation signals at six source distances. At shorter source distances, the microsphere signal displays structure not seen in the microphone signal, like a local minimum near the peak pressure and another near the pressure zero-crossing. The microsphere signal also displays higher noise, as seen before the signal's primary rising edge, and this is at least partially due to the ambitious 1 MHz bandwidth selected for the analysis. The local minimum features are not noise because they are seen propagated to later times at larger source distances. Signal noise is unique for each acquisition and therefore would not cause propagating features. When interpreting this data, we must bear in mind that the microsphere is sensitive to acoustic velocity that we convert to pressure using the simplest possible (plane-wave) impedance model. It is conceivable that, especially near the ablation source, this impedance model is overly simplistic and the microphone and microsphere sense quite different fields.

At the farthest observed source distance, the microsphere and microphone signals agree more closely. It is typical in impulsive acoustics to find highly structured near-fields and universal far-fields. Such universal impulse waveforms, called N-waves after the shape of their profile, provide the basis for scale-modeling of sonic booms [110]. Figure 4.16 shows the N-shaped profile measured by the microphone and microsphere at the furthest-tested source distance $x_0 = 104\,\text{mm}$. There, the microsphere signal is shown with a 1 MHz and 200 kHz bandwidth, the latter being the same as the microphone's bandwidth.

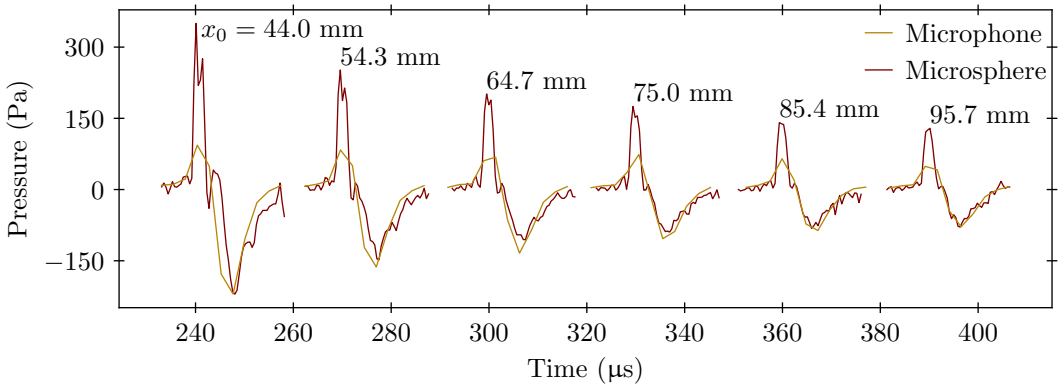

Figure 4.15: Acoustic pressure measurements of the laser ablation sound source. Curves are labeled by their distance to the source x_0 and are each the result of 10 averages. The microphone signals have a bandwidth of 200 kHz and the microsphere signals have a bandwidth of 1 MHz.

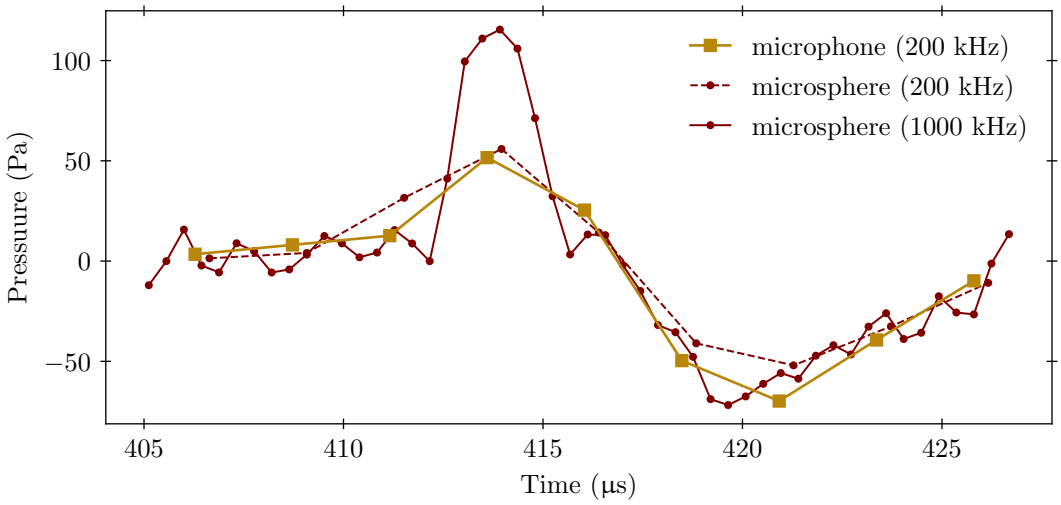

Figure 4.16: Laser ablation acoustic impulse at a source distance of $x_0 = 104$ mm. The dashed line shows the microsphere signal when analyzed with the same bandwidth as the microphone.

We quantify the peak pressure as the signal maximum and the peak rise time as the amount of time it takes for the signal's leading edge to increase from 10% of the peak pressure to 90% of the peak pressure. Figure 4.17 shows the peak pressure and peak rise time for increasing source distance. Evidently, reducing the microsphere's measurement bandwidth to that of the microphone in post-processing accounts for a significant portion of the difference in peak features measured by the two sensors. The peak pressure decays with distance as a power law. Upon reducing the microsphere's bandwidth, the peak pressure's power law exponent is relatively unchanged, though its magnitude is significantly reduced. Additionally, we find that reducing the microsphere's bandwidth by a factor of 5 increases the observed rise time by nearly the same factor. This suggests the rise-time measurements could be band-limited, even with a 1 MHz bandwidth.

4.2.4 Discussion

Combining the velocity transfer function from hydrodynamic theory with equilibrium calibration techniques has enabled acoustic measurements using our optically trapped microsphere system. Our technique is quite different from the established standards for calibrating a microphone, i.e. measuring the sensor's response to a well-characterized source under anechoic conditions. It is perhaps surprising, then, that our measurements agree at the level observed in Section 4.2.2.

Our microsphere resolves larger peak pressures and shorter rise times

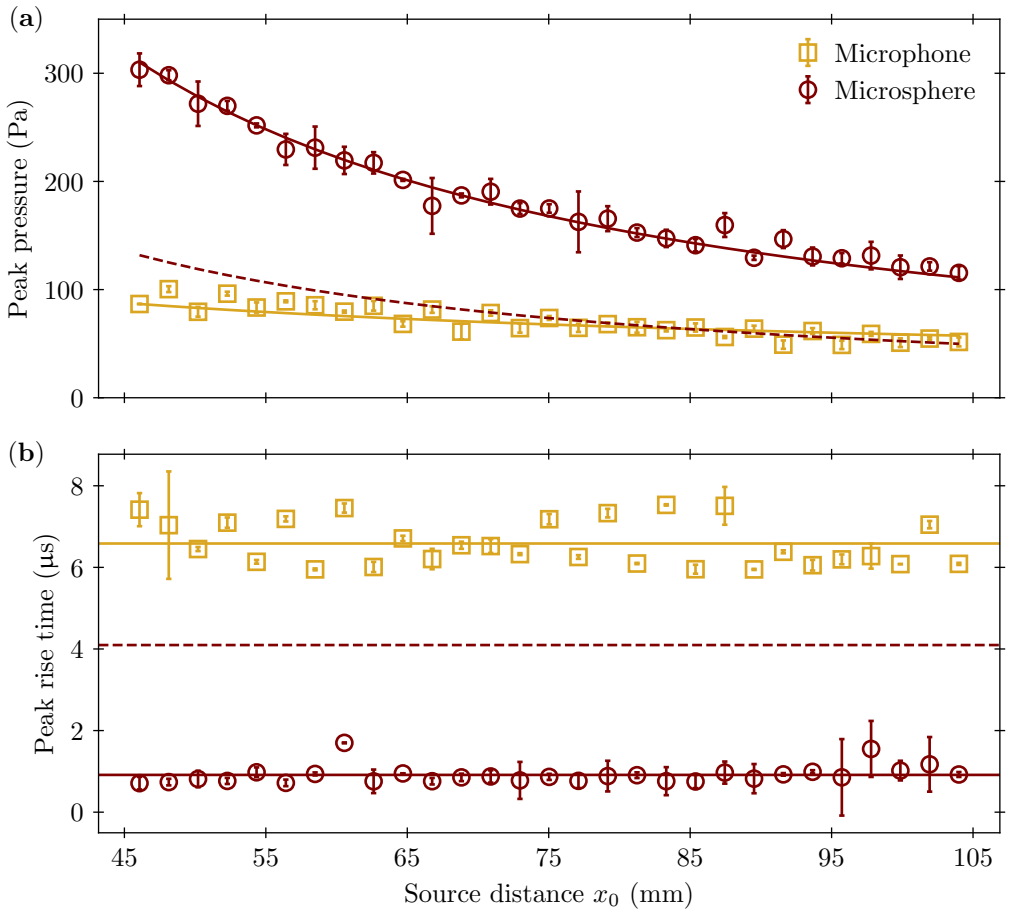

Figure 4.17: Quantifying the acoustic peak generated by laser ablation. Symbols are the average over 10 records and the error bars are the corresponding standard deviation. (**a**) The peak pressure is well fit by the power law ax_0^b (solid lines). We find $b = -1.3$ for the microsphere and $b = -0.51$ for the microphone. Reducing the microsphere bandwidth to 200 kHz results in $b = -1.2$ (the dashed red line reflects the fit, data not shown for visual clarity). (**b**) The 10-90 peak rise times. Here, the solid lines reflect the average over source distances. These averages are 6.6 µs for the microphone, 4.1 µs for the microsphere with a bandwidth of 200 kHz (dashed line, data not shown), and 0.9 µs for the microsphere with a bandwidth of 1 MHz.

compared to our high-bandwidth microphone. This indicates that the microsphere's sensitivity to high-frequency sounds enables measurements that cannot be performed with our microphone, which has the highest commercially-available bandwidth. Of course, the microphone's sensitivity, seen in Figure 4.9, is engineered to have a very flat amplitude response up to the design bandwidth, followed by a steep cutoff. This is achieved by engineering the microphone's electronic amplifier system. Physically, the microphone membrane has sensitivity beyond the design bandwidth, but it becomes increasingly challenging to maintain a flat response beyond the membrane's first resonance.

To our knowledge, our work is the first demonstration of a new sensing modality for optical tweezers. By monitoring the microsphere's instantaneous velocity in response to sonic, ultrasonic, and impulsive sounds, we infer the motion of the fluid that is local to the microsphere. For the remainder of this Section, we will outline the work most similar to ours that we have reviewed from the literature. This exercises will highlight the uniqueness of our approach.

First, one other work has couched their experiments as acoustic sensing using optically trapped microspheres [160], but in a dramatically different regime. In that work, a 60 nm gold sphere is trapped in water and imaged at 50 Hz with a camera. Sounds are generated by 1) a CW laser beam focused onto a nearby cluster of gold nanoparticles and intensity-modulated at 10 Hz to 50 Hz and 2) by a needle attached to a 300 Hz loudspeaker. Since the detection method is slow, the methodology hinges on measuring the particle's position

variance in the presence of sound, and hence no time-dependent waveforms may be measured. The authors claim to be able to detect sound power down to a level of -60 dB. They do not specify the reference value of the dB scale, but it appears to be 1 pW, the typical reference value for air-based measurements. The quoted sound powers are at best an order of magnitude estimate. As a part of their sound power level derivation they say "...the drag force exerted on the nanoparticle is compensated at a certain maximum displacement $x_{\max}$ by the restoring force of the optical trap: $\kappa x_{\max} = 6\pi\eta v_{\max}$." Yet, that force balance does not hold at any single instant in time since for harmonic oscillations $x_{\max}$ and $v_{\max}$ are 90° out of phase.

Similar methodologies to that in [160] have been used to make velocity flow measurements in aqueous environments. In [158] a bacterium is optically trapped about 2 µm away from a 1.76 µm silica microsphere. The flow generated by the bacterium's rotating flagella bundle affects the microsphere's motion which is monitored using 500 Hz imaging and analyzed in the frequency domain. In [159] the flow generated by a driven optically trapped microsphere (R=0.88 µm) is measured in water. The drive is provided at 197 Hz by periodically blocking and unblocking one of two traps transversely separated by 504 nm, causing the drive particle to jump between the traps. Detection is provided by a second nearby optically trapped particle monitored with a 1000 Hz camera. The authors successfully map a steady, two-dimensional vectorial flow field over an area of $\sim$20 µm^2 by scanning the detection microsphere's equilibrium position.

In a recent work termed *optical tweezer-based velocimetry* [161], a position-sensitive detector monitors a microsphere optically trapped in a water-filled sample chamber. The sample chamber is piezoelectrically driven at frequencies of 1 Hz - 90 Hz. Velocity amplitudes of 1.5 µm/s - 70 µm/s are detected in real-time. Such low amplitudes beat the thermal limit by using a Kalman filter to deduce the flow velocity from microsphere position measurements in the presence of Brownian motion. Their detection system's bandwidth is not specified, but they show spectra consistent with a sample rate of at least 2 kHz.

In another recent work [162], a silica microsphere ($R = 2.77\,\mu m$) is optically trapped in water and driven laterally at 50 Hz to 400 Hz. An additional 30 smaller polystyrene tracer particles ($R = 0.505\,\mu m$), initially optically trapped at fixed locations near the drive particle, are released upon starting the drive. The free tracers follow elliptical Lissajous trajectories, in agreement with theory.

Finally, in [163] a 5.20 µm diameter microsphere is trapped in water that is contained within a 6.8 MHz, piezo-driven, standing-wave chamber. The time-averaged microsphere position is recorded using a camera at 150 Hz. The trap center can be adjusted over $100\,\mu m \times 150\,\mu m$ and the sample can translate 74 mm × 120 mm. The displacement of the microsphere from its equilibrium position maps the standing-wave profile.

Our work presented in this Section is unique because it is performed in air, it makes quantitative acoustic field measurements that are benchmarked

against well-calibrated detectors, and it does so with enough time resolution to observe acoustic waveforms at 4 kHz and 40 kHz, as well as impulsive waveforms with frequency content in the megahertz-range.

Chapter 5

Conclusions

5.1 Recapitulation

The work presented in this dissertation has tested the mass and sound sensing capabilities of an optically trapped microsphere.

We have explored spectral and equipartition methods by which to sense a microsphere's inertial mass as it undergoes Brownian motion in air. With the former, we accurately extract physical parameters of trap strength κ, microsphere density ρ, and detector calibration constant β with 3 seconds of data. The initial spectral calibration step also yields the mass m_1 with 3.2% uncertainty. The subsequent equipartition method m_2 achieves an uncertainty of 4.3% in 0.3 seconds and is enabled by our detector's ability to resolve the microsphere's instantaneous velocity.

To detect sound, we have developed a theoretical model describing the air's motion in terms of the microsphere's motion. Sensitivity, self-noise, and minimum-detectable signal amplitudes are all predicted using our model. In contrast to inertial mass sensing, Brownian motion is interpreted as a source of noise. Physically, the microsphere is entrained in the acoustic velocity field and therefore follows it with a predictable amplitude and phase. Our

model was verified by making simultaneous measurements with our system and two state-of-the-art, commercially-available acoustic detectors when subject to tone bursts at 4 kHz and 40 kHz. When subject to an impulsive sound source derived from laser ablation, our microsphere resolves a 7.3× shorter rise time and a $\sim 3\times$ higher peak pressure than our high-bandwidth microphone.

5.2 Outlook and future applications

Having established our system's ability to measure mass and sound, what applications could be imagined for the future?

For mass measurement, we have in mind aerosol science. Already, optical traps combined with tools like laser spectroscopy provide researchers with a unique platform for studying aerosols at the single-particle level [165]. Studies of super-cooled organic droplets [166] and the formation of water [167,168] and ammonium sulfate [169] crystals, all in an air environment, have been enabled by optical trapping techniques. It would be fascinating to supplement these experiments with fast position detection. Then, our technique for fast mass measurement could monitor the growth of droplets and crystals in new ways.

Acoustic detection, especially with sensitivity at high frequencies, also supports a few applications. For example, in proton therapy — an emerging cancer treatment — high-energy protons are directed into a patient's body, aimed at a tumor. The protons deposit most of their energy in a well-localized point within the tissue, known as the Bragg peak. While effective and non-invasive, proton therapy suffers from a lack of real-time monitoring. Recent

efforts have investigated the use of acoustic sensors to monitor proton therapy in real-time, relying on the fact that an impulsive acoustic wave is sourced at the Bragg peak [170, 171]. Another possibility is to detect similar proton-generated acoustic waves occurring in bubble chambers — devices in which fundamental particles leave tracks of bubbles as they pass through. Acoustic detectors have already been used to veto "uninteresting" proton tracks in bubble-chamber searches for dark matter [172–174].

The efficacy of acoustical monitoring for proton therapy and bubble chamber particle physics is limited by the signal-to-noise ratio of the acoustic sensor. Could an optically trapped microsphere provide an improved measurement? The answer is not immediately clear because in both applications the sound originates in a non-air environment (e.g. CF_3I or C_3F_8 for a bubble chamber or water for the human body). Nonetheless, our method for acoustic detection is new and its operational principle has been proven. Further refinements are needed to maximize the methods' sensitivity, to make it more practical, and to test our model in alternative media. Our group hopes to pursue these endeavors and others in the future

As a final remark, it is worth again highlighting that our mass and sound measurements have been enabled by the resolution of a Brownian particle's instantaneous velocity. There may well be other measurement protocols that could benefit from similar detection capabilities. Moreover, could other sensing applications be enabled by yet higher resolution position tracking? Indeed, there exists an ultra-short time scale of Brownian motion where the

compressibility of the surrounding fluid becomes relevant. Measurements in this regime have not yet been performed, but our group has proposed a method for doing so [175]. Verifying the velocity equipartition theorem in the compressible regime of a liquid, that is, observing the bare rather than fluid-dressed mass of a microsphere, would provide an exciting verification of statistical mechanics theory. Further, at such short time scales, we may be able to observe the onset of viscous effects in the form of early-time non-exponential velocity correlation decay. Perhaps providing optical kicks at times shorter than the onset of viscosity could move a microsphere as if it were immersed in a superfluid, despite being coupled to water at room temperature.

Feynman famously said there is "plenty of room at the bottom" when he (arguably) inaugurated the field of nanotechnology [176]. Pushing the limits of experimental feasibility has always led to near-bottomless discoveries. As Feynman points out, Onnes enabled low-temperature physics, and Bridgman, by devising methods for high pressures experiments, "opened up another new field and was able to move into it and to lead us all along." It seems also true that there is plenty of room at the bottom of the time-axis of Brownian motion. Thus, we conclude this work, as is often done in the sciences, with a question: What applications, theory confirmations, and genuine surprises await us at the shortest time scales of mechanical motion in a fluid-coupled environment?

Bibliography

[1] Andrea Macchi and Onofrio M. Maragò, *Light pressure across all scales: editorial*, The European Physical Journal Plus **136** (2021), no. 5, 582.

[2] Johannes Kepler, *De cometis libelli tres*, Typis Andreae Apergeri, 1619.

[3] James Clerk Maxwell, *A treatise on electricity and magnetism*, vol. 1, Clarendon Press, 1873.

[4] Adolfo Bartoli, *Il calorico raggiante e il secondo principio di termodinamica*, Il Nuovo Cimento **15** (1884), no. 1, 193–202.

[5] Peter Lebedew, *Untersuchungen über die druckkräfte des lichtes*, Annalen der Physik **311** (1901), no. 11, 433–458.

[6] William Crookes, *On attraction and repulsion resulting from radiation*, Philosophical Transactions of the Royal Society of London **164** (1874), 501–527.

[7] E. F. Nichols and G. F. Hull, *A preliminary communication on the pressure of heat and light radiation*, Physical Review (Series I) **13** (1901), 307–320.

[8] Tomaž Požar, Jernej Laloš, Aleš Babnik, Rok Petkovšek, Max Bethune-Waddell, Kenneth J. Chau, Gustavo V. B. Lukasievicz, and Nelson G. C.

Astrath, *Isolated detection of elastic waves driven by the momentum of light*, Nature Communications **9** (2018), no. 1, 1–11.

[9] Charles H. Townes, *How the laser happened: Adventures of a scientist*, Oxford University Press, 2002.

[10] Arthur Ashkin, *The pressure of laser light*, Scientific American **226** (1972), no. 2, 62–71.

[11] Bill Hodgetts, R. Aud, and Dylan Scott, *Did you know how loud balloons can be?*, Canadian Audiologist **3** (2016), no. 6.

[12] Arthur Ashkin, *Acceleration and trapping of particles by radiation pressure*, Physical Review Letters **24** (1970), no. 4, 156.

[13] Arthur Ashkin and J. M. Dziedzic, *Optical levitation by radiation pressure*, Applied Physics Letters **19** (1971), no. 8, 283–285.

[14] Arthur Ashkin, James M. Dziedzic, John E. Bjorkholm, and Steven Chu, *Observation of a single-beam gradient force optical trap for dielectric particles*, Optics Letters **11** (1986), no. 5, 288–290.

[15] A. Ashkin, *Atomic-beam deflection by resonance-radiation pressure*, Physical Review Letters **25** (1970), 1321–1324.

[16] Theodor W. Hänsch and Arthur L. Schawlow, *Cooling of gases by laser radiation*, Optics Communications **13** (1975), no. 1, 68–69.

[17] Nobel Prize Outreach, *All nobel prizes in physics*, https://www.nobelprize.org/prizes/lists/all-nobel-prizes-in-physics/, Accessed: 6 August 2022.

[18] Sepehr Ebadi, Tout T. Wang, Harry Levine, Alexander Keesling, Giulia Semeghini, Ahmed Omran, Dolev Bluvstein, Rhine Samajdar, Hannes Pichler, Wen Wei Ho, Soonwon Choi, Subir Sachdev, Markus Greiner, Vladan Vuletić, and Mikhail D. Lukin, *Quantum phases of matter on a 256-atom programmable quantum simulator*, Nature **595** (2021), no. 7866, 227–232.

[19] Dolev Bluvstein, Harry Levine, Giulia Semeghini, Tout T. Wang, Sepehr Ebadi, Marcin Kalinowski, Alexander Keesling, Nishad Maskara, Hannes Pichler, Markus Greiner, Vladan Vuletić, and Mikhail D. Lukin, *A quantum processor based on coherent transport of entangled atom arrays*, Nature **604** (2022), no. 7906, 451–456.

[20] Arthur Ashkin, James M. Dziedzic, and T. Yamane, *Optical trapping and manipulation of single cells using infrared laser beams*, Nature **330** (1987), no. 6150, 769–771.

[21] Arthur Ashkin, *History of optical trapping and manipulation of small-neutral particle, atoms, and molecules*, IEEE Journal of Selected Topics in Quantum Electronics **6** (2000), no. 6, 841–856.

[22] Arthur Ashkin and James M. Dziedzic, *Optical trapping and manipulation of viruses and bacteria*, Science **235** (1987), no. 4795, 1517–1520.

[23] Karel Svoboda and Steven M. Block, *Biological applications of optical forces*, Annual Review of Biophysics and Biomolecular Structure **23** (1994), no. 1, 247–285.

[24] Adolphe Brongniart, *Memoire sur la generation et le developpement de l'embryon dans les vegetaux phanerogames*, Annales des Sciences Naturelles **12** (1827), 41.

[25] Stephen Gray, *Several microscopical observations and experiments, made by Mr. Stephen Gray*, Philosophical Transactions of the Royal Society of London **19** (1696), no. 221, 280–287.

[26] Albert Einstein, *On the motion of small particles suspended in liquids at rest required by the molecular-kinetic theory of heat*, Annalen der Physik **17** (1905), no. 549-560, 208.

[27] Marian Smoluchowski, *The kinetic theory of brownian molecular motion and suspensions*, Annals of Physics **21** (1906), 756–780.

[28] Paul Langevin, *Sur la théorie du mouvement brownien*, Comptes Rendus **146** (1908), 530–533.

[29] Theodor Svedberg, *Studien zur lehre von den kolloiden lösungen*, Akademische Buchdruckerei, 1907.

[30] J. Perrin and F. Soddy, *Brownian movement and molecular reality*, Annales de Chimie et de Physique, Taylor & Francis, 1910.

[31] Joseph Delsaulx, *Thermo-dynamic origin of the brownian motions*, The Monthly Microscopical Journal **18** (1877), no. 1, 1–7.

[32] Albert Einstein, *On the electrodynamics of moving bodies*, Annalen der Physik **17** (1905), no. 10, 891–921.

[33] Albert Einstein, *Theoretische bemerkungen über die brownsche bewegung*, Zeitschrift für Elektrochemie und angewandte physikalische Chemie **13** (1907), no. 6, 41–42.

[34] Tongcang Li, Simon Kheifets, David Medellin, and Mark G. Raizen, *Measurement of the instantaneous velocity of a brownian particle*, Science **328** (2010), no. 5986, 1673–1675.

[35] Simon Kheifets, Akarsh Simha, Kevin Melin, Tongcang Li, and Mark G. Raizen, *Observation of brownian motion in liquids at short times: instantaneous velocity and memory loss*, Science **343** (2014), no. 6178, 1493–1496.

[36] K. S. Melin, P. I. Nagornykh, Y. Lu, L. E. Hillberry, Y. Xu, and M. G. Raizen, *Observation of a quasi-one-dimensional variation of the stern-gerlach effect*, Physical Review A **99** (2019), no. 6, 063417.

[37] Logan E. Hillberry, Matthew T. Jones, David L. Vargas, Patrick Rall, Nicole Yunger Halpern, Ning Bao, Simone Notarnicola, Simone Montangero, and Lincoln D. Carr, *Entangled quantum cellular automata,*

physical complexity, and goldilocks rules, Quantum Science and Technology **6** (2021), no. 4, 045017.

[38] Eric B. Jones, Logan E. Hillberry, Matthew T. Jones, Mina Fasihi, Pedram Roushan, Zhang Jiang, Alan Ho, Charles Neill, Eric Ostby, Peter Graf, et al., *Small-world complex network generation on a digital quantum processor*, Nature communications **13** (2022), no. 1, 1–7.

[39] Peter W. Milonni and Joseph H. Eberly, *Laser physics*, John Wiley & Sons, 2010.

[40] John P. Barton and Dennis R. Alexander, *Fifth-order corrected electromagnetic field components for a fundamental gaussian beam*, Journal of Applied Physics **66** (1989), no. 7, 2800–2802.

[41] Bruce T. Draine and Jeremy Goodman, *Beyond clausius-mossotti-wave propagation on a polarizable point lattice and the discrete dipole approximation*, The Astrophysical Journal **405** (1993), 685–697.

[42] G. E. Vekstein, *On the electromagnetic force on a moving dipole*, European Journal of Physics **18** (1997), no. 2, 113.

[43] Patrick C. Chaumet and Manuel Nieto-Vesperinas, *Time-averaged total force on a dipolar sphere in an electromagnetic field*, Optics Letters **25** (2000), no. 15, 1065–1067.

[44] Paolo Polimeno, Alessandro Magazzù, Maria Antonia Iatì, Francesco Patti, Rosalba Saija, Cristian Degli Esposti Boschi, Maria Grazia

Donato, Pietro G. Gucciardi, Philip H. Jones, Giovanni Volpe, and Onofrio M. Maragò, *Optical tweezers and their applications*, Journal of Quantitative Spectroscopy and Radiative Transfer **218** (2018), 131–150.

[45] Silvia Albaladejo, Manuel I. Marqués, Marine Laroche, and Juan José Sáenz, *Scattering forces from the curl of the spin angular momentum of a light field*, Physical Review Letters **102** (2009), no. 11, 113602.

[46] David B. Ruffner and David G. Grier, *Comment on scattering forces from the curl of the spin angular momentum of a light field*, Physical Review Letters **111** (2013), no. 5, 059301.

[47] Manuel I. Marqués and Juan José Sáenz, *Marqués and Sáenz reply*, Physical Review Letters **111** (2013), no. 5, 059302.

[48] B. A. Kemp, *Resolution of the abraham-minkowski debate: Implications for the electromagnetic wave theory of light in matter*, Journal of Applied Physics **109** (2011), no. 11, 7.

[49] Manuel I. Marqués, Shulamit Edelstein, and Pedro A. Serena, *A proposal to measure belinfante's curl of the spin optical force based on the kerker conditions*, The European Physical Journal Plus **136** (2021), no. 2, 1–9.

[50] A. Clebsch, *Ueber die reflexion an einer kugelfl ache.*, Journal f ur die reine und angewandte Mathematik **1863** (1863), no. 61, 195–262.

[51] Ludvig Lorenz, *Lysbevaegelsen i og uden for en af plane lysbolger belyst kugle*, Det Kongelige Danske Videnskabernes Selskabs Skrifter **6** (1890), no. 6, 1–62.

[52] Gustav Mie, *Beiträge zur optik trüber medien, speziell kolloidaler metallösungen*, Annalen der Physik **330** (1908), no. 3, 377–445.

[53] Giuseppe Pesce, Philip H. Jones, Onofrio M. Maragò, and Giovanni Volpe, *Optical tweezers: theory and practice*, The European Physical Journal Plus **135** (2020), no. 12, 1–38.

[54] Timo A. Nieminen, Vincent L. Y. Loke, Alexander B. Stilgoe, Gregor Knöner, Agata M. Brańczyk, Norman R. Heckenberg, and Halina Rubinsztein-Dunlop, *Optical tweezers computational toolbox*, Journal of Optics A: Pure and Applied Optics **9** (2007), no. 8, S196.

[55] Isaac C. D. Lenton, Alexander B. Stilgoe, Timo A. Nieminen, V. L. Y. Loke, Y. Hu, G. Kröner, A. M. Branczyk, N. R. Heckenberg, Halina Rubinsztein-Dunlop, and Others, *Optical tweezers toolbox*, 2019.

[56] T. A. Nieminen, H. Rubinsztein-Dunlop, and N. R. Heckenberg, *Calculation of the t-matrix: general considerations and application of the point-matching method*, Journal of Quantitative Spectroscopy and Radiative Transfer **79** (2003), 1019–1029.

[57] Estefanía de Mirandés, Pauline Barat, Michael Stock, and Martin J. T. Milton, *Calibration campaign against the international prototype of the*

kilogram in anticipation of the redefinition of the kilogram, part II: evolution of the BIPM as-maintained mass unit from the 3rd periodic verification to 2014, Metrologia **53** (2016), no. 5, 1204.

[58] D. Haddad, Frank Seifert, L.S. Chao, Antonio Possolo, David B. Newell, Jon R. Pratt, Carl J. Williams, and Stephan Schlamminger, *Measurement of the planck constant at the national institute of standards and technology from 2015 to 2017*, Metrologia **54** (2017), no. 5, 633.

[59] Savely G. Karshenboim, *Some possibilities for laboratory searches for variations of fundamental constants*, Canadian Journal of Physics **78** (2000), no. 7, 639–678.

[60] Fabian Czerwinski, Andrew C. Richardson, and Lene B. Oddershede, *Quantifying noise in optical tweezers by allan variance*, Optics Express **17** (2009), no. 15, 13255–13269.

[61] David W. Allan, *Statistics of atomic frequency standards*, Proceedings of the IEEE **54** (1966), no. 2, 221–230.

[62] Sunaina, Mansi Butola, and Kedar Khare, *Calculating numerical derivatives using fourier transform: some pitfalls and how to avoid them*, European Journal of Physics **39** (2018), no. 6, 065806.

[63] George E. Uhlenbeck and Leonard S. Ornstein, *On the theory of the brownian motion*, Physical Review **36** (1930), no. 5, 823.

[64] Jérôme Duplat, Simon Kheifets, Tongcang Li, Mark G. Raizen, and Emmanuel Villermaux, *Superdiffusive trajectories in brownian motion*, Physical Review E **87** (2013), no. 2, 020105.

[65] Thai M. Hoang, Rui Pan, Jonghoon Ahn, Jaehoon Bang, H. T. Quan, and Tongcang Li, *Experimental test of the differential fluctuation theorem and a generalized jarzynski equality for arbitrary initial states*, Physical Review Letters **120** (2018), no. 8, 080602.

[66] Giorgio Volpe and Giovanni Volpe, *Simulation of a brownian particle in an optical trap*, American Journal of Physics **81** (2013), no. 3, 224–230.

[67] R. Kubo, *The fluctuation-dissipation theorem*, Reports on Progress in Physics **29** (1966), no. 1, 255–284.

[68] A. B. Basset, *On the motion of a sphere in a viscous liquid*, Philosophical Transactions of the Royal Society of London Series A **179** (1888), 43–63.

[69] G. G. Stokes, *On the effect of the internal friction of fluids on the motion of pendulums*, Transactions of the Cambridge Philosophical Society **9** (1851), 8.

[70] Jana Tóthová and Vladimír Lisỳ, *A note on the fluctuation–dissipation relation for the generalized langevin equation with hydrodynamic backflow*, Physics Letters A **380** (2016), no. 33, 2561–2564.

[71] Edward John Hinch, *Application of the langevin equation to fluid suspensions*, Journal of Fluid Mechanics **72** (1975), no. 3, 499–511.

[72] H. J. H. Clercx and P. P. J. M. Schram, *Brownian particles in shear flow and harmonic potentials: A study of long-time tails*, Physical Review A **46** (1992), no. 4, 1942.

[73] Aneesur Rahman, *Correlations in the motion of atoms in liquid argon*, Physical Review **136** (1964), no. 2A, A405.

[74] B. J. Alder and T. E. Wainwright, *Velocity autocorrelations for hard spheres*, Physical Review Letters **18** (1967), no. 23, 988.

[75] B. J. Alder and T. E. Wainwright, *Decay of the velocity autocorrelation function*, Physical Review A **1** (1970), 18–21.

[76] Robert Zwanzig and Mordechai Bixon, *Hydrodynamic theory of the velocity correlation function*, Physical Review A **2** (1970), 2005–2012.

[77] S. Temkin and C.-M. Leung, *On the velocity of a rigid sphere in a sound wave*, Journal of Sound and Vibration **49** (1976), no. 1, 75–92.

[78] Martin R. Maxey and James J. Riley, *Equation of motion for a small rigid sphere in a nonuniform flow*, Physics of Fluids **26** (1983), no. 4, 883–889.

[79] Jay Cleckler, Said Elghobashi, and Feng Liu, *On the motion of inertial particles by sound waves*, Physics of Fluids **24** (2012), no. 3, 033301.

[80] Yu Zheng and Fangwen Sun, *Three-dimensional position measurement of a levitated nanoparticle in a vacuum by a dove prism*, Chinese Optics Letters **17** (2019), no. 6, 060901.

[81] Simon Kheifets, *High-sensitivity tracking of optically trapped particles in gases and liquids: observation of brownian motion in velocity space*, Ph.D. thesis, The University of Texas at Austin, 2014.

[82] R. Gordon, M. Kawano, J. T. Blakely, and D. Sinton, *Optohydrodynamic theory of particles in a dual-beam optical trap*, Physical Review B **77** (2008), 245125.

[83] Xinlin Chen, Guangzong Xiao, Hui Luo, Wei Xiong, and Kaiyong Yang, *Dynamics analysis of microsphere in a dual-beam fiber-optic trap with transverse offset*, Optics Express **24** (2016), no. 7, 7575–7584.

[84] A. B. Stilgoe, N. R. Heckenberg, T. A. Nieminen, and H. Rubinsztein-Dunlop, *Phase-transition-like properties of double-beam optical tweezers*, Physical Review Letters **107** (2011), 248101.

[85] Aidan Rafferty and Thomas C. Preston, *Trapping positions in a dual-beam optical trap*, Journal of Applied Physics **130** (2021), no. 18, 183105.

[86] Frederick Gittes and Christoph F. Schmidt, *Interference model for back-focal-plane displacement detection in optical tweezers*, Optics Letters **23** (1998), no. 1, 7–9.

[87] Patrick Kwee and Benno Willke, *Automatic laser beam characterization of monolithic Nd: YAG nonplanar ring lasers*, Applied Optics **47** (2008), no. 32, 6022–6032.

[88] Walter Schottky, *Über spontane stromschwankungen in verschiedenen elektrizitätsleitern*, Annalen der Physik **362** (1918), no. 23, 541–567.

[89] Lars S. Madsen, Muhammad Waleed, Catxere A. Casacio, Alex Terrasson, Alexander B. Stilgoe, Michael A. Taylor, and Warwick P Bowen, *Ultrafast viscosity measurement with ballistic optical tweezers*, Nature Photonics **15** (2021), 386–392.

[90] Michael A. Taylor and Warwick P. Bowen, *Quantum noise in optical tweezers*, Journal of Physics: Conference Series, vol. 467, IOP Publishing, 2013, p. 012007.

[91] Guoyao Li and Zhang-Qi Yin, *Squeezing light via levitated cavity optomechanics*, Photonics, vol. 9, MDPI, 2022, p. 57.

[92] William H. Press, *Flicker noises in astronomy and elsewhere*, Comments on Astrophysics **7** (1978), 103–119.

[93] Werner Stöber, Arthur Fink, and Ernst Bohn, *Controlled growth of monodisperse silica spheres in the micron size range*, Journal of Colloid and Interface Science **26** (1968), no. 1, 62–69.

[94] Howard Brenner, *The stokes resistance of a slightly deformed sphere*, Chemical Engineering Science **19** (1964), no. 8, 519–539.

[95] Boris V. Derjaguin, Vladimir M. Muller, and Yu P. Toporov, *Effect of contact deformations on the adhesion of particles*, Journal of Colloid and Interface Science **53** (1975), no. 2, 314–326.

[96] Lars-Oliver Heim, Jürgen Blum, Markus Preuss, and Hans-Jürgen Butt, *Adhesion and friction forces between spherical micrometer-sized particles*, Physical Review Letters **83** (1999), no. 16, 3328.

[97] Evan Weisman, Chethn Krishna Galla, Cris Montoya, Eduardo Alejandro, Jason Lim, Melanie Beck, George P. Winstone, Alexey Grinin, William Eom, and Andrew A. Geraci, *An apparatus for in-vacuum loading of nanoparticles into an optical trap*, arXiv preprint arXiv:2208.02102 (2022).

[98] Tongcang Li, *Fundamental tests of physics with optically trapped microspheres*, Ph.D. thesis, The University of Texas at Austin, 2011.

[99] Ayub Khodaee, Kahan Dare, Aisling Johnson, Uroš Delić, and Markus Aspelmeyer, *Dry launching of silica nanoparticles in vacuum*, arXiv preprint arXiv:2209.00482 (2022).

[100] Maryam Nikkhou, Yanhui Hu, James A. Sabin, and James Millen, *Direct and clean loading of nanoparticles into optical traps at millibar pressures*, Photonics, vol. 8, Multidisciplinary Digital Publishing Institute, 2021, p. 458.

[101] GRAS Sound and Vibration, *The world's smallest measurement microphone set*, https://www.grasacoustics.com/news/47-46de, 2017, Accessed: 18 October 2022.

[102] H.-E. de Bree, W. F. Druyvesteyn, E. Berenschot, and M. Elwenspoek, *Three-dimensional sound intensity measurements using microflown particle velocity sensors*, Technical Digest. IEEE International MEMS 99 Conference. Twelfth IEEE International Conference on Micro Electro Mechanical Systems (Cat. No. 99CH36291), IEEE, 1999, pp. 124–129.

[103] Hans-Elias de Bree, *An overview of microflown technologies*, Acta Acustica United with Acustica **89** (2003), no. 1, 163–172.

[104] Hans-Elias de Bree, *The microflown e-book*, https://www.microflown.com/resources/e-books/e-book-the-microflown-e-book, 2009, Accessed: 18 October 2022.

[105] X. Liu, D. Du, and G. Mourou, *Laser ablation and micromachining with ultrashort laser pulses*, IEEE Journal of Quantum Electronics **33** (1997), no. 10, 1706–1716.

[106] Celio Pasquini, Juliana Cortez, Lucas Silva, and Fabiano B Gonzaga, *Laser induced breakdown spectroscopy*, Journal of the Brazilian Chemical Society **18** (2007), 463–512.

[107] Paul Gibbon and Eckhart Förster, *Short-pulse laser-plasma interactions*, Plasma Physics and Controlled Fusion **38** (1996), no. 6, 769.

[108] Itsuro Kajiwara, Ryosuke Akita, and Naoki Hosoya, *Damage detection in pipes based on acoustic excitations using laser-induced plasma*, Mechanical Systems and Signal Processing **111** (2018), 570–579.

[109] Lihong V. Wang and Song Hu, *Photoacoustic tomography: in vivo imaging from organelles to organs*, Science **335** (2012), no. 6075, 1458–1462.

[110] Qin Qin and Keith Attenborough, *Characteristics and application of laser-generated acoustic shock waves in air*, Applied Acoustics **65** (2004), no. 4, 325–340.

[111] Markus W. Sigrist, *Laser generation of acoustic waves in liquids and gases*, Journal of Applied Physics **60** (1986), no. 7, R83–R122.

[112] Todd W. Murray and James W. Wagner, *Laser generation of acoustic waves in the ablative regime*, Journal of Applied Physics **85** (1999), no. 4, 2031–2040.

[113] Julian Kappler, Shamit Shrivastava, Matthias F. Schneider, and Roland R. Netz, *Nonlinear fractional waves at elastic interfaces*, Physical Review Fluids **2** (2017), 114804.

[114] Lev Davidovich Landau and Evgenii Mikhailovich Lifshitz, *Fluid mechanics: Course of theoretical physics, volume 6*, vol. 6, Elsevier, 2013.

[115] Logan E. Hillberry, Yi Xu, Sebastian Miki-Silva, Gabriel H. Alvarez, Julia E. Orenstein, L. C. Ha, Diney S. Ether, and Mark G. Raizen, *Weighing an optically trapped microsphere in thermal equilibrium with air*, Physical Review Applied **14** (2020), no. 4, 044027.

[116] K. C. Neuman and A. Nagy, *Single-molecule force spectroscopy: optical tweezers, magnetic tweezers and atomic force microscopy*, Nature Methods **5** (2008), no. 6, 491.

[117] B. Pontes, N. B. Viana, L. Campanati, M. Farina, V. Moura Neto, and H. M Nussenzveig, *Structure and elastic properties of tunneling nanotubes*, European Biophysical Journal **37** (2008), 121.

[118] S. Frases, B. Pontes, L. Nimrichter, M. L. Rodrigues, N. B.Viana, and A. Casadevall, *The elastic properties of the Cryptococcus neoformans capsule*, Biophysical Journal **97** (2009), 937.

[119] B. Pontes, N. B. Viana, L. T. Salgado, M.Farina, V. Moura Neto, and H.M.Nussenzveig, *Cell cytoskeleton and tether extraction*, Biophysical Journal **101** (2011), 43.

[120] E. Moeendarbary and A. R. Harris, *Cell mechanics: principles, practices, and prospects*, Wiley Interdisciplinary Reviews: Systems Biology and Medicine **6** (2014), 371.

[121] Matthew P. Nicholas, Lu Rao, and Arne Gennerich, *An improved optical tweezers assay for measuring the force generation of single kinesin molecules*, Methods in Molecular Biology **1136** (2014), 171.

[122] Yareni A. Ayala, Bruno Pontes, Diney S. Ether, Luis B. Pires, Glauber R. Araujo, Susana Frases, Luciana F. Romão, Marcos Farina, Vivaldo

Moura-Neto, Nathan B. Viana, et al., *Rheological properties of cells measured by optical tweezers*, BMC biophysics **9** (2016), no. 1, 1–11.

[123] H. M. Nussenzveig, *Cell membrane biophysics with optical tweezers*, European Biophysical Journal **47** (2018), 499.

[124] C. Bustamante, Y. R. Chemla, and Jeffrey R. Moffitt, *High-resolution dual-trap optical tweezers with differential detection: Alignment of instrument components*, Cold Spring Harbor Protocols **161** (2009), 260.

[125] J. Gieseler, B. Deutsch, R. Quidant, and L. Novotny, *Subkelvin parametric feedback cooling of a laser-trapped nanoparticle*, Physical Review Letters **109** (2012), 103603.

[126] Jan Gieseler, Juan Ruben Gomez-Solano, Alessandro Magazzù, Isaac Pérez Castillo, Laura Pérez García, Marta Gironella-Torrent, Xavier Viader-Godoy, Felix Ritort, Giuseppe Pesce, Alejandro V. Arzola, Karen Volke-Sepúlveda, and Giovanni Volpe, *Optical tweezers — from calibration to applications: a tutorial*, Mar 2021, pp. 74–241.

[127] U. Delić, M. Reisenbauer, K. Dare, D. Grass, V. Vuletić, N. Kiesel, and M. Aspelmeyer, *Cooling of a levitated nanoparticle to the motional quantum ground state*, Science **367** (2020), no. 6480, 892.

[128] Felix Tebbenjohanns, M. Luisa Mattana, Massimiliano Rossi, Martin Frimmer, and Lukas Novotny, *Quantum control of a nanoparticle op-*

tically levitated in cryogenic free space, Nature **595** (2021), no. 7867, 378–382.

[129] R. Kaltenbaek, M. Aspelmeyer, and P. F. Barker *et al.*, *Macroscopic quantum resonators (maqro): 2015 update*, European Physical Journal Quantum Technology **3** (2016), 5.

[130] Felix Tebbenjohanns, Martin Frimmer, Vijay Jain, Dominik Windey, and Lukas Novotny, *Motional sideband asymmetry of a nanoparticle optically levitated in free space*, Physical Review Letters **124** (2020), 013603.

[131] Felix Tebbenjohanns, Martin Frimmer, Andrei Militaru, Vijay Jain, and Lukas Novotny, *Cold damping of an optically levitated nanoparticle to microkelvin temperatures*, Physical Review Letters **122** (2019), no. 22, 223601.

[132] E. Hebestreit, M. Frimmer, R. Reimann, C. Dellago, F. Ricci, and L. Novotny, *Calibration and energy measurement of optically levitated nanoparticle sensors*, Review of Scientific Instruments **89** (2018), 033111.

[133] F. Ricci, M. T. Cuairan, G. P. Conangla, A. W. Schell, and R. Quidant, *Accurate mass measurement of a levitated nanomechanical resonator for precision force-sensing*, Nano Letters **19** (2019), 6711.

[134] Yu Zheng, Lei-Ming Zhou, Yang Dong, Cheng-Wei Qiu, Xiang-Dong Chen, Guang-Can Guo, and Fang-Wen Sun, *Robust optical-levitation-*

based metrology of nanoparticle's position and mass, Physical Review Letters **124** (2020), 223603.

[135] Gambhir Ranjit, David P. Atherton, Jordan H. Stutz, Mark Cunningham, and Andrew A. Geraci, *Attonewton force detection using microspheres in a dual-beam optical trap in high vacuum*, Physical Review A **91** (2015), 051805(R).

[136] Gambhir Ranjit, Mark Cunningham, Kirsten Casey, and Andrew A. Geraci, *Zeptonewton force sensing with nanospheres in an optical lattice*, Physical Review A **93** (2016), 053801.

[137] Fernando Monteiro, Sumita Ghosh, Adam Getzels Fine, and David C. Moore, *Optical levitation of 10-ng spheres with nano-g acceleration sensitivity*, Physical Review A **96** (2017), 063841.

[138] Gabriel Schnoering, Yoseline Rosales-Cabara, Hugo Wendehenne, Antoine Canaguier-Durand, and Cyriaque Genet, *Thermally limited force microscopy on optically trapped single metallic nanoparticles*, Physical Review Applied **11** (2019), 034023.

[139] James Millen, Tania S. Monteiro, Robert Pettit, and A. Nick Vamivakas, *Optomechanics with levitated particles*, Reports on Progress in Physics **83** (2020), no. 2, 026401.

[140] S. R. Parnell, A. L. Washington, A. J. Parnell, A. Walsh, R. M. Dalgliesh, F. Li, W. A. Hamilton, S. Prevost, J. P. A. Fairclough, and R. Pynn,

Porosity of silica stöber particles determined by spin-echo small angle neutron scattering, Soft Matter **12** (2016), no. 21, 4709–4714.

[141] Charles P. Blakemore, Alexander D. Rider, Sandip Roy, Alexander Fieguth, Akio Kawasaki, Nadav Priel, and Giorgio Gratta, *Precision mass and density measurement of individual optically levitated microspheres*, Physical Review Applied **12** (2019), 024037.

[142] Gehrig Carlse, Kevin B. Borsos, Hermina C. Beica, Thomas Vacheresse, Alex Pouliot, Jorge Perez-Garcia, Andrejs Vorozcovs, Boris Barron, Shira Jackson, Louis Marmet, and A. Kumarakrishnan, *Technique for rapid mass determination of airborne microparticles based on release and recapture from an optical dipole force trap*, Physical Review Applied **14** (2020), 024017.

[143] Z. Gong, Y.-L Pan, G. Videen, and C. Wang, *Optical trapping and manipulation of single particles in air: Principles, technical details, and applications*, Journal of Quantitative Spectroscopy and Radiative Transfer **214** (2018), 94.

[144] A. van der Horst, P. D. J. van Oostrum, A. Moroz, A. van Blaaderen, and Marileen Dogterom, *High trapping forces for high-refractive index particles trapped in dynamic arrays of counterpropagating optical tweezers*, Applied Optics **47** (2008), 3196.

[145] Stephen R. Cole, Haitao Chu, and Sander Greenland, *Maximum likelihood, profile likelihood, and penalized likelihood: a primer*, American

Journal of Epidemiology **179** (2014), no. 2, 252–260.

[146] S. F. Norrelykke and H. Flyvbjerg, *Power spectrum analysis with least-squares fitting: Amplitude bias and its elimination, with application to optical tweezers and atomic force microscope cantilevers*, Review of Scientific Instruments **81** (2010), 075103.

[147] Chris Dawson and James Bateman, *Spectral analysis and parameter estimation in levitated optomechanics*, Journal of the Optical Society of America B **36** (2019), no. 6, 1565–1573.

[148] Sydney Chapman, Thomas George Cowling, and David Burnett, *The mathematical theory of non-uniform gases: an account of the kinetic theory of viscosity, thermal conduction and diffusion in gases*, Cambridge University Press, 1990.

[149] P. T. Tsilingiris, *Review and critical comparative evaluation of moist air thermophysical properties at the temperature range between 0 and 100 c for engineering calculations*, Renewable and Sustainable Energy Reviews **83** (2018), 50–63.

[150] Joel Tellinghuisen, *Statistical error propagation*, The Journal of Physical Chemistry A **105** (2001), no. 15, 3917–3921.

[151] J. Millen, T. Deesuwan, P. Barker, and Janet Anders, *Nanoscale temperature measurements using non-equilibrium brownian dynamics of a levitated nanosphere*, Nature Nanotechnology **9** (2014), no. 6, 425.

[152] L. B. Pires, D. S. Ether, B. Spreng, G. R. S. Araújo, R. S. Decca, R. S. Dutra, M. Borges, F. S. S. Rosa, G.-L. Ingold, M. J. B. Moura, S. Frases, B. Pontes, H. M. Nussenzveig, S. Reynaud, N. B. Viana, and P. A. Maia Neto, *Probing the screening of the casimir interaction with optical tweezers*, Phys. Rev. Research **3** (2021), 033037.

[153] Karel Svoboda, Christoph F. Schmidt, Bruce J. Schnapp, and Steven M. Block, *Direct observation of kinesin stepping by optical trapping interferometry*, Nature **365** (1993), no. 6448, 721–727.

[154] Jonghoon Ahn, Zhujing Xu, Jaehoon Bang, Peng Ju, Xingyu Gao, and Tongcang Li, *Ultrasensitive torque detection with an optically levitated nanorotor*, Nature Nanotechnology **15** (2020), no. 2, 89–93.

[155] Charles P. Blakemore, Denzal Martin, Alexander Fieguth, Akio Kawasaki, Nadav Priel, Alexander D. Rider, and Giorgio Gratta, *Absolute pressure and gas species identification with an optically levitated rotor*, Journal of Vacuum Science & Technology B, Nanotechnology and Microelectronics: Materials, Processing, Measurement, and Phenomena **38** (2020), no. 2, 024201.

[156] David C. Moore and Andrew A. Geraci, *Searching for new physics using optically levitated sensors*, Quantum Science and Technology **6** (2021), no. 1, 014008.

[157] Asimina Arvanitaki and Andrew A. Geraci, *Detecting high-frequency*

gravitational waves with optically levitated sensors, Physical Review Letters **110** (2013), no. 7, 071105.

[158] Silke R. Kirchner, Spas Nedev, Sol Carretero-Palacios, Andreas Mader, Madeleine Opitz, Theobald Lohmüller, and Jochen Feldmann, *Direct optical monitoring of flow generated by bacterial flagellar rotation*, Applied Physics Letters **104** (2014), no. 9, 093701.

[159] Spas Nedev, S. Carretero-Palacios, S. R. Kirchner, F. Jäckel, and J. Feldmann, *Microscale mapping of oscillatory flows*, Applied Physics Letters **105** (2014), no. 16, 161113.

[160] Alexander Ohlinger, Andras Deak, Andrey A. Lutich, and Jochen Feldmann, *Optically trapped gold nanoparticle enables listening at the microscale*, Physical Review Letters **108** (2012), 018101.

[161] P. Ghoddoosi Dehnavi, D. Wei, M.-E. Aubin-Tam, and D. S. W. Tam, *Optical tweezers-based velocimetry: a method to measure microscale unsteady flows*, Experiments in Fluids **61** (2020), no. 9, 1–15.

[162] Nicolas Bruot, Pietro Cicuta, Hermes Bloomfield-Gadêlha, Raymond E. Goldstein, Jurij Kotar, Eric Lauga, and Fran çois Nadal, *Direct measurement of unsteady microscale stokes flow using optically driven microspheres*, Physical Review Fluids **6** (2021), 053102.

[163] P. G. Bassindale, D. B. Phillips, A. C. Barnes, and B. W. Drinkwater, *Measurements of the force fields within an acoustic standing wave using*

holographic optical tweezers, Applied Physics Letters **104** (2014), no. 16, 163504.

[164] Owen Cramer, *The variation of the specific heat ratio and the speed of sound in air with temperature, pressure, humidity, and co2 concentration*, The Journal of the Acoustical Society of America **93** (1993), no. 5, 2510–2516.

[165] Chuji Wang, Yong-Le Pan, and Gorden Videen, *Optical trapping and laser-spectroscopy measurements of single particles in air: a review*, Measurement Science and Technology **32** (2021), no. 10, 102005.

[166] Alexander Logozzo and Thomas C. Preston, *Temperature-controlled dual-beam optical trap for single particle studies of organic aerosol*, The Journal of Physical Chemistry A **126** (2021), no. 1, 109–118.

[167] Jessica W Lu, Merrill Isenor, Egor Chasovskikh, David Stapfer, and Ruth Signorell, *Low-temperature bessel beam trap for single submicrometer aerosol particle studies*, Review of Scientific Instruments **85** (2014), no. 9, 095107.

[168] Kazuki Taji, Maki Tachikawa, and Kazushige Nagashima, *Laser trapping of ice crystals*, Applied Physics Letters **88** (2006), no. 14, 141111.

[169] Shoji Ishizaka, Teruhide Wada, and Noboru Kitamura, *In situ observations of freezing processes of single micrometer-sized aqueous ammonium*

sulfate droplets in air, Chemical Physics Letters **506** (2011), no. 1-3, 117–121.

[170] Marcello De Matteis, Andrea Baschirotto, and Elia Vallicelli, *Acoustic analog signal processing for 20–200 mev proton sound detectors*, IEEE Transactions on Radiation and Plasma Medical Sciences **6** (2021), no. 3, 325–335.

[171] F. R. Deurvorst, G. Collado Lara, A. Matalliotakis, H. J. Vos, N. De Jong, V. Daeichin, and M. D. Verweij, *A spatial and temporal characterisation of single proton acoustic waves in proton beam cancer therapy*, The Journal of the Acoustical Society of America **151** (2022), no. 2, 1200–1210.

[172] E. Behnke, J. Behnke, S. J. Brice, D. Broemmelsiek, J. I. Collar, P. S. Cooper, M. Crisler, C. E. Dahl, D. Fustin, J. Hall, et al., *Improved limits on spin-dependent wimp-proton interactions from a two liter* CF_3I *bubble chamber*, Physical Review Letters **106** (2011), no. 2, 021303.

[173] Tetiana Kozynets, Scott Fallows, and Carsten B. Krauss, *Modeling emission of acoustic energy during bubble expansion in pico bubble chambers*, Physical Review D **100** (2019), 052001.

[174] C. Amole et al., *Dark matter search results from the complete exposure of the PICO-60* C_3F_8 *bubble chamber*, Physical Review D **100** (2019), 022001.

[175] Jianyong Mo and Mark G. Raizen, *Highly resolved brownian motion in space and in time*, Annual Review of Fluid Mechanics **51** (2019), no. 1, 403–428.

[176] Richard P. Feynman, *Plenty of room at the bottom*, APS Annual Meeting, 1959.

Vita

Logan Hillberry was born in Westminster, CO in 1993. He attended The Colorado School of Mines in 2012, obtaining a BS in engineering physics in 2015 and an MS in applied physics in 2016 under the direction of Prof. Lincoln Carr. Logan entered the physics Ph.D. program at The University of Texas at Austin in 2016 where he has since been supervised by Prof. Mark Raizen.

Address: lhillberry@gmail.com

This dissertation was typeset with LaTeX[†] by the author.

[†]LaTeX is a document preparation system developed by Leslie Lamport as a special version of Donald Knuth's TeX Program.